# Silica-on-silicon optical couplers and coupler based optical filters

**Leick, Lasse; Povlsen, Jørn Hedegaard; Nicolaisen, Ejner**

*Publication date:*
2002

*Document Version*
Publisher's PDF, also known as Version of record

# Silica-on-silicon couplers and coupler-based optical filters for wavelength division multiplexed networks

Lasse Leick
*COM*
Technical University of Denmark
Delivered:1 March 2002,
Defence: 12 June 2002,
Revised: 17 July 2002

The present work was carried out at *COM* in partial fulfillment of the requirements for the Ph.D. degree from the Technical University of Denmark

# Contents

# Abstract

This work concerns modeling and characterization of non amplifying silica-on-silicon optical components for wavelength division multiplexed networks. Emphasis is placed on optical couplers and how they can be used as building blocks for devices with a larger complexity. It has been investigated how to construct wavelength flattened and process tolerant couplers. A thorough comparison between directional couplers, multi mode interference couplers and interferometer-based couplers has been performed. Numerically all these architectures have the ability to obtain similar wavelength-flatness, but the multi mode interference couplers have superior process tolerance. The measured characteristics of multi mode interference couplers deviate from the simulations, showing an unexpected imbalance and large polarization sensitivity. This can be explained by a slightly non-uniform index distribution across the multi mode interference slab. Accordingly the process tolerance of multi mode interference couplers is inferior to what has previously been assumed. The directional couplers show better agreement between simulations and measurements, but a qualitative comparison shows that a rectangular step-index model is not an adequate description of the waveguides.

A simple application for an optical coupler is as a 980/1550 nm multiplexer for erbium doped waveguide amplifiers. A numerical analysis shows that a directional coupler has acceptable specifications, whereas a multi mode interference coupler does not. The wavelength flatness can be improved by using a new point-symmetric interferometer structure. The proposed multiplexer fulfills commercial specifications over a wavelength range from 1500 nm to 1600 nm.

Furthermore the spectral and dispersion response of a $1x4$ interferometer based multiplexer/demultiplexer with single-stage all-pass filters in the arms is modeled. The all-pass filters ensure that the demultiplexer has excellent transmission, but add a substantial, detrimental cubic dispersion over the channel passband. This limits the number of demultiplexers that can be cascaded without incurring a significant power penalty. The dispersion can be removed by adding a three-stage all-pass filter on the input arm.

The above mentioned silica-on-silicon components have been fabricated using a conventional method where the waveguides are defined and fabricated using cleanroom processing. Waveguides can also be fabricated by an alternative ultraviolet-writing method. It is shown experimentally that it is possible to describe the waveguiding properties of ultraviolet-written waveguides by a rectangular step-index profile. The model facilitates development of new ultraviolet-written components.

# Sammendrag

Denne afhandling omhandler design, modellering og karakterisering af ikke forstærkende silica-glas komponenter til brug i optiske kommunikationssystemer, hvor der er lagt vægt på optiske koblere, samt hvordan disse kan benyttes i komponenter med en mere komplex funktionalitet. Det er blevet undersøgt, hvordan der er muligt at producere bølgelængdeflade koblere, som er ufølsomme overfor procesvariationer. Herunder er der foretaget en grundig sammenligning af retningskoblere, multi mode interferens koblere og interferometer-baserede koblere. Numerisk kan alle disse arkitekturer opnå sammenlignelig bølgelængdefladhed, men multi mode interferens koblere har størst procestolerance. Imidlertid afviger målingerne for multi mode interferens koblere fra simulationerne, idet de viser en uventet ubalance samt en stor polarisationsafhængighed. Dette kan forklares ved et ikke-uniformt brydningsindeks på tværs af strukturen. Derved er multi mode interferens koblere ikke så procestolerante, som det hidtil er blevet antaget. Retningskoblerne viser større overensstemmelse mellem simulationerne og måleresultaterne, men en kvalitativ sammenligning viser, at det ikke er muligt at beskrive bølgelederne indenfor en step-indeks model. En simpel anvendelse for optiske koblere er som en 980/1550 nm multiplexer for erbium doterede bølgelederforstærkere. En analyse viser, at en retningskobler har gode specifikationer hertil, men at multi mode interferens kobleren ikke har dette. Bølgelængdefladheden kan øges ved at benytte en ny punktsymmetrisk struktur af to asymmetriske retningskoblere. Denne opfylder kommercielle specifikationer over hele bølgelængdeområdet fra 1500 nm til 1600 nm. Endvidere er der arbejdet med at modellere den spektrale afhængighed af transmissionen og dispersionen af en $1x4$ interferometer-baseret multiplexer/demultiplexer med såkaldte all-pass filtre i interferometerets arme. All-pass filtrene bevirker at demultiplexeren opnår en fremragende transmission, men giver også en betydelig og skadelig dispersion. Denne begrænser det antal af demultiplexere, som kan anbringes i forlængelse af hinanden, uden at der kommer en betydelig power penalty. Dispersionen kan ikke fjernes ved optimering af all-pass filtrene, men derimod ved at placere et all-pass filter på demultiplexerens input arm.

De hidtil beskrevne silica-glas komponenter er blevet fremstillet med en konventionel teknik, hvorved bølgelederne bliver defineret og fabrikeret i et rentrum. Det er også muligt at fabrikere komponenterne ved en alternativ metode, hvori bølgelederne bliver defineret ved direkte ultraviolet-skrivning. I dette arbejde er det eksperimentielt eftervist, at bølgelederegenskaberne af ultraviolet-skrevne bølgeldere kan beskrives med en rektangular step-indeks profil. Modellen letter udvikling af nye ultraviolet-skrevne komponenter.

# Acknowledgments

I would like to thank my supervisors Jørn Hedegaard Povlsen and Ejner Nicolaisen as well as my former supervisors Rune Pedersen and Jörg Hübner for advice, help, support and for always having time to discuss whatever problems I might have. Mikael Svalgaard, Anders Harpøth and Kjartan Færch are acknowledged for fabricating the ultraviolet-written waveguides and for their collaboration in constructing a model for the waveguiding properties for these. Haiyan Ou from *COM* and the Slimline group at Lucent Technologies Bell Labs deserves credit for fabrication of the standard waveguides. Dan A. Zauner and Rasmus K. Sandberg are acknowledged for collaboration on optimizing wavelength-flattened optical couplers and a pump/signal multiplexer for erbium doped waveguide amplifiers, respectively. Furthermore I would like to thank Lars-Ulrik Andersen, Kevin Malone, Jesper Bo Jensen, Christophe Peucheret, Morten G. Dyndgaard, Søren Guldberg-Kjær, Peter Carøe Nielsen and Mogens Rysholt Poulsen for their help.

I am grateful to Alice E. White for allowing me to spend half a year in her research group at Lucent Technologies Bell Labs and to Christi K. Madsen for her help during the stay. Debbie Gras is thanked for help with all sorts of practical problems, and Mahmoud Rasras for good collaboration.

The staff at *COM* are thanked for creating a good and informal atmosphere with plenty of room for discussion of both scientific and other matters. Finally Dan A. Zauner, Mikael Svalgaard and Jørn Hedegaard Povlsen are thanked for their help with improving this manuscript.

# List of abbreviations

*ASE*: Amplified spontaneous emission
*AWG*: Arrayed waveguide grating (a.k.a. waveguide grating router, phasar)
*BCW*: Buried channel waveguides
*BER*: Bit error rate
*BPM*: Beam propagation method
*DEMUX*: Demultiplexer
*DUT*: Device under test
*EDWA*: Erbium doped waveguide amplifiers
*EIM*: Effective index method
*FD* method: Finite difference method
*FSR*: Free spectral range
*FWHM*: Full-width at half maximum
*GMZI*: Generalized Mach-Zehnder interferometer
*MMI*: Multimode interference coupler
*MPA*: Mode propagation analysis
*MUX*: Multiplexer
*MZI*: Mach-Zehnder interferometer
*OSA*: Optical spectrum analyzer
*PDC*: Polarization dependent coupling
*PDL*: Polarization dependent loss
*PECVD*: Plasma enhanced chemical vapor deposition
*PRBS:* Pseudo random bit sequence
*RIE*: Reactive ion etching
*SMF*: Single mode fiber
*TE*: Transverse electric field
*TM*: Transverse magnetic field
*UA* coupler: Uniform asymmetric coupler
*UMZI* coupler: Unbalanced Mach-Zehnder interferometer coupler
*US* coupler: Uniform symmetric coupler
*UV*: Ultraviolet
*WDM*: Wavelength division multiplexing
*WGR*: Waveguide grating router
*WWR***:** Waveguide width reduction

# Chapter 1

# Introduction

The field of optical communication emerged in the $1960's$ and has ever since been growing tremendously to satisfy the rapidly increasing demand for larger capacity. Optical telecommunication provides the necessary bandwidth to transmit the information and thus is an enabling technology for the rapid growth in voice and data traffic. A forecast from Kleiner Perkins Caufield & Byers (a leading venture capitalist) predicts an exponential growth in optical bandwidth with a doubling time of nine months [1],[1]. The growth will be fueled by increasing the number of customers and by providing new bandwidth demanding services to the customers (e.g. fiber to the home and the mobile internet). Over the last three decades the complexity of computer chips has been doubling every eighteen months (Moore's law). A comparison shows that the electronics can not keep up with the growth in bandwidth, thus creating a potential bottleneck for utilization of the increased bandwidth. Consequently optical components will become increasing important to handle the enormous bandwidth.

A basic optical telecommunication systems consists of an information source (a laser and a modulator), a transport medium (an optical fiber) and a detection system (an electrical detector). The information is stored in the modulation pattern of the source and accordingly the frequency of modulation sets the bit rate at which information is transmitted [2]. Using this technique in combination with time division multiplexing presently commercial long haul systems employ bit rates of up to 10 $Gbit/s$. Higher bit rates have been demonstrated

[1] The forecast is from before the current crisis in the high tech industry. Thus it might be somewhat optimistic, but it gives an estimate of the impetus in the development. Furthermore, historical projections have all fallen short of the actual development.

in research labs, but they impose very strict specifications to limit dispersion induced problems (including polarization mode dispersion) and the speed of the electronics.

Another method of increasing the bit rate employs that signals at different wavelengths only interact by non-linear effects, whence it is possible to transmit several signals with different wavelengths on the same optical fiber. This technique is termed wavelength division multiplexing (*WDM*) and can be used to increase the bandwidth of the fiber. It has enormous potential with demonstrated transmission rates of 10.2 $TBit/s$ over 100km [3] and 3 $Gbit/s$ over 7380km [4]. Using *WDM* networks furthermore enables optical routing according to the wavelength of the signal by means of optical cross-connects. Creating optical cross-connects is far from trivial, but it is currently a very hot research topic (e.g. [5]) as optical cross connects can replace extremely costly electronic routing terminals.

For *WDM* networks to be efficient requires active components such as high quality lasers at the desired wavelengths, electro-optic modulators and wavelength converters. In addition a new class of non-amplifying optical components become necessary e.g. to optically multiplex and demultiplex signals at different wavelengths, to route them according to their wavelength and to compensate for their difference in intensity and dispersion. These components can be fabricated using many different technologies, and all applications will not have the same optimal realization [6]. However, like in the electronic industry it is important to work towards optical integration in order to increase the functionality and reduce the cost. A candidate for optical integrated components is the planar silica-on-silicon technology. This technology has many advantages as low material loss, stable refractive index, low connection loss to standard fibers, low material cost and compatibility with the silicon technology [7], but also has problems as birefringence and side-wall roughness and limitations as no electro-optic effect.

The present work describes planar non-amplifying silica-on-silicon components for optical telecommunication systems, and is a result of a Ph.D. project at *COM*, which is an institute at the Technical University of Denmark. The emphasis of the work has been to design, simulate and characterize optical components for *WDM* networks. In the initial part of the project I worked on optimizing wavelength-flattened process flattened optical couplers. This was followed by an investigation of how to use couplers as building blocks in *WDM* devices, i.e. as a pump/signal multiplexer for amplifying waveguides and as interferometer based multiplexer/demultiplexer with flattened passband, low loss and low dispersion. The latter part was mainly conducted during a period as

visiting scientist at Lucent Technologies Bell Labs, under supervision of Dr. Christi Madsen. Finally I have developed an empirically based model for the waveguiding properties of ultraviolet ($UV$) written waveguides.

A substantial part of the research has been performed in collaboration with others. They shall not be credited in each particular instance, but in a separate acknowledgment section. An exception occurs if the particular measurement or simulation has been performed without my help, in which case the names of the persons who have performed the work are given.

This thesis is divided into nine chapters including this introduction. **Chapter 2** and **3** gives the necessary background information needed to understand the research that has been conducted. In **Chapter 2** some commonly used numerical modeling techniques are described, including both mode solvers and propagation solution techniques. This is followed by a description of the transfer matrix method, which is useful because it allows a hierarchical approach to modeling complicate devices. Hence a device can be split into several parts that are treated independently, whereupon the total transfer matrix is found by matrix algebra. **Chapter 3** reviews the fabrication technologies for silica-on-silicon waveguide. Including both a standard cleanroom fabrication method and an alternative method in which the waveguides are fabricated by direct $UV$-writing. Furthermore practical limitations in the fabrication and inevitable process variations are discussed and there is a description of the setup used for characterizing the fabricated components.

**Chapter 4** to **8** describes the research that has been conducted during my Ph.D. project, and accordingly presents the core of this thesis.

**Chapter 4** concerns straight waveguides. Measurements of the various losses (coupling, propagation and polarization dependent loss) and the birefringence and size of the waveguides are presented. These measurements give essential feedback to the fabrication process and serve as input to modeling waveguide components. Both the standard and $UV$-writing technology can be used to fabricate low loss components. The fabricated standard waveguides have problems with birefringence (especially for very wide waveguides). The $UV$-written waveguides have low birefringence but a comparably high propagation loss, which poses a problem for realizing long components.

**Chapter 5** describes planar $2x2$ optical 3 $dB$ couplers optimized for high process tolerance and wavelength-flattened coupling from 1500 nm to 1600 nm. A rigorous numerical comparison of different architectures is performed, and the results are used to fabricate the best suited components. Subsequent measurements show reasonable agreement with the simulations, although it must be concluded that a rectangular step-index model does not adequately describe

the waveguides. Furthermore the measurements of multi mode interference couplers show an unexpected large polarization sensitivity and imbalance between the output arms. A numerical and experimental investigation shows that this is probably due to a non-uniform index distribution where the index is slighty lower at the edge than in the center of the multi mode interference coupler, which can be caused by stress in the waveguides. Thus multi mode interference couplers are less process tolerant than what has previously been assumed.

In **Chapter 6** multiplexers for erbium doped waveguide amplifiers are optimized for wavelength-flattened passband. The discussion includes directional and multi mode interference couplers and a new architecture, which consists of a point-symmetric Mach-Zehnder interferometer of two uniform asymmetrical couplers. The directional coupler has good specifications with a 980 nm pump loss of less than 0.2 $dB$ and a $-0.2$ $dB$ signal passband of approximately 80 nm. Simulations show that the new design has similar pump loss as the directional coupler in addition it has an extremely flat signal passband with a $-0.1$ $dB$ passband of approximately 200 nm. It furthermore has good process tolerance with a signal loss of less than 0.1 $dB$ from 1500 nm to 1600 nm when realistic process variations are considered.

The topic of **Chapter 7** is a $1x4$ interferometer based passive optical multiplexer/ demultiplexer, where the interferometer arms lengths differ by units of a discrete delay. By including a single-stage all pass filter in each interferometer arm the multiplexer achieves an excellent transmission spectrum. Hence the filter can be cascaded a number of times while maintaining a substantial bandwidth. However, the all-pass filter also incur a substantial detrimental cubic dispersion over the passband. The dispersion shape is inherent to the architecture and can not be removed without using additional non-linear phase filters. As the dispersion is identical from channel-to-channel it can be compensated for all of them by adding a all-pass filter to the single input arm. Simulations show that a three-stage all-pass filter reduces the maximum dispersion over a 60% passband by a factor of 16. It is shown by a loop transmission simulation that the dispersion compensating filter significantly improves the transmission through a cascade of multiplexers. Finally some considerations on the requirements for fabricating the multiplexer are presented. Based on measurements on ring and multi mode interference couplers it seems feasible to fabricate the multiplexer.

**Chapter 8** is concerned with directly $UV$-written waveguides and how this method can be used to fabricate optical components. For this purpose an empirical model for the waveguiding properties of the directly $UV$-written planar waveguides is developed. Herein the waveguides are described by a rectangular

core step-index profile, where the model parameters are found by comparing measured waveguide characteristics with modal field calculations. The model is used as input for beam propagation method simulations in order to design $UV$-written optical couplers. Subsequent fabrication and a measurement of the refractive index profile show good agreement with the model predictions. Accordingly the model can be used to reduce the number of iterations and the development time of new $UV$-written optical components.

The conclusions of the work are summarized in **chapter 9.**

# Chapter 2

# Modeling

The theory of dielectric waveguides is well described in the literature, and it is not the intent of this chapter to reproduce a detailed and rigorous account of the theory, which can be found elsewhere [8], [9], [10], [11], [7], [12]. The aim of the chapter is to give a brief summary of the theory to facilitate the reading of this work. Emphasis is on the modeling methods that are used in this work and their accuracy is tested.

The chapter contains a description of the scalar wave equation. It is shown that within the paraxial approximation of the scalar wave equation it is possible to derive normalized parameters allowing optical components to be scaled from one index step to another. The scalar wave equation does not have an analytical solution for rectangular waveguides. Hence it is necessary to use numerical methods to solve the wave equation and find the transfer function. The transfer matrix approach enables splitting an architecture into several parts, which can be treated independently, whereupon the total transfer matrix can be found by matrix algebra. Finally effects of changing the wavelength and the spectral response of filters with discrete delays are considered.

## 2.1 The scalar wave equation

The starting point for analyzing optical waveguides are the Maxwell equations, or more specifically the vector wave equations for the electric and magnetic fields. Modeling techniques can be divided into two groups: time-harmonic (e.g. monochromatic continuous wave operation) and general time-dependent

analysis (pulsed operation) [12]. In this thesis only the time-harmonic analysis is used, which is a good approximation as long as the temporal pulse duration is much longer than the harmonic period of the light.

Since the components described in this work are realized in silica-on-silicon a propagating field solution in a weakly guiding dielectric medium is sought. Weakly guiding means that the changes in refractive index are small with respect to the mean refractive index of the medium $n_0$. This implies that the field can be assumed to be divergence free with negligible loss of accuracy, whence the field is polarized perpendicular to the propagation direction and the vector wave equations are replaced by a single scalar wave equation [8], [11]. Assume that the refractive index $n(x,y,z)$ only deviates from the background index $n_0$ in a limited region, termed the core. At a single free space wavelength $\lambda_0$ and polarization, the Maxwell equation for the electric field $E_\omega(\mathbf{r})$ is [7]:

$$\nabla^2 E_\omega(\mathbf{r}) + k^2 n^2(\mathbf{r}) E_\omega(\mathbf{r}) = 0 \tag{2.1}$$

where $\omega = kc$ is the angular frequency, $k = \frac{2\pi}{\lambda_0}$ is the free space wave number and $\mathbf{r} = (x,y,z)$ is the space coordinate. The propagating wave solution to this equation has the form:

$$E_\omega(\mathbf{r}) = \Theta(x,y,z)\exp(-i\omega t) \tag{2.2}$$

where $\Theta(x,y,z)$ is the field distribution, $i = \sqrt{-1}$ and $t$ is the time. In a typical guided-wave problem the field propagates along a preferred direction, set to be the $z$-direction. It is advantageous to factor out the rapid variation along the $z$-axis, by writing the field as:

$$\Theta(x,y,z) = \Phi(x,y,z)\exp(ikn_0 z) \tag{2.3}$$

where $\Phi(x,y,z)$ is termed the slowly varying field. Insertion of eq. 2.3 into eq. 2.1 yields the following expression for the slowly varying field:

$$[\frac{\partial^2}{\partial z^2} + 2ikn_0\frac{\partial}{\partial z}]\Phi(x,y,z) + [\frac{\partial^2}{\partial x^2} + \frac{\partial^2}{\partial y^2} + k^2(n^2(x,y,z) - n_0^2)]\Phi(x,y,z) = 0 \tag{2.4}$$

Define $\Delta n(x,y,z) = n(x,y,z) - n_0$. By the weakly guiding assumption $\Delta n << 1$ whence $n^2(x,y,z) - n_0^2 \simeq 2n_0\Delta n(x,y,z)$. Assume that $\frac{\partial^2}{\partial z^2}\Phi$ is negligible to obtain:

$$\frac{i}{k}\frac{\partial}{\partial z}\Phi(x,y,z) = -\frac{1}{2n_0k^2}(\frac{\partial^2}{\partial x^2} + \frac{\partial^2}{\partial y^2})\Phi(x,y,z) - \Delta n(x,y,z)\Phi(x,y,z) \tag{2.5}$$

which is called the scalar paraxial wave equation. The accuracy of the paraxial approximation increases with the mode size, and decreases with the index contrast $\Delta n$. By comparison eq. 2.5, is seen to be similar to the time dependent two-dimensional Schrödinger equation for a particle with mass $m$ in a potential $V(x,y,t)$:

$$i\hbar\frac{\partial}{\partial t}\psi(x,y,t) = -\frac{\hbar^2}{2m}(\frac{\partial^2}{\partial x^2} + \frac{\partial^2}{\partial y^2})\psi(x,y,t) + V(x,y,t)\psi(x,y,t) \qquad (2.6)$$

Thus monochromatic field propagation along the $z$-axis is equivalent to quantum mechanical time evolution of a particle with mass $m \propto n_0$ in a potential $V \propto -\Delta n$. Hence a positive index perturbation is able to confine light as a potential well is able to trap a particle. A local increase in refractive index is termed a waveguide. If the refractive index is independent of $z$ the situation corresponds to time independent potential and the field propagation corresponds to the time evolution of a particle in a time independent potential well. In analogy with the potential well, the waveguide has a finite number of bounded and an infinite number of unbounded modes, these are termed guided and radiation modes. Each mode has its own field distribution and propagation constant $\beta$, from which its effective index is defined:

$$n_{eff} \equiv \frac{\beta}{k} \qquad (2.7)$$

A very weak waveguide only has a single guided mode, hence it is termed a single mode waveguide. The bounded modes have a effective index, which is larger than background refractive index $n_{eff} > n_0$ and propagates along an ideal waveguide without loss. Unbounded modes have an effective index which is smaller than the refractive index of the background $n_{eff} < n_0$, whence these modes are lossy and radiates from the waveguide upon propagation. The modes define a complete orthogonal set meaning that any transverse field distribution can be uniquely decomposed into a weighted sum of the waveguides guided and unguided modes.

## 2.2 Scaling the scalar wave equation

Within the paraxial scalar approximation it is possible to scale a device. To see this introduce the following variables:

$$\mathbf{r} = (ax_s, ay_s, bz_s), \qquad \delta n = c\delta n_s, \qquad a,b,c \in R \Rightarrow \tag{2.8}$$

$$\frac{\partial^2}{\partial x_s^2} = a^2\frac{\partial^2}{\partial x^2}, \qquad \frac{\partial^2}{\partial y_s^2} = a^2\frac{\partial^2}{\partial y^2}, \qquad \frac{\partial}{\partial z_s} = b\frac{\partial}{\partial z} \tag{2.9}$$

Insert eq. 2.9 into the scalar paraxial equation (eq. 2.5) to obtain:

$$\frac{i}{k}\frac{\partial}{\partial z_s}\Phi(\mathbf{r}_s) = -\frac{a^2}{b}\cdot\frac{1}{2n_{eff}k^2}(\frac{\partial^2}{\partial x_s^2}+\frac{\partial^2}{\partial y_s^2})\Phi(\mathbf{r}_s) - \frac{1}{cb}\cdot\delta n_s(\mathbf{r}_s)\Phi(\mathbf{r}_s) \tag{2.10}$$

where $\mathbf{r}_s = (x_s, y_s, z_s)$. A comparison shows that eq. 2.10 is identical to eq. 2.5 if:

$$a^2 = b \qquad \wedge \qquad cb = 1 \qquad \Rightarrow \qquad c = \frac{1}{b} = \frac{1}{a^2} \tag{2.11}$$

This implies that the device behavior is unchanged if the index difference $\delta n$ is scaled by $\kappa$, the length by $1/\kappa$ and the height and width by $1/\sqrt{\kappa}$. Thus it is possible to change any design from one step-index to another by scaling, which saves time compared to using standard numerical methods. Furthermore scaling is useful if the space requirements for a given device is very strict, as eq. 2.10 shows that the length is decreased if the index difference is increased.

The equations are only valid in the scalar paraxial approximation and e.g. can not be used to scale a 90° bend. However, it has been shown that the radiation coefficient in a circular bend is unchanged if it is scaled so the normalized frequency is constant [13], [14] and the radius $R$ is scaled according to:

$$R \propto \frac{n^{1/2}\lambda}{\Delta n^{3/2}} \tag{2.12}$$

eq. 2.12 can be used to estimate the tolerable bend radius if the step index is increased. For a 90° bend the length is equal to the radius, which shows that the length scales as $\Delta n^{-3/2}$, thus a step-index increase by a factor of two implies a length reduction of 65%.

## 2.3 Buried channel waveguides

In the present work two types of waveguides are encountered: the optical fiber and the planar buried channel waveguide. Traditional fibers have a step-index

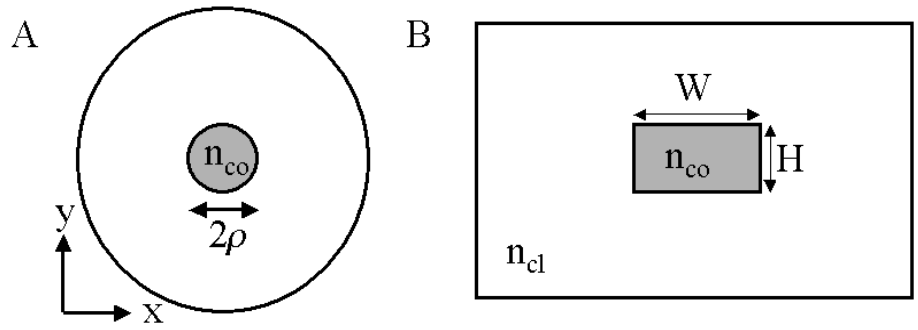


Figure 2.1: The figure shows the geometry of $A$) a step index fiber with radius $\rho$ and $B$) a buried channel rectangular step-index waveguide with width $W$ and height $H$. The size of the core and the cladding is not to scale.

distribution with a circular core of radius of $\rho$ and refractive index $n_{co}$ embedded in a cladding with index $n_{cl}$, which is sufficiently large that the field is negligible at its edges. The normalized frequency of a fiber $V_f$ is defined as:

$$V_f = \frac{2\pi}{\lambda}\rho(n_{co}^2 - n_{cl}^2)^{0.5} \simeq \frac{2\pi}{\lambda}\rho(2n_{co}\Delta n)^{0.5} \tag{2.13}$$

where the last equality uses that $n_{co} \simeq n_{cl}$. The normalized frequency determines the number of modes in the fiber. A fiber is single mode if $V_f < 2.40$, which can be assured by choosing either a small radius $\rho$ or a small step index $\Delta n \equiv n_{co} - n_{cl}$. The confinement increases with the normalized frequency. For a standard single-mode fiber $\rho \simeq 4\,\mu$m and $\Delta n(\lambda = 1.55\,\mu\text{m}) \simeq 0.005$, whence the ground mode of the optical fiber has a field that resembles a Gaussian with a waist of $5.0\,\mu$m [2]. Notice that the normalized frequency is unchanged if the core is scaled according to eq. 2.11.

The planar buried channel waveguide analogy of the circular step index fiber is the buried rectangular step-index waveguide, which is shown in fig. 2.1. The core has a width $W$ and height $H$ and an index of $n_{co}$. In analogy with the optical fiber the normalized frequency of a planar waveguide is defined as:

$$V_w = \frac{2\pi}{\lambda}(\frac{HW}{\pi})^{0.5}(n_{core}^2 - n_{cl}^2)^{0.5} \simeq \frac{2\pi}{\lambda}(\frac{HW}{\pi})^{0.5}(2n_{co}\Delta n)^{0.5} \tag{2.14}$$

where $\rho$ has been replaced by $(HW/\pi)^{0.5}$ to ensure that a square core has a

second mode cut-off at $V_w = 2.40$ [11]. Other definitions can be found in the literature [11], but except for a different front factor the definitions are identical.

As a standard fiber has circular symmetry any two orthogonal axis can be used to define the polarization planes. For a rectangular step-index core the symmetry is broken and there are only two possible orthogonal polarization directions. In this work the field is denoted transverse electric ($TE$) if the electric field is polarized in the horizontal plane (along the $x$-axis in fig. 2.1) and transverse magnetic ($TM$) if the magnetic field is polarized in the horizontal plane. If the effective index of the two polarization states is different the waveguide is said to be birefringent, with a birefringence $\Delta n_{eff}$:

$$\Delta n_{eff} = n_{eff}^{TE} - n_{eff}^{TM} \tag{2.15}$$

From a geometrical consideration the square core has zero birefringence, whereas a wide core ($W > H$) has positive birefringence and a narrow core ($W < H$) negative birefringence. For fabricated waveguides there are also other contributions to the birefringence as e.g. non uniform stress, whence the total birefringence is different than the geometrical birefringence (see chapter 3)

## 2.4 Accuracy of numerical methods

The scalar wave equation can be solved analytically for a one dimensional index distribution (a slab waveguide) and for a circular step index core in a uniform cladding. But for most geometries it can not be solved analytically and it is necessary to use numerical methods. A numerical method is based on an approximation to the exact solution and a criterion that minimizes the error between the two. Numerical methods are characterized by their accuracy, validity region, calculation speed and simplicity. The importance of the accuracy and the validity region is obvious. However, there is no reason to demand a numerical accuracy that is more than an order of magnitude larger than the measurement uncertainty. The importance of the calculation speed stems from the practical point that the method should not be so slow, that it hinders the necessary number of calculations.

Numerical methods can be split into two groups: approximation and asymptotically exact methods. The strength of the approximation methods is their simplicity and large calculation speed, whence they can be used to quickly estimate the desired properties. However, their predictions are inaccurate, and one should exercise caution when using them. The asymptotically exact methods on

the other hand offer a better accuracy, but the trade-off is an added complexity and computation time.

The accuracy of numerical methods can be tested by comparison with an asymptotically exact method, examining the convergence when improving the calculation settings or by examining the predictions on benchmark structures, where the result is known in advance [12].

## 2.5 Numerical mode solvers

In the literature several different mode solvers have been discussed covering both approximation methods (e.g. the Marcatili approximation, the Gaussian approximation and the effective index method) and asymptotically exact methods (e.g. the Fourier decomposition method, the finite element method and the finite difference method) [11]. Here only the effective index method (*EIM*) and the finite difference method (*FD*) are described, as these methods have been widely used in the present work. It is sketched how they solve the scalar wave equation for a rectangular core.

### 2.5.1 Effective index method

The one-dimensional scalar wave equation can be solved analytically. The idea behind the effective index method (*EIM*) is to separate the two-dimensional problem into two coupled one-dimensional problems, which are solved sequentially as sketched on fig. 2.2. First the one-dimensional wave equation is solved for a horizontal slab (i.e. placed along the $x$-axis on fig. 2.2) with index $n_{co}$ and height $H$, which is placed between a buffer and topcladding both having an index of $n_{cl}$, to obtain the effective index of the slab structure $n_{Sl}$. Hereafter a one dimensional wave equation is solved for a vertical slab with index $n_{Sl}$ and width $W$ placed between two layers with index $n_{cl}$. If the two equations are solved in the sequence mentioned the method is termed *EIM-x* because the index in the last one-dimensional problem depends on $x$ (if the sequence is reversed it is termed *EIM-y*).

The *EIM-x* is accurate in the limit of an infinitely wide waveguide, and in general the accuracy of the *EIM-x* increases the closer the structure resembles a slab waveguide, i.e. it increases with the ratio of $W/H$. Thus the *EIM-x* is a better approximation for a multi mode interference structure than for a directional coupler [13]. The *EIM* does not give a good representation of the modal field near the corners of the core and far away from the core [11]. By

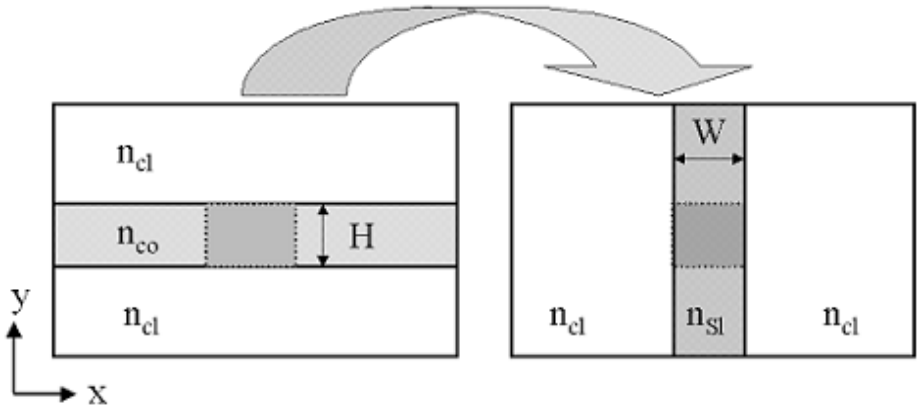


Figure 2.2: In the effective index method the two-dimension wave equation is replaced by two one-dimensional wave equations that are solved sequentially. The core is shown as a grey rectangle in the center of the stucture.

analyzing eq. 2.5 it can furthermore be seen that the *EIM* gives a too high effective index, but that the difference between the effective indices of two modes is determined with a reasonable accuracy. For a more thorough analysis of the accuracy of the *EIM* see appendix A.

### 2.5.2 Finite Difference method

The finite difference (*FD*) method is an asymptotically exact solution of the scalar wave equation and is furthermore quite simple. In the finite difference method the calculation window is discretized with a rectangular grid of points that might be of equal or variable size. In each of the subdivision the partial difference equation is replaced by a finite difference equation by a five point Taylor series formula, whereupon a eigenvalue matrix is assembled. Because the subdivisions are rectangular the *FD* method is primarily suited for rectangular structures. The size of the calculation window should be chosen so that the field is negligible at the boundaries. The boundary conditions for the calculation window can either be transparent or fixed. Fixed boundary conditions means setting the field to zero at the edge of the calculation window, which is a good approximation if there is large index discontinuity there. Transparent boundary

conditions tries to eliminate back reflection into the calculation window and can be implemented in several different fashions e.g. by assuming that the field close to the boundary is a plane wave. The transparent boundary condition is a good approximation if the structure is unchanged across the boundary.

## 2.6 Numerical propagation solution techniques

Propagation solution techniques are used to find a components output field as a function of its input field by propagating the scalar wave equation either in the space or the time domain. For a uniform structure the output field can be found directly from the mode decomposition of the input field using the mode propagation analysis (*MPA*), while applicable methods for a non-uniform structure are the method of lines, the beam propagation method and the finite difference time-domain method [12]. In the following the mode propagation analysis and the beam propagation method (*BPM*) are described.

### 2.6.1 Mode propagation analysis

If the index distribution is uniform throughout the structure (i.e. independent of $z$) then the power in any of its modes is constant. From the modal fields and the decomposition amplitudes at a particular position $z_o$ the field at any $z$ is found by a mode propagation analysis:

$$E(x,y,z_0) = \Sigma a_i \Phi_i(x,y) \Longrightarrow \tag{2.16}$$

$$E(x,y,z) = \Sigma a_i \Phi_i(x,y) \exp[i\beta_i(z-z_0)] \tag{2.17}$$

The main advantage of mode propagation analysis is that it is asymptotically exact (provided that a asymptotically exact mode solver is used) and very fast since eq. 2.1 is only solved once. For a non-uniform structure the mode propagation analysis cannot stand alone. However, for structures with a large uniform part (e.g. a multimode interference coupler) it can be used in combination with another propagation solution technique to reduce the overall calculation time.

### 2.6.2 Beam Propagation Method

The beam propagation method (*BPM*) is the most commonly used propagation technique. It is conceptually straightforward, automatically considers both guided and radiation modes, is readily applied to complex geometries and has optimal efficiency [12]. The basic *BPM* is a solution for a forward propagating

paraxial scalar wave, but the method can be extended to include most effects of interest as e.g. wide-angle propagation [15], polarization effects [16], and reflections [17].

**Comparison of 2 and 3 dimensional *BPM***

The previous discussion considers the three-dimensional (*3D*) finite difference *BPM*, which is an asymptotically exact solution. Even though it has optimal efficiency it is rather slow[1], which is a problem if a large parameter space is to be examined. Hence it can be advantageous to use an approximation method to find the quantitative behavior of a given device, whereafter the *3D BPM* can be used for fine tuning [18]. A widely used approximation method is the two-dimensional (*2D) BPM,* in which the *EIM-x* is used to reduce the problem to two dimensions before performing the beam propagation. In the *2D BPM* the calculation window is not discretized in the vertical direction, whence the method is faster than the *3D BPM* (typically several orders of magnitude). The errors in the *2D BPM* stem from the *EIM* method, whence its accuracy increases for wide waveguides ($W/H$ large). A comparison shows that for uniform directional couplers or multi mode interference couplers the results from the *2D BPM* and *3D BPM* have the same functional behavior. Thus the *2D BPM* can be used to examine the wavelength dependency and process tolerance of a given architecture even though it is not exact, but for mask layout it must be supplemented with *3D BPM* simulations. For a detailed comparison see appendix A.

## 2.7 The transfer function and matrix

In the previous section it was sketched how the transfer function of an optical component can be calculated. The transfer function $T$ of an optical component relates the output fields modal amplitude $\Phi$ to the input fields modal amplitude $\Psi$ by:

$$\Phi = T\Psi \tag{2.18}$$

The transfer function is normally written in complex notation as:

$$T = A\exp(i\theta) \tag{2.19}$$

[1] For a standard silica-on-silicon directional coupler the calculation time is on the order of 10 minutes.

where $A$ and $\theta$ are termed the transmission amplitude and phase, respectively. The power transfer is given as the squared norm of the transmission amplitude $P = |A|^2$. From the power transfer the excess loss (in $dB$) is defined as:

$$ExL = -10\log_{10} P \qquad [dB] \tag{2.20}$$

whence the excess loss is zero for a loss less component and decreases with the power transfer. Consider a optical component with $N$ input arms and $M$ output arms, where the arms are counted from top and down. The transfer function from arm $n$ to arm $m$ ($T_{nm}$) is defined as:

$$\Phi_m = T_{mn}\Psi_n \tag{2.21}$$

where $\Psi_n$ is the field amplitude at input arm $n$ and $\Phi_m$ is the field amplitude at output arm $m$.

### 2.7.1 Advantages of the transfer matrix approach

The transfer matrix $\underline{T}$ is given from all the $NxM$ transfer functions:

$$\Phi = \underline{T} \cdot \Psi \tag{2.22}$$

where $\Phi = (\Phi_1, \Phi_2, ..\Phi_M)$ and $\Psi = (\Psi_1, \Psi_2, ..\Psi_N)$ are the total input and output fields, written in vector notation. Consider a device consisting of a cascade of $q$ different components. Here the total transfer matrix $\underline{T}$ is found by matrix multiplication of the individual matrices $\underline{T_i}$:

$$\underline{T} = \underline{T_q} .. \cdot \underline{T_2} \cdot \underline{T_1} \tag{2.23}$$

Accordingly the architecture can be resolved into small modules, which can be modeled independently. Thus the transfer matrix approach allows a hierarchical approach towards modeling complicated components. This enables a solution by using different calculation settings or numerical methods in different parts of the component. An example is to use a combination of *MPA* and *BPM* to model a multi mode interference coupler or to include reflections in a *BPM* analysis [17]. Another advantage is that the transfer matrix for a given component gives a complete description of the component, whence it can be considered as a basic well known building block and does not need to be modeled again. This facilitates making general statements about complicated components consisting of multiple building blocks. As an example consider a Mach-Zehnder

interferometer build of two identical cascaded loss less 3 $dB$ couplers. By matrix multiplication it is seen that the interferometer does not have a unit cross port power unless the two couplers are placed in a point symmetric configuration [19]. The result might seem trivial as standard directional couplers are invariant towards symmetry transformations in both the $x$ and $y$ axis. However, non symmetrical couplers exists (e.g. the uniform asymmetric coupler [20], the series-tapered coupler [21] and the unbalanced Mach-Zehnder interferometer used as coupler [22]). For these coupler types the interferometer will not work if the point-symmetrical rule is not followed.

## 2.8 Wavelength dependency

As this work is concerned with components for $WDM$ networks it is essential to know their spectral response, which is considered in the following section. The relevant wavelength region depends on the application. The entire third telecommunication window covers 1500 to 1600 nm, which is divided into the conventional ($C$), short ($S$) and long ($L$) band, where the $C$-band covers wavelengths of $1525 - 1565$ nm, the $L$-band $1565 - 1610$ nm and the $S$-band $1480 - 1525$ nm. A typical channel spacing is 100 $GHz$ ($\simeq 0.8$ nm).

### 2.8.1 Effects of changing the wavelength

A monochromatic wave with any wavelength can be modeled by using the previously mentioned methods. By repeating this process the entire wavelength region of interest can be sampled with any desired density. To get a feeling for the effects of changing the wavelength the normalized frequency $V$ (eq. 2.14) and the propagation constant $\beta$ are considered. In the weakly guiding approximation the derivative of the normalized frequency with respect to the wavelength is:

$$\frac{dV}{d\lambda} = -\frac{1}{\lambda}V + \frac{2\pi}{\lambda}(\frac{HW}{\pi})^{0.5}\frac{d}{d\lambda}(2n_{co}\Delta n)^{0.5} \tag{2.24}$$

$$\simeq -\frac{1}{\lambda}V \tag{2.25}$$

Hence the derivative of the normalized frequency is negative, i.e. the normalized frequency decreases with the wavelength. Accordingly any waveguide has a wavelength $\lambda_{cut}$, below which it seizes to be single-mode. This wavelength is termed the cutoff wavelength. For a standard step-index fiber the cutoff wavelength is $\lambda_{cut} \simeq 1.2$ $\mu$m.

Another consequence of changing the wavelength is that the propagation constant $\beta$ changes, which is called dispersion. Thus different wavelengths travel with a different speed and loose their synchronization. To quantify this effect the propagation constant can be Taylor expanded in the frequency domain [2]:

$$\beta(\omega) \approx \beta(\omega_0) + \frac{\partial\beta}{\partial\omega}_{\omega_0}(\omega-\omega_0) + \frac{1}{2}\frac{\partial^2\beta}{\partial\omega^2}_{\omega_0}(\omega-\omega_0)^2 + \frac{1}{6}\frac{\partial^3\beta}{\partial\omega^3}_{\omega_0}(\omega-\omega_0)^3 \tag{2.26}$$

where the angular frequency $\omega$ is related to the wavelength by $\omega = \frac{2\pi c}{\lambda}$. For pulses with a small spectral width the first order term of the Taylor series (eq. 2.26) dominates over the other terms and the third order term can be neglected. Thus the envelope of the pulse travels as a whole with a group velocity $v_g = (\partial\beta/\partial\omega)^{-1}$. For a component with length $L$ this leads to a group delay $\tau_g$ of:

$$\tau_g = L\frac{\partial\beta}{\partial\omega} \tag{2.27}$$

If the second order term in eq. 2.26 is negligible the temporal distribution of the pulse is unchanged during propagation, else it leads to pulse deformation and in general pulse broadening in the time domain[2] .Conventionally the second order dispersion is given in terms of the dispersion parameter, defined as:

$$D \equiv \frac{\partial}{\partial\lambda}\left(\frac{\partial\beta}{\partial\omega}\right) = -\frac{2\pi c}{\lambda^2}\frac{\partial^2\beta}{\partial\omega^2} \tag{2.28}$$

The dispersion slope $S$ is:

$$S \equiv \frac{\partial D}{\partial\lambda} \tag{2.29}$$

The number of terms needed in eq. 2.26 grows with the considered wavelength range and length of the system. In a *WDM* network dispersion leads to inter-channel crosstalk and gives rise to a power penalty. Hence it is necessary to have some sort of dispersion control. Normally it is sufficient to compensate for the second order dispersion, but for very demanding systems it can also be necessary to compensate for the dispersion slope (i.e. in ultra long haul systems, systems with high data rates or systems where the *WDM* channels range over a wide wavelength range) [23], [24].

[2] An exception occurs for chirped pulse with a linear frequency chirp $C$. If $Cd^2\beta/d\omega^2 < 0$ the pulse will initially be suppresed.

### 2.8.2 The spectral distribution of an optical pulse

Consider a pulse with a temporal distribution $h(t)$ and duration $\Delta T$. The temporal $h(t)$ and frequency distribution $H(\omega)$ of an optical pulse are interrelated as a pair of Fourier transformations [25]:

$$H(\omega) = \int_{-\infty}^{\infty} h(t) \exp(-i\omega t) dt \tag{2.30}$$

$$h(t) = \frac{1}{2\pi} \int_{-\infty}^{\infty} H(\omega) \exp(i\omega t) d\omega \tag{2.31}$$

whence the temporal duration $\Delta T$ and the spectral width $\Delta\omega$ fulfill:

$$\Delta\omega\Delta T \geqq 1 \tag{2.32}$$

To find the pulse deformation due to a component with a known transfer function it is advantageous to use the frequency domain. The spectral distribution is simply given as the product of the pulse distribution $H(\omega)$ and the components spectral transfer function $T(\omega)$

$$H^{out}(\omega) = T(\omega)H(\omega)$$

whereupon the temporal distribution can be found by 2.31.

## 2.9 Optical filters with discrete delays

Optical filters with discrete delays are fundamentally generalized Mach-Zehnder interferometers, where the incoming light is split into many parts that are delayed with respect to each other by an integer number of discrete units, and finally recombined. This type of filters ranges from simple standard $2x2$ interferometer with different arm lengths to very complex components as e.g. the waveguide grating router or a transversal filter that can be used as multi-channel selectors [25]. The free spectral range $FSR$ of the filters is obtained by setting the phase difference between two interferometer arms to $\Delta\theta = 2\pi$:

$$FSR = \frac{1}{\Delta L} \frac{c}{n_{group}} = \frac{1}{\Delta T} \tag{2.33}$$

where $n_{group}$ is the group index, $\Delta L$ is the path length difference and $\Delta T$ is the unit delay. A typical channel spacing in a $WDM$ network is 100 or 50 $GHZ$.

By eq. 2.33 a $FSR = 100\ GHz$ is equivalent to $\Delta T = 10\ ps$. The periodicity is sometimes also given in the wavelength range (using the free space wavelength). By using $c = f\lambda$ it is seen that:

$$\Delta\lambda \simeq -\frac{\lambda^2}{c}\Delta f \qquad \Delta\lambda << \lambda \tag{2.34}$$

Accordingly $FSR = 100\ GHz$ and $\lambda \simeq 1550\,\mathrm{nm} \Rightarrow \Delta\lambda \simeq -0.8\,\mathrm{nm}$. For a silica-based waveguide with $n \simeq 1.45$, $FSR = 100\ GHz \Rightarrow \Delta L \simeq 2.1\,\mathrm{mm}$.

Normalized parameters are often used to make the description of the filters as general as possible. The normalized frequency $f_N$ is defined as:

$$f_N \equiv \frac{f - f_0}{FSR} \tag{2.35}$$

where $f_0$ is the central frequency of the filter. From the normalized frequency the normalized group delay $\tau_N$ and dispersion $D_N$ are defined as:

$$\tau_N \equiv -\frac{1}{2\pi}\frac{\partial\theta}{\partial f_N} \tag{2.36}$$

$$D_N \equiv -\frac{1}{2\pi}\frac{\partial^2\theta}{\partial f_N^2} \Rightarrow D = -c(\frac{\Delta T}{\lambda})^2 D_N \tag{2.37}$$

where the comparison with the absolute dispersion is based on eq. 2.28, for $FSR = 100\ GHz \Rightarrow D(\ ps/nm) = -12.5 D_N$.

By writing the unit delay as $z^{-1} = \exp(-i\omega\Delta T)$ the transfer function is [25]:

$$T(z) = \frac{\sum_{r=0}^{M} b_r z^{-r}}{1 + \sum_{s=1}^{N} a_s z^{-s}} \tag{2.38}$$

where $b_r$ and $a_s$ are termed the weight coefficient of the filter, and $M$, $N$ are integers. Both the numerator are and denominator are polynomials, their complex roots are termed zeros $(z_r)$ are poles $(\rho_s)$, respectively. As mentioned in section 2.8 the spectral response of an optical component is found from a Fourier transform of its transfer function. For an optical filter with discrete delays the problem simplifies and as the discrete Fourier transform can be utilized. For a filter with a finite maximum delay of $N\Delta T$ the finite Fourier-transform is [25]:

$$H(f) = \sum_{n=0}^{N-1} h(n\Delta T)\exp(-\frac{i2\pi f n\Delta T}{N}) \tag{2.39}$$

$$h(N\Delta T) = \frac{1}{N}\sum_{n=1}^{N} H(f)\exp(\frac{i2\pi f n\Delta T}{N}) \tag{2.40}$$

where $h(N\Delta T)$ is the impulse response of the filter.

## 2.10 Summary

In this chapter some commonly used modeling techniques were described. The chapter gave a description of the scalar wave equation, which is analog to the steady-state Schrödinger equation. It was shown that within the paraxial approximation of the scalar wave equation it is possible to derive normalized parameters. Hence optical components can be scaled from one index step to another. The planar waveguides considered in this work are rectangular. However, the scalar wave equation does not have an analytical solution for rectangular waveguides. Accordingly it is necessary to use numerical mode solvers (as the effective index method and the finite difference method) to solve the wave equation, and a numerical propagation solution (as the beam propagation method) to find the transfer function. The transfer matrix method enables a hierarchical approach to modeling where the total transfer matrix is found from the individual transfer matrices by matrix algebra. Thus the transfer matrix method facilitates modeling of more complicated components. The effects of changing the wavelength was considered and the cutoff wavelength and dispersion parameters were introduced and discussed. Finally the spectral response of optical filters with discrete delays were found from a discrete Fourier analysis of their transfer matrix.

# Chapter 3

# Fabrication and characterization

This chapter describes silica-on-silicon ($SiO_2$ : Si) waveguides and sketch how they are fabricated at *COM*, which is an institute at the Technical University of Denmark. Covering both standard cleanroom fabricated waveguides and waveguides fabricated by direct ultraviolet writing. Some practical limitations in the fabrication and inevitable process variations are discussed and the setup used for characterizing the waveguides is described.

## 3.1 Properties of silica-on-silicon

This work is concerned with passive planar optical components for telecommunications systems. It must be emphasized that for some applications integrated components can not match the performance of fiber components (e.g. a $2x2$ coupler), while for other applications the best solution might be to use micro-optic devices (e.g. an isolator [6]). The main advantage of using planar waveguides is that it enables integration of several components on the same wafer to achieve a complex functionality and decrease the cost and size. Some examples of passive planar optical components are $NxN$ demultiplexers and multiplexers, non-blocking switches[1] and routers, gain and dispersion equalizers and programmable filters [7], [25]. In addition to this there are active planar

[1] For large channel numbers the planar switch can not compete with a *MEMS* based optical switch [26], [5].

components as e.g. semiconductor lasers, electro-optic modulators, wavelength converters and amplifiers.

In this work all waveguides are fabricated in silica-on-silicon, although planar waveguides can also be made with many other materials as e.g. indium phosphide, lithium niobate, silicon oxynitride and polymer materials. In the following the pros and cons of the silica-on-silicon technology shall be sketched.

As the name implies the waveguides are made in doped silica, which is placed on top of a planar silicon wafer. Many of the processes involved in fabricated the waveguides are compatible with silicon technology. This is a major advantage as the latter is well established and has been thoroughly tested. The similarity with fabrication of silica fibers can also be exploited. Silica is highly transparent at the wavelengths used for telecommunication and furthermore has a stable refractive index, enabling a high component reliability [27]. Since the waveguides are made of the same material as optical fibers they have a similar modal field distribution. Therefore silica-on-silicon can be pigtailed directly to standard fibers with a low loss, whereas e.g. indium phosphide waveguides needs mode tapering before the pigtail. Having a simple, low loss pigtail is extremely important as compensation of optical losses increases the system complexity and price and packaging of planar components present a major part of their overall cost [28], [7]. By adding a rare earth dopant to the silica glass the waveguides can be made amplifying to construct e.g. an amplifying array, a laser or a loss less optical splitter [29], [30].

Drawbacks of silica-on-silicon compared to optical fibers include a propagation loss that is several orders of magnitude larger, stress induced problems and birefringence, these topics are addressed in chapter 4. A drawback compared to other integrated waveguides is that silica is amorphous and accordingly has no electro-optic coefficient, whence there is no operating mechanism for high speed switches [28]. However it is possible to pole silica so it obtains an electro-optic coefficient, but the currently achieved coefficients are too small for commercial applications [31].

Silicon is very cheap and readily available. It has a higher thermal conductivity than silica and can thereby act as a heat sink in thermo-optic switches. Furthermore it is possible to etch high precision $V$-grooves into the silicon, which makes passive alignment between fiber and waveguide possible, although such a product is not currently commercially available [32]. Finally the silicon wafer can be used as a laser submount to enable hybrid integration of e.g. a laser and the waveguides [33], [34].

## 3.2 Fabrication

The following section sketches the sequence involved in fabrication silica-on-silicon waveguides at *COM*, covering both our standard process and *UV*-written waveguides. As I have not been involved in the actual processing the description is kept short, a more detailed description can e.g. be found in [18], [35], [36].

### 3.2.1 Standard processing

The majority of the standard cleanroom wafers used in this work have been fabricated at *COM*, but for comparison a few waveguides were fabricated Lucent Technologies Bell Labs. The following description only covers the fabrication process at *COM*.

1. The buffer consists of thermal oxide and is formed by wet oxidation of the silicon wafer. The purpose of the buffer is to shield the core from the silicon (having a refractive index of $n \simeq 3.5$), which can be obtained by having a large buffer thickness. For a step-index of $\Delta n = 0.010$ typical values are $14 - 16\,\mu$m.

2. The subsequent layers are deposited using Plasma Enhanced Chemical Vapor Deposition (*PECVD*), which is a low temperature process ($T \simeq 300\,^{\circ}$C). However, high temperature annealing ($T > 1000\,^{\circ}$C) is necessary between each deposition step to stabilize the glass. The first layer to deposit is the core, which must have higher index than the buffer. The index in the core is raised by adding $GeH_4$ to the plasma, whereby the adsorbed silica film contains $GeO_2$ impurities, which raises its refractive index. Thus the refractive index of the deposited film is controlled by changing the doping concentration of $GeH_4$.

3. After the deposition of the core an irradiation sensitive polymer (photoresist) is spun on top of the wafer. By light exposure through a transparent mask with an opaque pattern, followed by a removal of the exposed photoresist in a developing solution, the pattern of the mask is transferred to the photoresist. Subsequently the remaining photoresist is hardened by baking it. This has the unwanted side effect that the cross-sectional profile of the photo-resist is transformed from nearly rectangular to nearly half circular.

4. The next step is to remove the parts of the core layer that are not covered with photoresist. This is achieved using a Reactive Ion Etch (*RIE*) with

freons as etching agents. The freons have a much higher etch rate for silica than for the hardened photoresist, which accordingly serves as an etch mask. The etching is a very critical step in the fabrication sequence as it determines the waveguide cross section and the side-wall roughness. Therefore all the process parameters should diligently be optimized to obtain a good result. Hereafter the remaining photoresist is removed by an etch in a oxygen plasma that has a much higher etch rate for the photoresist than for the silica.

5. Finally the cores should be covered with topcladding having the same index as the buffer to obtain a symmetric mode and minimize the coupling loss to an optical fiber. The obvious approach is to cover the cores with silica glass. However silica has a very low viscosity and has difficulties with covering the core without giving residual air-bubbles. This is particularly a problem for tightly spacing cores as e.g. in the coupling region of a directional coupler. Accordingly the top cladding is not made of silica. A positive effect of the low viscosity is that it limits the diffusion during the anneal and thus a very small layer of silica is deposited on top of the waveguides to act as a diffusion barrier, accordingly it is termed a barrier-layer.

6. The remaining part of the topcladding consists of boron phosphor silica glass (*BPSG*), which has a higher viscosity than silica glass and gives better coverage of the structures. Boron decreases the refractive index of the film whereas phosphor increases it. So by a suitable choice of the relative concentration the *BPSG* glass obtains the same index as the buffer. The topcladding is deposited in several steps with intermediate annealing to improve the coverage.

The thickness and refractive index of each layer is obtained by comparison with single layer samples measured at 1.55 $\mu$m on a prism coupler, which results in an uncertainty of $\pm 5\%$. The refractive index of the layers have an absolute uncertainty of $\pm 0.001$ and a relative uncertainty of $\pm 0.0002$.

### 3.2.2 Direct *UV*-writing

The directly *UV*-written waveguides that are used in this work are fabricated at *COM*, using the methods described in [37], [38], [39], [40], [36].

1. The starting point is a three silica-on-silicon layer sample, which is fabricated using *PECVD*. The buffer consists of thermal oxide and the top-

cladding of BPSG, while the core layer contains germanium and boron in a proportion, so it matches the refractive index of the surrounding layers. Notice that only the central layer contains germanium and hence it is the only photosensitive layer. For the samples used in this work the thickness of the buffer/core/cladding layer is 16.3 $\mu$m / 5.5 $\mu$m / 11.8 $\mu$m, and the refractive index of each layer is 1.4450/1.4440/1.4440, with uncertainties stated above for standard cleanroom fabricated waveguides. The small unintentional difference in refractive index of the core and cladding with respect to the buffer is caused by slightly mismatched concentrations of germanium and boron.

2. The sample is loaded with molecular deuterium at a temperature of 4 °C and a pressure of 190 bar until saturation, to increase the photosensitivity.

3. The waveguides are fabricated by scanning a sample under a focused 257 nm continuous wave laser beam using high precision three dimensional translation stages. For the waveguides used in this work the beam intensity profile has a measured $1/e^2$ diameter on the sample of 3.1 $\mu$m and a power of 45 $mW$, but other values can also be used. During UV-witting the sample is cooled to $-35\,^{\circ}$C to reduce the rate of $D_2$ out-diffusion. A number of straight waveguides and directional couplers are fabricated with a fixed scan velocity ($v_{scan}$) for each component in the range from 50 $\mu$m / s to 500 $\mu$m / s.

4. After $UV$ processing the sample is annealed to out-diffuse residual deuterium.

It will be shown in chapter 8 that the UV induced index change is several times larger than the unintentional difference in refractive index of the different layers. Thus the asymmetry will only be of minor importance for these waveguides.

Since $UV$-writing does not involve photolithography or etching it requires less cleanroom processing than conventional waveguide fabrication methods. Another strength of the $UV$-writing method is that it does not require a mask with the desired waveguide pattern, which reduces the turnaround time and facilitates having multiple iteration steps in the development of a new optical component. However, the $UV$ induced index change in the core layer occurs by a non-linear process, which is not well understood. Accordingly the refractive index profile of the waveguides is unknown, which makes it problematic to model $UV$-written component, this subject is treated in detail in chapter 8

## 3.3 Practical limitations for standard waveguides

To design any optical component it is essential to know the limitations of the used technology in terms of what can be fabricated, which is the topic of the following section.

### 3.3.1 Waveguide shape and index

By taking scanning electron microscopy (*SEM*) pictures of the waveguide structure after the *RIE* etch, it has been found that our waveguides have nearly vertical side-walls [35], whence a rectangular step-index model seems to be a good description of the waveguides. However, the measured widths on the wafer ($W$) are smaller than the widths on the mask ($W_M$):

$$W = W_M - WWR \tag{3.1}$$

where $WWR$ is the waveguide width reduction. The $WWR$ is caused by the non-rectangular shape of the etch mask and non-idealities of the etch. It is assumed to be symmetrical and thereby the edge-to-edge separation between 2 cores is changed from the mask to the wafer, but the center-to-center separation is constant [18].

To measure the width after the deposition an optical picture was taken of the waveguide. By comparing the waveguide width after the etch and after deposition of the topcladding a further width reduction is apparent (the measurement technique will be described in section 4.2). This unwanted effect is probably caused by diffusion of germanium out of and boron into the waveguide during the anneal of the topcladding, which leads to a graded index profile, where the index is lower at the edge than in the center of the core. This size of this effect can be estimated by measuring the refractive index profile of the core e.g. by scanning near field microscopy [41]. However the measurement techniques are complex and have a limited resolution of approximately $0.5\,\mu$m [42], which is the length scale over which a change can be expected. Therefore such experiments have not performed for standard cleanroom waveguides at *COM*. A possible solution to the diffusion problem is to anneal at lower temperatures. However, this would give a lower flow rate, which might incur problems with the step coverage, but this has not been investigated.

The average $WWR$ for a core fabricated at *COM* with $\Delta n = 0.010$, height $H = 5.5\,\mu$m and mask width $W_M = 7.0\,\mu$m has been measured to be:

$$mean(WWR) \simeq 1.8\,\mu\text{m} \tag{3.2}$$

where it is not a priory clear whether the $WWR$ is independent of the mask width, and therefore the $WWR$ is always measured on a structure with the same mask width (this subject is investigated experimentally in section 4.2). The quoted value of the $WWR$ is for a typical step-index and height. If the step-index is increased the size of the cores must be decreased, to keep them single mode (see section 2.3). A smaller height has been measured to lead to a smaller value of the $WWR$, which is not surprising as the etching depth is reduced.

If the concentration of germanium is too high this leads to problems due to clustering and crystallization of the germanium. At $COM$ it is possible to create germanium doped waveguides with a step-index of up to $\Delta n = 0.027 = 0.02 n_{buf}$ [35], which is comparable to what can be found in the literature [43].

### 3.3.2 Minimum separation between the waveguides

Another problem arises if the waveguides are very close, as it is then not possible to etch the gap between them and subsequently fill it with topcladding. To investigate this effect a set of waveguides with a varying edge-to-edge separation were produced with a step-index of $\Delta n = 0.010$ and a height of $H = 5.5\,\mu$m. Fig. 3.1 shows a bright field picture of a number of pairs of straight waveguides, where the edge-to-edge separation between the waveguides in a pair is growing from left to right. The figure shows that for very closely spaced waveguides a large dark shadow is formed around the waveguide pairs. The shadow is caused by the topcladding not filling the space between the waveguides. Instead air-bubbles (so called key holes) are formed, thus leading to a shadow due to the large difference in refractive index between air and the silica glass. By comparing with the mask documentation it is found that it is not possible to fill the gap for an edge-to-edge separation which is smaller than $2.1\,\mu$m, whence the ratio of the gap to the height is $G/H \simeq 0.38$. As a curiosity it can be mentioned that for an edge-to edge separation between $1.2\,\mu$m and $1.5\,\mu$m no air-bubbles are observed. However, a $SEM$ picture of the waveguides after the $RIE$ shows that the etch does not go all the way down between the cores for an edge to-edge separation of less than $1.6\,\mu$m, whereby this hole is easier to fill.

For waveguides with a smaller height it is possible to etch and fill smaller gaps. A similar experiment for a height of $H = 4.0\,\mu$m showed that it is possible to fill the gap between two waveguides provided their edge-to-edge separation is larger than $1.5\,\mu$m, resulting in a gap to height ratio of $G/H \simeq 0.38$. This suggest that the ratio of the minimum gap to the height is constant for our process.

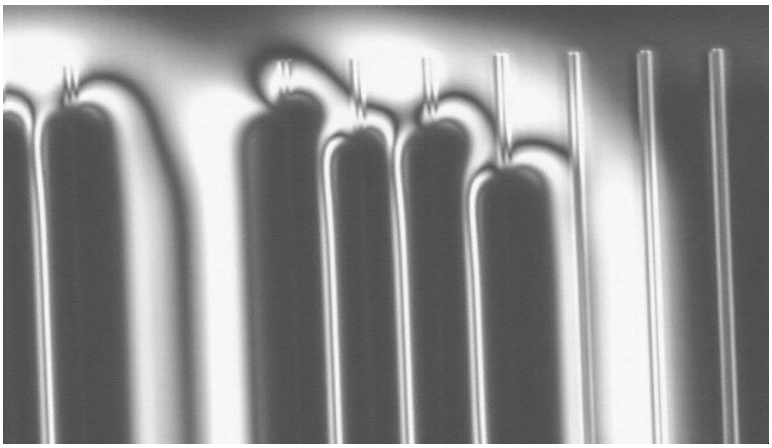

Figure 3.1: An optical picture of groups of two closely spaced waveguides. The separation between the two waveguides in a group is increasing from left to right. The shadows indicates regions where the index is markedly different, which is due to the formation of air-bubbles.

The resolvable limit depends on the widths and shapes of the cores after the *RIE*, whence the minimum resolvable gap on the mask increases if the $WWR$ is reduced. During the Ph.D. project it was initially possible to fill a gap of $2.0\,\mu$m for waveguides with a height of $H = 5.5\,\mu$m. However, due to equipment failure and subsequent replacement it was no longer possible to resolve smaller gaps than $2.2\,\mu$m for a height of $H = 5.5\,\mu$m. As this coincided with the arrival of a new mask it rendered a number of components on the mask impossible to fabricate (see section 5.3).

## 3.4 Process variations

Another major concern is to minimize the size of the inevitable variation in the process parameters during the fabrication process, to ensure a high yield of the fabricated optical components.

As described in the previous section it is assumed that the standard clean-room fabricated waveguides can be described by a step-index distribution. Thus they are characterized by a height $H$, width $W$ and step-index relative to the

| | $\delta\Delta n$ | $\delta H$ | $\delta W$ |
|---|---|---|---|
| Uniformity across wafer | $\pm 3 \cdot 10^{-5}$ | $\pm 0.1\%$ | $\pm 0.2$ $\mu$m |
| Reproducibility | $\pm 2 \cdot 10^{-4}$ | $\pm 0.1\%$ | $\pm 0.2$ $\mu$m |

Table 3.1: The uniformity and reproducibility of standard waveguides at COM

cladding $\Delta n$. This implies that the process tolerance can be modeled by examining the effects of variations in these three parameters. Define the deviation $\delta x$ of a parameter $x$ by:

$$\delta x \equiv x_{meas} - x_{des} \tag{3.3}$$

where $x_{meas}$ is the measured and $x_{des}$ is the design value of the parameter $x$. Notice that by eq. 3.1 the deviation in width and $WWR$ have different sign:

$$\delta W = -\delta WWR \tag{3.4}$$

It must be emphasized that there are two different types of process variations, one is occurring from the degree of uniformity across a wafer and the other from the wafer to wafer reproducibility. Table 3.1 shows an estimate of the process variation at *COM* [35], [18].

The step-index uniformity across the wafer is an order of magnitude better than the reproducibility, whereas for the two other parameters the variations have similar magnitude.

Finally it is worth noticing that clean room processing is not static and it is therefore necessary to monitor the process and make minor adjustments to keep the waveguide parameters within acceptable limits [18].

### 3.4.1 Use of optical test structures

In the previous section it was shown how to extract information about the waveguides by direct measurements to serve as input for simulations of waveguide components. A supplement hereto is to include optical test structures on the wafer to reveal some of the properties of the constituent waveguides, as the characterization results from an optical test structure can give the desired property without making any further assumptions about e.g. the refractive index profile of the waveguides.

The simplest possible test structure is a straight waveguide. In spite of its simplicity it is possible to extract a lot of useful information from measurements

on straight waveguides, which is the subject of the next chapter. Another useful structure is a Mach-Zehnder interferometer from which it is possible to extract information about the coupling strength in directional couplers, which gives feedback about the confinement in the waveguides. A sensible choice of optical test structures depends on the content of the mask, but in general the test structures should not be too large nor process tolerant. The purpose of including the test structures is to give feedback on the waveguide parameters and therefore they should not give identical response if the process varies.

An alternative to having optical test structures on each mask is to fabricate a standard test mask containing all the individual test structures. By subsequently processing a wafer using the test mask in every batch of wafers, it is possible to monitor the process in great detail.

## 3.5 Optical characterization

By optical characterization is meant that light is sent through the device under test, and either the transmission or the reflection is measured.

### 3.5.1 Optical sources

In this work the light used for the characterization comes from either a laser, a polarized *ASE* source or an unpolarized white light source.

#### Laser

The laser is a distributed feed back (*DFB*) fiber laser, which lases in a single polarization with a wavelength of 1556.78 nm and a peak power at the wafer of $-30\ dBm$. The laser has a side mode suppression ratio of more than 20 $dB$ and a spectral full width at half maximum of 0.06 nm. By comparison with an atomic emission line from a gas cell the peak wavelength of the laser has been observed to be stable within the measurement uncertainty.

#### Polarized *ASE* source

The *ASE* source is integrated with a polarizer and is henceforth referred to as a polarized *ASE* source. The *ASE* power spectrum at the wafer is measured on a optical spectrum analyzer (*OSA*). Fig. 3.2*A* shows the measured power spectrum from $\lambda = 1507$ nm to 1607 nm using an optical resolution of $res = 0.1$ nm. The spectrum has local maxima at $\lambda = 1533$ nm and $\lambda = 1557$ nm, where the

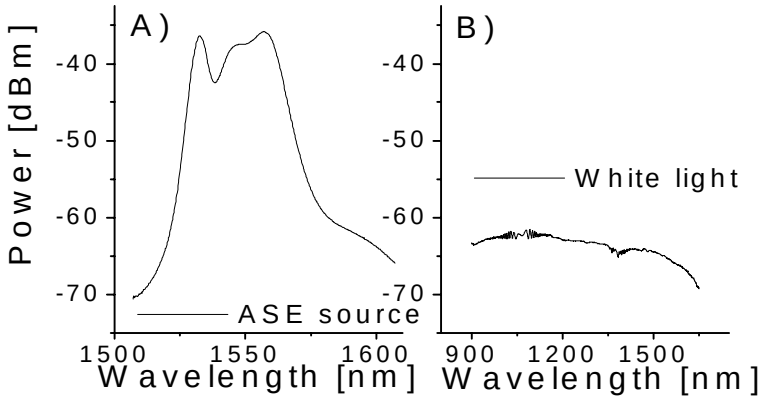


Figure 3.2: The power spectrum at the wafer of $A$) the polarized $ASE$ source ($res = 0.1\ nm$) and $B$) the white light source ($res = 2.0\ nm$).

power in both cases is $P \simeq -36\ dBm$. The spectral width at $-10\ dB$ relative to the maximum is $\Delta\lambda \simeq 39$ nm, whereas the width at $-30\ dB$ relative to the maximum is $\Delta\lambda \simeq 88$ nm. The noise floor of the $OSA$ is at approximately $P \simeq -80\ dBm$, which is lower than the measured power over the entire wavelength range in fig. 3.2$A$. Thus the $ASE$ source can be used to measured the transfer function over a wavelength range of up to 100 nm with the considered resolution. However, during a part of the Ph.D. project there was problems with the characterization setup, whereby the power at the wafer was 16 $dB$ lower than these value. Therefore some of the measurements of the spectrum of optical couplers suffer from a low signal to noise ratio close to the edges of the wavelength interval (see section 5.3).

**White light source**

For measurements of the spectrum from 900 nm to 1600 nm an unpolarized white light source is used. Fig. 3.2$B$ shows a $OSA$ measurement of the spectrum at the wafer, which is obtained using a resolution of $res = 2.0$ nm (thus the measured power is approximately 13 $dBm$ higher than if a resolution of $res = 0.1$ nm were used). The recorded spectrum is very flat as the power is between $-62\ dBm$

and $-69\ dBm$ from $\lambda = 900\,\text{nm}$ to $\lambda = 1600\,\text{nm}$. However, the power level is very low and therefore the light has not been sent through a polarizer as this would result in a power loss of 3 $dB$, bringing the power very close to the noise floor of the $OSA$.

### 3.5.2 Transmission and reflection measurements

Fig. 3.3 shows a schematic of the characterization setup used in this work. The light comes from an optical source with a fiber output. From the source the light is sent though an isolator and a fiber optical tap coupler. The small reference signal from the cross arm of the coupler is sent directly to a detector (#1). The purpose of the reference signal is to monitor fluctuations in the output power of the source, for which it is possible to compensate. The remaining part of the light (from the bar arm of the coupler) is sent through a polarization controller, a circulator and then to the device under test ($DUT$). Stripped standard single mode fiber are butt coupled directly to the $DUT$, where index matching oil is used between the fibers and $DUT$ to minimize reflections and increase the precision of the measurements. The position of the input and output fibers are manually optimized by using high precision translation stages. The reflection and transmission from the device under test goes to a $2x1$ mechanical optical switch and then to another detector (#2). By changing the settings of the switch it is determined whether the transmission or reflection is detected. If the transmission or reflection spectrum is needed an optical spectrum analyzer ($OSA$) can be used as detector.

It should be noticed that the characterization setup is different for measurements with the unpolarized white light source, where the polarization controller, circulator and optical switch have been removed due to the low power level of the source. Furthermore, standard single mode fibers are not single mode at wavelengths below $\lambda \simeq 1.2\ \mu\text{m}$, which poses a problem for the low wavelength range of the measurements. Accordingly the standard fibers are replaced by fibers that are single mode down to $\lambda \simeq 0.8\ \mu\text{m}$.

#### Measurement uncertainty

The measurement uncertainty of the power transfer is estimated from multiple measurements of the same component, whereby it is found to be:

$$\delta P \simeq \pm 0.1\ dB \tag{3.5}$$

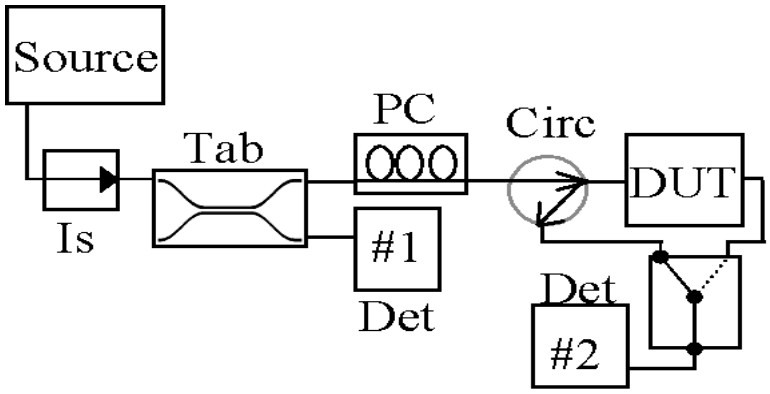


Figure 3.3: The characterization setup used to measure the transmission or the reflection of the device under test ($DUT$). The isolated is denoted $Is$, the polarization controller $PC$, the detectors by $Det$, the circulator by Circ and the device under test by $DUT$.

The characterization setup has a polarization dependent loss of

$$PDL_{ch} \simeq 0.05 - 0.1 \; dB \tag{3.6}$$

which gives a limit for the determination of the $PDL$ of the characterized components.

By measuring the peak wavelength of the $DFB$ fiber laser on the $OSA$ the measured value was found to drift up to 0.01 nm on a time scale of 30 min. This is a problem if the wavelength of a sharp peak in a power spectrum is to be recorded. Accordingly the peak wavelength of the $DFB$ laser is measured immediately after each measurement of a resonance wavelength, whereby the instantaneous value of the drift is measured and can be subtracted. The compensated wavelength $\lambda_{comp}$ is:

$$\lambda_{comp} = \lambda_{meas} - \delta\lambda^{laser} \tag{3.7}$$

where $\lambda_{meas}$ is the measured wavelength and $\delta\lambda^{laser}$ is the deviation of the wavelength of the $DFB$ fiber laser from its nominal value. The obtainable relative uncertainty between two sharp wavelength peaks $\delta\lambda_{rel}$ is estimated

from multiple measurements of the same components:

$$\delta\lambda_{rel} \approx 2 - 3 \cdot 10^{-3}\,\mathrm{nm} \tag{3.8}$$

## 3.6 Summary

In this chapter the fabrication sequences used for standard cleanroom waveguides and *UV*-written waveguides at *COM* have been sketched. A number of practical fabrication limitations for standard waveguides are discussed, in particular with respect to the obtainable index difference and the minimum allowable separation between two waveguides. Based on *SEM* and optical microscopy pictures of the standard waveguides it seemed reasonable to assume that the waveguides can be described by a rectangular step-index profile. Accordingly the waveguides are determined by their step-index relative to the buffer $\Delta n$, height $H$ and width $W$, and the uniformity and reproducibility of these quantities are discussed. The obtained uncertainties shall be used in later chapters to simulate the process tolerance of optical components. It is mentioned that the measured width is smaller on the mask, and the deviation between the two quantities is termed waveguide width reduction $WWR$.

Finally the chapter described the characterization setup used for measuring the transmission and reflection spectra of optical components. A *DFB* fiber laser, a polarized *ASE* source and a white light source was used in the characterization, whence it was possible to measure the transfer function from 900 nm to 1600 nm. It was shown that by careful alignment of the fibers to the waveguide and compensating for the fluctuations in the power of the source, the uncertainty of the measured power transfer can be kept at $\delta P = \pm 0.1\ dB$. The relative uncertainty on the measurement of multiple sharp wavelength peak was estimated to be $\delta\lambda_{rel} \approx 2 - 3 \cdot 10^{-3}\,\mathrm{nm}$.

# Chapter 4

# Straight waveguides

This chapter describes a number of measurements on straight waveguides that are produced either as standard waveguides or as $UV$-written waveguides. The measurements include coupling, propagation and polarization dependent loss, as well as the width and birefringence of the waveguides. All the waveguides have been fabricated at *COM*, using the methods described in section 3.2. The measurements are obtained at a wavelength of $\lambda = 1557\,\mathrm{nm}$.

## 4.1 Waveguide losses

The power transfer of a straight waveguide is measured by butt-coupling standard single mode fibers to the waveguide, as sketched in section 3.5. Recall from section 2.7 that the excess loss (in $dB$) is obtained from the power transfer $PT$ by:

$$ExL = -10\log(PT) \tag{4.1}$$

The excess loss of a straight waveguide stems from coupling loss (due to mismatch between the fiber and waveguide mode and misalignment between the fiber and waveguide) and propagation loss in the waveguide (which in passive silica-on-silicon waveguides is mainly due to side wall roughness of the waveguide [44], [45]). For a straight waveguide with length $L_{st}$ the total excess loss is:

$$ExL = 2CpL + PL \cdot L_{str} \tag{4.2}$$

where $CpL$ is the coupling loss per facet and $PL$ is the propagation loss per length unit.

By scanning the polarization the excess loss varies, giving rise to a polarization dependent loss:

$$PDL = \max(ExL) - \min(ExL) \tag{4.3}$$

Polarization dependent loss is detrimental as the polarization in a telecommunication system is unknown and fluctuating.

### 4.1.1 Standard waveguides

The following measurements are for standard waveguides with step-index $\Delta n = 0.010$ and height $H = 5.5\,\mu$m. The propagation loss $PL$ is estimated by measuring the loss of straight waveguides having the same width and different lengths, for standard widths of $W_M \approx 7\,\mu$m this gives:

$$PL \approx 0.02 - 0.03\ dB/\,\mathrm{cm} \tag{4.4}$$

which is a low value for integrated waveguides, but 4 orders of magnitude larger than the propagation loss for a standard optical fiber. The polarization dependent loss $PDL$ is estimated from a measurement of a straight waveguide with length $L = 30\,$mm:

$$PDL_{str} < 0.1\ dB \tag{4.5}$$

where the quoted value contains a unknown contribution from polarization dependent coupling loss. A more accurate determination can be obtained by measuring the total polarization dependent loss for a number of different waveguides with different length. This has not been performed.

To find the coupling loss a number of waveguides with length $L = 30\,$mm and different mask width were fabricated. If the width is increased from the standard value (up tapering) the effect is primarily to change the horizontal width of the mode, whereas the vertical width is nearly unchanged. As the step index of the considered waveguide is higher than the standard fibers, the waveguides mode size is smaller than the fibers. By up tapering it is possible to match the horizontal width of the waveguide mode to that of the fiber, but the vertical mode remains smaller. Thus it is not possible to achieve perfect mode match and zero coupling loss. If the width is decreased from the standard value (down tapering) this leads to a decrease in confinement, which eventually leads

to an increase in mode size in both directions. For a suitable down tapering it is possible to obtain a mode with similar dimensions as that of the standard fiber leading to a low loss.

Fig. 4.1 shows the measured coupling loss per facet $CpL$ as a function of the waveguide mask width, as well as a finite difference ($FD$) method simulation, where it has been assumed that the fiber mode is Gaussian and has a waist of $5.0\,\mu$m. To plot the simulated and measured coupling loss on the same axis the simulated widths have been inflated by the average $WWR$ of $1.8\,\mu$m. The simulated curve has two local minimums at $W_M \simeq 4.5\,\mu$m and $W_M \simeq 12.0\,\mu$m of which the first is a global minimum, these are referred to as the down and up tapered minimum. For the down tapered minimum the coupling loss is very sensitive towards changes in the width, whereas the up tapered minimum is quite shallow. Thus it is easier to produce waveguides with low coupling loss by up than by down tapering the waveguide width. In general fig. 4.1 shows good agreement between the measured and simulated curves, although it was not possible to produce down tapered waveguides with a low coupling loss. The measured curve confirms that for up tapered waveguides the coupling loss is quite insensitive towards changes in the width. A waveguide with $W_M \approx$

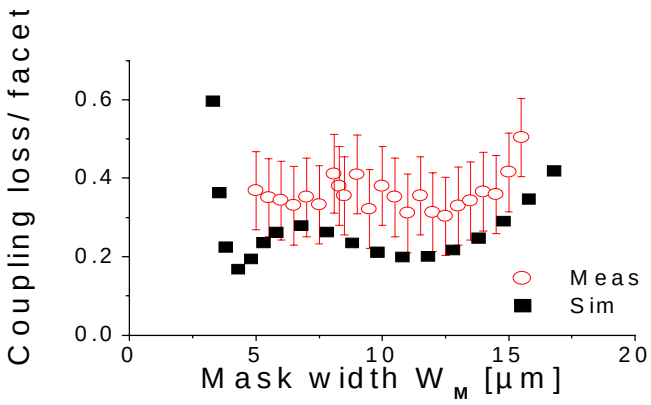


Figure 4.1: The measured and simulated coupling loss per facet of a straight standard waveguide as a function of the waveguide mask width.

$12.0\,\mu$m is multi mode and in general multi mode waveguides are unwanted in optical components. A solution to this problem is to use a wide waveguide

width at the output of the wafer, which is adiabatically tapered down to the desired width to ensure single mode operation. Hereby both low coupling loss and single mode operation in the critical areas of the wafer can be achieved [46].

If the step-index of the waveguide is increased and the waveguide dimensions are scaled to fix the normalized frequency the size of the waveguide mode decreases. This increases the coupling loss to standard fibers. As an example consider a step-index core with $\Delta n = 0.029 = 0.02 n_{buf}$ and a height of $H = 3.0\,\mu$m. The down tapered minimum occurs at $W \approx 1.0\,\mu$m giving a coupling loss to a standard fiber of $CpL \approx 0.5\ dB/facet$, whereas the up tapered minimum occurs at $W \approx 12.0\,\mu$m with a loss of $CL \approx 1.5\ dB/facet$, which shows that the coupling loss from the process tolerant up tapered minimum increases rapidly with the step-index. To solve this problem the loss can be decreased by coupling to a fiber with a smaller mode than the standard fiber or a lensed fiber [47], or by changing the waveguide mode in both the horizontal and vertical direction. This can be achieved by using segmented tapers [48], [49] or vertical tapers [50], [51].

### 4.1.2 *UV*-written waveguides

A similar investigation has been performed for $UV$-written waveguides. For the used laser power of the writing beam 45 mW the total excess loss has a shallow minimum close to $v_{scan} = 200\,\mu\text{m}/\text{sec}$. As the investigation was performed for rather short waveguides it is difficult to completely separate the coupling and propagation loss, but an estimate of the quantities is:

$$CpL \simeq 0.2 - 0.3\ dB/facet \tag{4.6}$$

$$PL \simeq 0.1 - 0.2\ dB/\text{cm} \tag{4.7}$$

The coupling loss has approximately the same size as for the previously considered standard cleanroom fabricated waveguides (with $\Delta n = 0.010$), but the propagation loss is somewhat higher. Pictures of the $UV$-written waveguides indicate that the propagation loss could be caused by gas turbulence over the wafer during the $UV$-writing, and it is currently being investigated whether this problem can be solved, by encapsulating the waveguides in a vacuum chamber during the writing process.

The polarization dependent loss over the entire range of scan velocities was measured to be:

$$\max(PDL) < 0.2\ dB \tag{4.8}$$

where the $PDL$ at scan velocities between 100 and 200 $\mu$m / sec was on the order of 0.1 $dB$, which is the measurement limit of the current setup (see section 3.5)

## 4.2 Width of straight waveguides

The following section describes measurements of the widths of waveguides after the deposition of the topcladding. The width is measured by imaging each waveguide in bright field illumination with an optical microscope equipped with a charge coupled device camera, where it must be emphasized that such images do not give the refractive index profile of the waveguides. The imaging is performed in blue light to increase the resolution, which for this imaging setup was measured to be 0.4 $\mu$m (Airy disc full width at half maximum). Hence, it is an order of magnitude smaller than a typical waveguide width. The width measurements were performed by Anders Harpøth.

### 4.2.1 Standard waveguides

The following measurements are for standard waveguides with step-index $\Delta n = 0.0081$ and height $H = 6.1\,\mu$m. An image of a standard cleanroom fabricated waveguide with a mask width of $W_M = 7.5\,\mu$m is shown in fig. 4.2$A$. The waveguide is slightly brighter than the background, but the salient feature is that a series of bright and dark bands surround the waveguide core. Fig. 4.2$B$ shows the normalized profile of the pixel count perpendicular to the waveguide axis. By comparing pictures for slightly different focus positions of the microscope it is seen that the edge between the central waveguide region and the strongest dark line (marked by an arrow in fig. 4.2$B$) is insensitive to small deviations in the focus position. This must correspond to the waveguide edge since defocussing changes the image sharpness, but not the image scale. The conclusion is confirmed by dark field illumination, which shows scattering - and thus a large index gradient - along two lines coinciding with the two edges on the bright field picture.

The image scale is determined by imaging two closely spaced waveguides with an accurately known center-to-center separation. From independent measurements of the same waveguide the standard deviation on the measured width is found to be 0.04 $\mu$m.

The width of straight waveguides was measured as a function of the width on the mask, which is depicted in fig. 4.3. The figure also shows a linear fit to the measurements, which has a slope of $1.03 \pm 0.01$, and it is clear that the

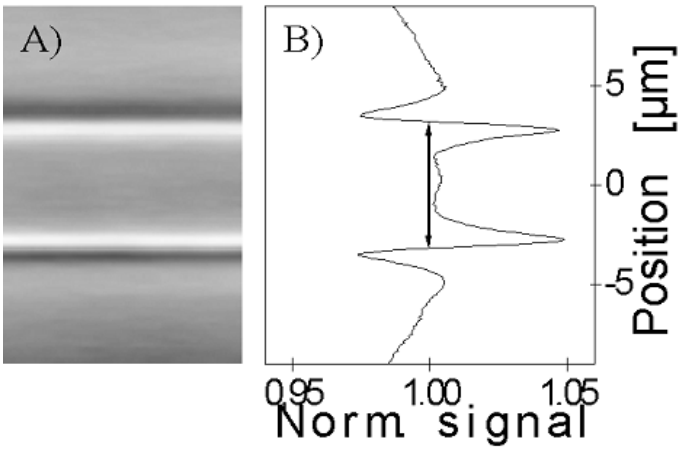


Figure 4.2: The figure shows $A$) on optical bright field picture of a standard waveguide with $W_M = 7.5\ \mu m$ and $B$) the normalized pixel count perpendicular to the waveguide axis.

agreement between the measurements and the fit is excellent. Notice that the slope from the fit is very close to unity. This gives the apparently trivial result that the measured width can be found from the mask width by subtraction of a constant. However this conclusion has the non trivial implication that the waveguide width reduction $WWR$ is constant as a function of the waveguide width.

### 4.2.2 *UV*-written waveguides

The $UV$-written waveguides can not be expected to have a step-index profile. In prior work it has been suggested that the index change decays exponentially in the vertical direction due to strong $UV$ absorption [52]. It is also reasonable to assume that the index distribution in the horizontal direction could be approximated by a Gaussian function, since this is the form of the $UV$-writing beam. However by taking optical pictures of the waveguides it can be examined whether it makes sense to assign some width to the waveguides.

Fig. 4.4 shows a corresponding image of a $UV$-written waveguide. The figure shows a similar pattern as on fig. $4.2A$, with the exception that it contains a

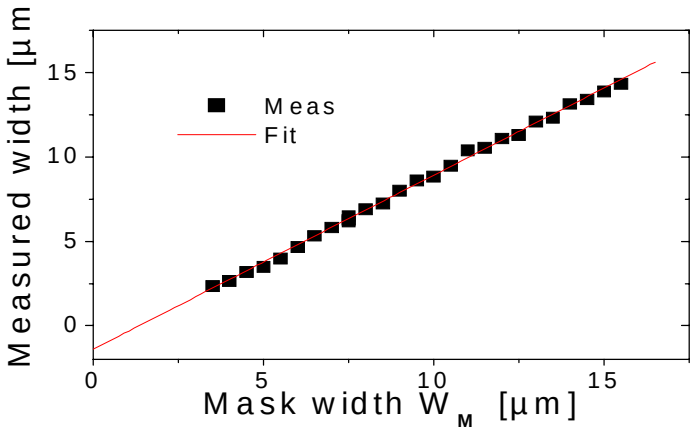


Figure 4.3: The measured width of standard waveguides with $\Delta n = 0.0081$ and $H = 6.1\,\mu$m as a function of the mask width $W_M$. Also shown is a linear fit to the measurements, the fit has a slope of $1.03 \pm 0.01$.

more complex structure of bands within the waveguide. This shows that the index profile of $UV$-written waveguides is more complex than a simple square profile. Furthermore the figure shows a fluctuation of the waveguide edge, which was not present in the cleanroom waveguide. The fluctuation can be due to imperfect movement of the laser beam over the wafer or a fluctuation of the air turbulences over the wafer during the writing process. Fig. 4.4*B* shows the normalized vertical profile of the pixel count for two slightly different focus positions of the microscope. Again the edge between the central waveguide region and the strongest dark line is insensitive to small deviations in the focus position. Therefore a width is assigned to the waveguide as illustrated in fig. 4.4*B*.

Fig. 4.5 shows the assigned width as a function of the scan velocity applied during $UV$-writing. In general the measured values are roughly two times larger than the $UV$ spot size. Furthermore the width decreases with the scan velocity, even though the $UV$ spot size does not change. These observations indicate that the index change process induced by the $UV$ exposure is saturated in the central regions of the exposed area.

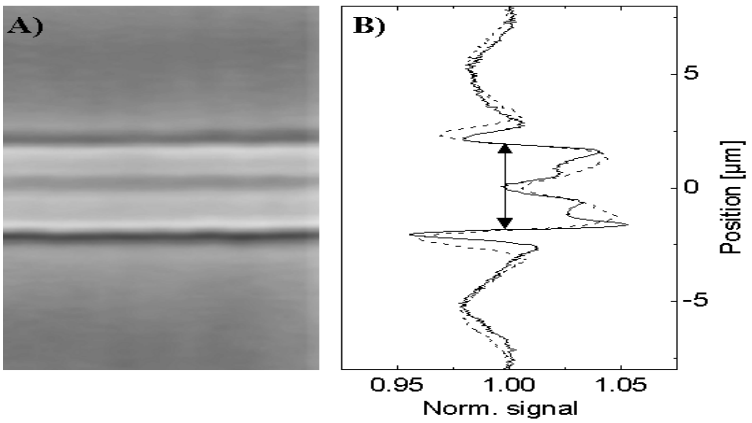


Figure 4.4: *A*) an optical bright field image of a $UV$-written waveguide and *B*) the image intensity perpendicular to the waveguide axis for two slightly different focus positions of the optical microscope. The assigned waveguide width, as shown by the arrow, is independent of the focus position.

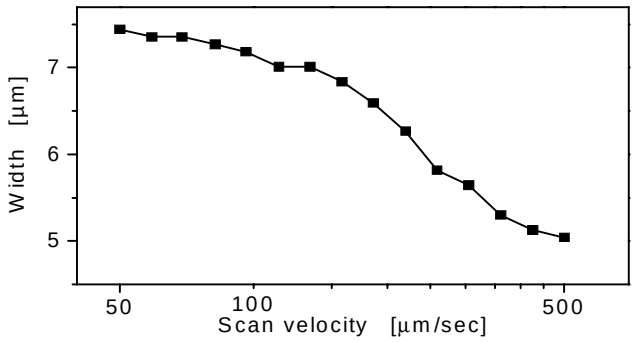


Figure 4.5: The measured width of $UV$-written waveguides as a function of the applied scan velocity. The spot size of the laser beam is 3.1 $\mu m$, roughly a factor of two smaller than the measured widths.

## 4.3 Birefringence of straight waveguides

By inscribing a Bragg grating into a waveguide its effective index can be found as the grating gives rise to resonances for wavelengths $\lambda_{Br}$ given by the Bragg formula:

$$\lambda_{Br} = n_{eff}\Lambda \tag{4.9}$$

where $\Lambda$ is the mask period and $n_{eff}$ is the effective index of the mode.

The accuracy of the measurement depends on the width of the resonance and the accuracy of the detector. As the UV exposure raises the index of the waveguide and the width of the resonance increases with the strength of the grating, it is advantageous to inscribe a weak Bragg grating. The width of the resonance furthermore decreases with the length of the grating. The Bragg resonance is most clearly seen by measuring the reflection spectrum of the waveguide. The measurements of the effective index have an absolute uncertainty on the order of $1 \cdot 10^{-5}$ and a relative uncertainty (between the indices of different waveguides) of a few times $10^{-6}$.

If the waveguide has several guided modes the spectrum has several peaks, where the strength of a particular resonance is determined by the power in that mode. For each mode there is two resonances, one for *TE* and another for *TM* polarized light. By using the polarized *ASE* source and a polarization controller the power in the two resonances can be changed to ensure that the light at the wavelength of the resonance is polarized either in the plane of the wafer (*TE* polarization) or perpendicular to the plane of the wafer (*TM* polarization). Recall that the birefringence is defined from eq. 2.15 as:

$$\Delta n_{eff} = n_{eff}^{TE} - n_{eff}^{TM} \tag{4.10}$$

whence it is positive if $n_{eff}^{TE} > n_{eff}^{TM}$. The birefringence measurements of the standard waveguide were performed by Maja Albertsen, Anders D. Jensen and Johnny H. Olsen, whereas the measurements of the *UV*-written waveguides were performed by Anders Harpøth.

### 4.3.1 Standard waveguides

The following measurements are for standard waveguides with step-index $\Delta n = 0.010$ and height $H = 5.5\,\mu$m. A Bragg grating has been inscribed to the waveguides through a phase-mask with a period of 1071 nm leading to resonance wavelengths close to 1550 nm (see eq. 4.9).

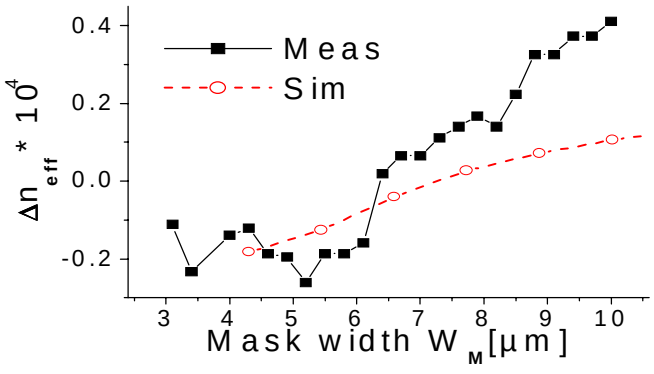


Figure 4.6: The measured birefringence of standard waveguides with $\Delta n = 0.010$ and $H = 5.5\,\mu$m as a function of the mask width $W_M$. The figure also contains a *FD* simulation of the geometrical birefringence.

Fig. 4.6 shows the measured birefringence of the zero order mode as a function of the mask width of the standard waveguides. The figure also shows a *FD* method simulation of the geometrical birefringence, where the simulated widths have been inflated by the average $WWR$ of $1.8\,\mu$m. Hence a core with a mask width of $W_M = H + WWR = 7.30\,\mu$m has zero geometrical birefringence. Fig. 4.6 shows good agreement between the measurements and the simulations. For a mask width below $8.0\,\mu$m the measured birefringence is less than $\delta n_{eff} < 2.0 \cdot 10^{-5}$ showing that standard waveguides have very low birefringence. However, for large widths the measured birefringence grows faster than the simulated birefringence.

A part of this work is devoted to understanding multi mode interference couplers (see chapter 5), whence the birefringence at a large width is important. Accordingly a Bragg grating is inscribed into very wide multi mode waveguides having mask widths up to $110\,\mu$m. The wide waveguides have several guided modes and therefore the reflection spectra have several peaks. Recall from section 2.1 that the effective index and the resonance wavelength decreases with the mode number, whereby the zero order mode corresponds to the peak at the largest wavelength. Fig. 4.7 shows the measured birefringence and simulated geometrical birefringence for the zero order mode of very wide waveg-

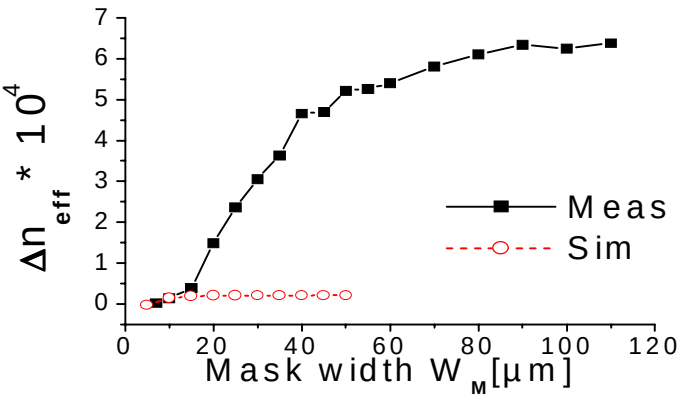


Figure 4.7: The measured and simulated (geometrical) birefringence for the zero order mode as a function of the waveguide width for very wide standard waveguides with $\Delta n = 0.010$ and $H = 5.5\,\mu$m.

uides. The measured birefringence is much larger than the simulated geometrical birefringence and furthermore the difference is increasing with the width. For the largest simulated width of $W = 50\,\mu$m the geometrical birefringence is $\Delta n_{eff} \simeq 2.0 \cdot 10^{-5}$ whereas the measured birefringence is $\Delta n_{eff} \simeq 5.0 \cdot 10^{-4}$, i.e. a factor of 25 larger. A measurement of the birefringence for the first and second order mode of the waveguides showed a similar dependency both with respect to the functional form and size of the birefringence. Accordingly the measured birefringence is so large that components using very wide waveguides must be expected to suffer from a large polarization dependency.

The birefringence can be caused by several effects such as insufficient shielding of the core from the silicon wafer, non rectangular core shape, non isotropic diffusion of germanium out of and boron into the core and non isotropic stress in the film. The non isotropic stress is caused by that the different glass layers having different viscosity, e.g. the viscosity of the core layer depends on its germanium concentration. However, the three first mentioned effects should have largest effect for small cores and therefore can not explain the unexpected birefringence at large waveguide width. It is expected that the stress field in the silica film depends on the width of the waveguide, but the dependency has not

been measured. Accordingly it can not be determined whether a stress induced effect can explain the large observed birefringence.

### 4.3.2 *UV*-written waveguides

A similar experiment was performed for *UV*-written waveguides, but this time a grating period 1057.09 nm was used, yielding resonances at a wavelength of approximately 1530 nm.

Fig. 4.8*A* shows the measured effective index for the *TM* polarization $n_{eff}^{TM}$ as a function of the scan velocity. As expected, the effective index decreases with the scan velocity from approximately 1.4508 at $v_{sc} = 50\,\mu\mathrm{m}/s$ to 1.4485 at $v_{sv} = 500\,\mu\mathrm{m}/s$. When the waveguides become very weak the effective index converges towards that of the slab structure. This convergence value has been estimated by inducing progressively weaker waveguides (using low power of the *UV*-writing beam and high scan velocities). For the weakest waveguides it is only possible to observe a Bragg reflection for the *TM* polarization. This is interpreted as the propagation loss being so large for the other polarization that it hinders detection of any reflection. If the waveguide was made slightly weaker no guiding could be observed for either polarization. The convergence value determined in this way is marked as a dashed line in fig. 4.8*A*. Fig. 4.8*B* shows the measured birefringence (multiplied by $10^4$) as a function of the scan velocity. The figure shows that the birefringence in general is low, it is negative for small scan velocities but positive for large scan velocities. A comparison with fig. 4.5 shows that the width of the UV written waveguides decreases with the scan velocity. Thus the birefringence decreases with the width of the waveguides, in contrast to what was found for standard cleanroom waveguides. The physical reason for the birefringence is unknown, but it is believed to be caused by non uniform stress. For a scan velocities of approximately $200\,\mu\mathrm{m}/\,\mathrm{sec}$ the birefringence is zero. In the interval between $120\,\mu\mathrm{m}/s$ and $250\,\mu\mathrm{m}/s$ its absolute value is below $5.0 \cdot 10^{-5}$, while for values between $50\,\mu\mathrm{m}/\,\mathrm{sec}$ and $400\,\mu\mathrm{m}/\,\mathrm{sec}$ it is below $5.0 \cdot 10^{-5}$. Accordingly any specification of a maximum allowable birefringence can be met by choosing the appropriate range of scan speeds.

## 4.4 Summary

This chapter described a number of measurements of both standard cleanroom fabricated and *UV*-written straight waveguides. The width of the standard

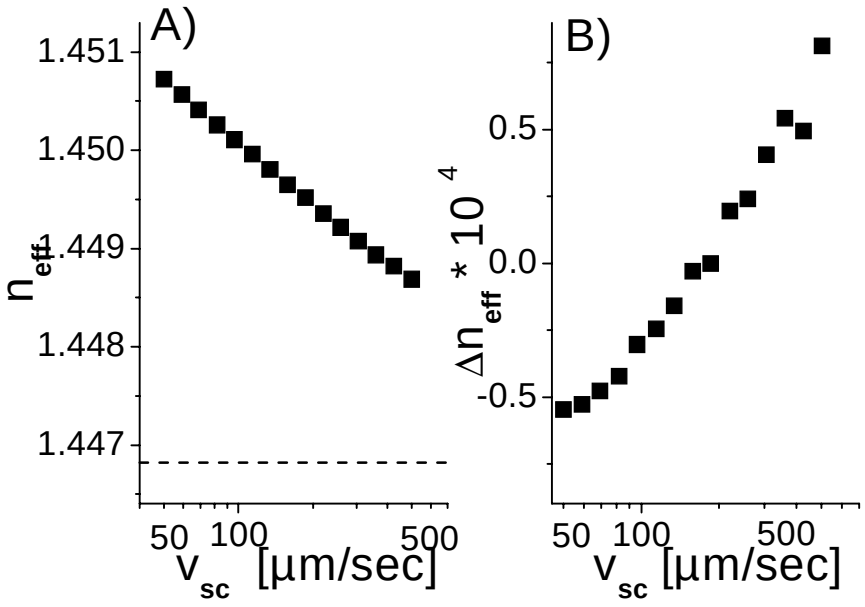


Figure 4.8: *A*) the measured effective index of *UV*-written waveguides for the *TM* polarization ($n_{eff}^{TM}$) as a function of the applied scan velocity. The dotted line shows the estimated effective index value for the slab structure. *B*) the measured birefringence (times $10^4$). The birefringence is negative for small scan velocities, crosses zero for a scan velocity of approximately $200\,\mu\mathrm{m}/s$, whereupon it becomes positive.

waveguides was measured using optical microscopy and a criterion for achieving high precision measurements were found. It was shown that the width on the wafer was obtained from the mask width by subtraction of a constant, which implied that the waveguide width reduction was independent of the waveguide width. Waveguides with a step-index of $\Delta n = 0.010$ and height $H = 5.5\,\mu$m were shown to have a coupling loss of 0.3 $dB/facet$ to a standard fiber, where the loss could be slightly decreased by using a wide waveguide. The propagation loss ($PL \simeq 0.02$ $dB/$cm), polarization dependent loss ($PDL \simeq 0.1$ $dB$) and birefringence ($\delta n_{eff} < 2.0 \cdot 10^{-5}$) were also low for standard waveguides with mask widths below $8\,\mu$m. However, the measured birefringence was large for very wide multi mode waveguides. A comparison with simulations of the geometrical birefringence showed that the measured birefringence was more than an order of magnitude larger than the geometrical birefringence. Furthermore the discrepancy was increasing with the waveguide width. A potential candidate to explain the observed effect is non uniform stress, but this has not been tested. The measured large birefringence indicated that components using very wide waveguide width (as e.g. multi mode interference couplers) might have a large polarization dependency.

A similar set of measurements for $UV$-written waveguides showed that the coupling loss and polarization dependent loss were similar to those of the standard waveguides, but the propagation loss was a factor of $5 - 10$ larger ($PL \simeq 0.1 - 0.2$ $dB/$cm). This presents a problem for very long components. It was possible to assign a width to the $UV$-written waveguides. The assigned width decreased with the scan velocity, but was roughly a factor of two larger than the spot size of the laser beam used to write the waveguides, which indicated that the index change process induced by the $UV$ exposure was saturated in the central regions of the exposed area. Measurements of the effective index of the $UV$-written waveguides showed a decrease with the scan velocity, meaning that the size of the $UV$ induced change increased with the fluence. The measured birefringence in general was low, but varied with the scan velocity achieving zero birefringence at a scan velocity of approximately $v_{scan} \simeq 200\,\mu$m / sec. By choosing an appropriate range of scan speeds any specification of a maximum allowable birefringence can be met.

# Chapter 5

# Optical 3 $dB$ couplers

This chapter describes planar $2x2$ optical 3 $dB$ couplers, optimized with respect to process tolerance and wavelength-flattened coupling from 1500 nm to 1600 nm. Three different types of couplers are examined: uniform directional couplers, interferometer based couplers and multi mode interference (*MMI*) couplers, and simulations show that of these the *MMI* couplers have the best performance. The experimental data for the directional couplers agrees reasonably well with the simulations, although complete agreement can not be obtained within the step-index model for the waveguides. For the *MMI* couplers a larger discrepancy is observed with an unexpected large polarization sensitivity and imbalance between the output arms. A numerical investigation shows that a parabolic error in the index distribution, which e.g. can be caused by non uniform stress, can explain this effect. This postulate is corroborated by experiments showing that the imbalance can be removed by $UV$-trimming the *MMI* coupler. These observations show that the process tolerance of *MMI* couplers is less than what has previously been assumed.

Parts of this chapter has been published in the journals *Optical and Quantum Electronics* [53] and *News of the Danish Optical Society* [54], while other parts were presented at the conference *Integrated Photonics Research* in 2000 [55] and 2001 [56].

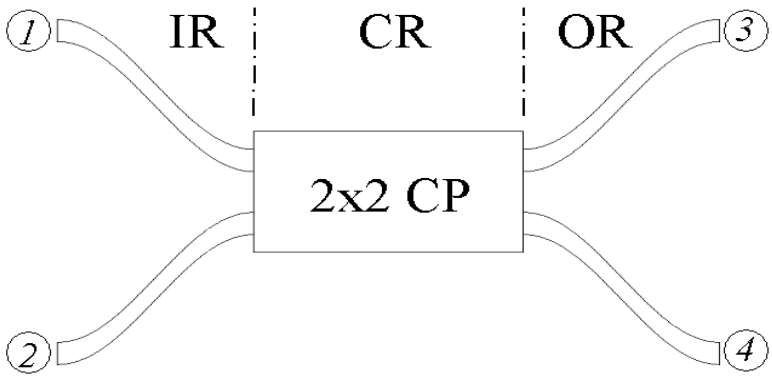


Figure 5.1: Schematic of a $2x2$ coupler, where the access arms are numbered from top and down. The dotted vertical lines mark the transitions between the input region (IR), central region (CR) and output region (OR).

## 5.1 Introduction

Before describing the optical couplers the notation for 3 $dB$ couplers and the method used for simulating the process tolerance are sketched and the choice of coupler architectures is commented.

### 5.1.1 Notation

A general $2x2$ coupler is shown in fig. 5.1. It can be divided into an input region, a central region and an output region. In the input/output region the waveguides follow a smooth $S$-shaped curve, whence their center-to-center separation is increased/decreased without leading to a large loss.

For a loss less coupler the transfer matrix is unitary [57]. Denote the transfer function from arm $r$ to arm $s$ by $T_{rs}$ to obtain the following transfer matrix [19]:

$$\underline{T} = \begin{bmatrix} T_{13} & T_{14} \\ T_{23} & T_{24} \end{bmatrix} = \begin{bmatrix} a & -b^* \\ b & a^* \end{bmatrix} \tag{5.1}$$

where $a, b$ are complex, $b^*$ denotes the complex conjugate of $b$ and $|a|^2 + |b|^2 = aa^* + bb^* = 1$. Notice from eq. 5.1 that $P_{13} = |a|^2 = aa^* = |a^*|^2 = P_{24}$ and $P_{14} = P_{23}$. The power transfer of the coupler is determined from $P_{13}$ and $P_{14}$ and

these are denoted the bar ($P_b$) and the cross coupling ($P_c$), respectively. Instead of using the bar and cross coupling the 3 $dB$ coupler is often characterized by its imbalance and excess loss. The imbalance $IMB$ (in $dB$) is defined as:

$$IMB = 10\log\frac{P_b}{P_c} = 10\log(P_b) - 10\log(P_c) \qquad [dB] \tag{5.2}$$

the imbalance is zero for an ideal coupler, is positive if $P_b > P_c$ and negative if $P_c > P_b$. To get a feeling for the scale of the imbalance a linear fit was imposed to the imbalance over the region from $0.3 < P_c < 0.7$. The fit, which has excellent accuracy, becomes:

$$IMB \simeq 9.0 - 18.0P_c \qquad 0.3 < P_c < 0.7 \tag{5.3}$$

which shows that a imbalance of 0.5 $dB$ corresponds to a cross coupling of approximately $P_c \approx 0.47$, whereas 1 $dB$ corresponds to $P_c \approx 0.44$. The excess loss (in $dB$) is defined from the total power transfer:

$$ExL = -10\log(P_b + P_c) \qquad [dB] \tag{5.4}$$

whereby the excess loss is zero for a loss less component, is non negative for passive optical components and increases with the loss.

### 5.1.2 Simulating the process tolerance

To examine the process tolerance recall that our waveguides resemble step-index waveguides (see chapter 3), whence the process variations can be described by changes in the three parameters: waveguide width reduction $WWR$, waveguide height $H$ and waveguide step-index $\Delta n$. To compare the importance of the individual parameters a normalized deviation is defined:

$$\delta_{Norm} \equiv \frac{x_{Ac} - x_{Des}}{\max(x_{Ac} - x_{Des})} = \frac{\delta x}{\max(\delta x)} \tag{5.5}$$

where $x_{Ac}$ is the actual value, $x_{Des}$ is the design value, max is the maximum value operator and $\delta x$ is the deviation of the process parameter $x$. The maximal deviations depend on the details of the processing. At $COM$ they are (see chapter 3):

$$\begin{aligned} \max(\delta WWR) &= 0.2\,\mu\text{m} \\ \max(\delta H) &= 0.1\,\mu\text{m} \\ \max(\delta\Delta n) &= 2\cdot 10^{-4} \end{aligned} \tag{5.6}$$

By using the normalized deviation it is possible to compare the importance of the individual parameters directly by plotting all of them on the same graph. However, such a plot only gives the results of changing one parameter, whereas in reality it is possible that several parameters deviate from the design values. Accordingly it can be argued that one should examine what happens if all the parameters vary independently of each other and e.g. create contour plots of the desired property as a function of two or three process parameters [18], but this increases the number of simulations dramatically. As the aim of this investigation is to estimate the process tolerance whence it was decided to vary one parameter at the time.

For all the considered couplers the step-index is chosen to be: $\Delta n = 0.010$, which is a relative change of 0.7%. The chosen step-index is a compromise between having low coupling loss to standard fibers (requires low $\Delta n$) and small component size (requires large $\Delta n$). A core height of $H = 5.5\,\mu$m is used for all components. As mentioned in section 2.2 the devices can be scaled without effecting the performance, provided that the index difference $\Delta n$ is scaled by $x$, the length by $1/x$ and the height and width by $1/\sqrt{x}$. The process tolerance at the new step-index can be found from the original simulations by scaling the maximal deviations in accordance to the scaling laws. For a scaling factor of $x$ this implies that:

$$\begin{aligned} \max[\delta WWR(x)] &= x^{0.5} \max[\delta WWR] \\ \max[\delta H(x)] &= x^{0.5} \max[\delta H] \\ \max[\delta \Delta n(x)] &= x \max[\delta \Delta n] \end{aligned} \tag{5.7}$$

where it should be emphasized that eq. 5.7 is only valid for a theoretical evaluation of the process tolerance at the new step-index, and not to give the maximal deviation of the process parameters at the new step-index.

### 5.1.3 Choice of architecture

This investigation covers uniform directional couplers, unbalanced Mach-Zehnder couplers and multi mode interference (*MMI*) couplers. However, there are also other possibilities as e.g. the point symmetric series tapered coupler [21], [18] and the adiabatic coupler [58], [59], [60].

In the point symmetric series tapered couplers the central region consists of three tapered sections. Thus it has larger design flexibility than the uniform couplers and allows a wavelength flat behavior. Initially this project was collaboration with Dan Zauner, where he found that the point symmetric series

tapered coupler inherently has low process tolerance [18], whence it was decided not to continue the work on this coupler type.

In the adiabatic coupler the two waveguides are dissimilar at the start of the central region of the coupler. An input from the wide arm will only excite the zero order supermode of the coupler. By adiabatically changing the widths of the two arms the shape of the supermode changes[1]. If the widths are interchanged this gives a 100% coupler, whereas equal output widths will result in a 3 $dB$ coupler [58], [59]. The adiabatic coupler has wavelength-flattened-performance and good process tolerance, but is rather long. For a 3 $dB$ coupler another complication arises because the output waveguides are identical. Thus the output of the coupler is identical to that of a uniform directional coupler, whence the light couples between the waveguides in the output bends leading to an unwanted oscillatory wavelength response.

Another possibility is a symmetric $1x2$ $Y$-branch splitter, which by symmetry has equal power in the two arms and good process tolerance. A drawback of the $Y$-branch splitter is that it is a three port device whereas the other components are four port devices. This limits the possible applications e.g. a three port device can not be used to construct an interferometer type optical switch[2] as it will only have one output waveguide.

It should furthermore be mentioned that the coupling coefficient between two waveguides can be changed by post-fabrication methods as heating [62] or $UV$-trimming ([63], [64]) the coupler. However, this complicates the fabrication process and therefore is an undesirable solution.

## 5.2 Theoretical investigation

The simulations presented in this chapter are performed using either a $2D$ or a $3D$ $BPM$ for a monochromatic wave that is polarized with the electric field parallel to the plane of the wafer ($TE$ polarization), whereupon the wavelength dependency is found by calculating the response at selected wavelengths over the region of interest (see section 2.8). For the considered couplers the results from the two simulation methods have the same functional form (see appendix A) and therefore the $2D$ $BPM$ can be used to give qualitative predictions for

[1] An alternative way of adiabatically changing the asymmetry is to bend the waveguides in the plane of the couplers, where the bent region is skewed towards one end of the coupler waist [61].

[2] In silica-on-silicon the phase at the second coupler is typically controlled by heating the interferometer arms to change their total path length.

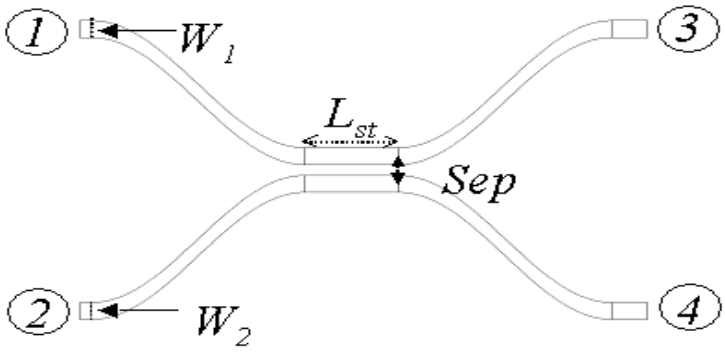


Figure 5.2: Schematic of a uniform symmetric directional coupler. The waveguides have widths of $W_1$ and $W_2$, the coupling region has length $L_{str}$ and center-to-center separation of $Sep$.

the wavelength-flatness and process tolerance. Although the method in general is inaccurate, whence the asymptotically correct $3D$ $BPM$ is used to fine tune the designs before they are fabricated.

### 5.2.1 Directional couplers

The uniform directional coupler is the waveguide equivalent of the fused fiber coupler, where uniform means that the waveguides are uniform in the central region. Generically it is a loss less component, whence the output power is given solely from either the bar or the cross coupling. The directional coupler functions by evanescent wave coupling between two closely spaced waveguides. Hence the central region of a directional coupler is termed the coupling region. Fig. 5.2 shows a uniform directional coupler, where the waveguides have widths of $W_1$ and $W_2$, center-to-center separation between the waveguides in the coupling region $Sep$ and the length of the coupling region $L_{st}$. Instead of using the center-to-center separation the edge-to-edge gap $G_{E2E}$ can also be used. It is:

$$G_{E2E} = Sep - 0.5(W_1 + W_2) \tag{5.8}$$

The directional coupler can be described by either the coupled mode or the supermode theory. In the coupled mode theory the total field is assumed to be a superposition of the fields of the unperturbed waveguides. The characteristic parameter of the problem is the coupling coefficient $C$, which can be found from [57]:

$$C = 0.5(n_c - n_b)k_0[\frac{\int\int_{A_{core2}} \Psi_1(\Psi_1^* + \Psi_2^*)dA}{\int\int_{R^2} \Psi_1(\Psi_1^* + \Psi_2^*)dA} - \frac{\int\int_{A_{core2}} \Psi_1(\Psi_1^* - \Psi_2^*)dA}{\int\int_{R^2} \Psi_1(\Psi_1^* - \Psi_2^*)dA}] \tag{5.9}$$

where $\Psi_1, \Psi_2$ are the fields of the undisturbed waveguides, $A_{core2}$ is the area of core 2 and $R^2$ is the plane perpendicular to the propagation axis. The field of an isolated waveguide is exponentially decreasing outside its core, whence the coupling coefficient decays rapidly with increasing center-to-center separation between the waveguides.

In the supermode theory the wave-equation is solved for the two-core structure in the coupling region. Unless each of the two cores is extremely weakly guiding [65], [66] the two-core structure will support two so called supermodes, with propagation constants $\beta_0^S$ and $\beta_1^S$. If both modes are excited this will lead to a periodic oscillation of the power between the two waveguides. The coupling length is defined as the length required to transfer all the power from one waveguide to the other (half the period of the oscillation):

$$L_{cp} = \frac{\pi}{(\beta_0^S - \beta_1^S)} = \frac{\lambda}{2(n_{eff,0}^S - n_{eff,1}^S)} \tag{5.10}$$

where the effective indices of the supermodes are denoted as $n_{eff,0}^S$ and $n_{eff,1}^S$, respectively. The two descriptions are equivalent and the coupling coefficient $C$ and coupling length $L_{cp}$ are related by [8]:

$$C = (\beta_0^S - \beta_1^S) = \frac{\pi}{L_{cp}} \tag{5.11}$$

Even though the coupling coefficient decreases rapidly with the separation between the waveguides there is some coupling in the input and output region of the coupler. It has been shown that this can be described by an equivalent length $\delta L_b$, that should be added to the length of the coupling region [8]:

$$L = L_{st} + \delta L_b \tag{5.12}$$

Hereby maximum cross coupling is achieved at $L_{st} = L_{cp} - \delta L_b$. The equivalent length $\delta L_b$ depends on the shape of the bends, the confinement in the waveguides and the wavelength [13]. The product of the coupling coefficient and total length is termed the coupling strength and is denoted by $\phi$:

$$\phi \equiv CL \tag{5.13}$$

**Uniform symmetrical couplers**

In the uniform symmetrical (*US*) coupler the two waveguides have identical propagation constant. The transfer function of the *US* coupler is [67]:

$$\underline{T}^{UA} = \begin{bmatrix} \cos(CL) & -i\sin(CL) \\ -i\sin(CL) & \cos(CL) \end{bmatrix} \tag{5.14}$$

where the output from arm 3 and 4 are $\pi$ radians out of phase. The cross coupling is:

$$P_c^{US} = \sin^2(CL) \tag{5.15}$$

whence a 3 $dB$ design is obtained at $CL = (2r-1)\cdot\pi/4$ where $r \in N$. Normally the first cross point $CL = \pi/4$ is chosen, as it gives the shortest possible coupler and has larger wavelength-flatness and process tolerance than the higher order cross points. A wavelength-flattened 3 $dB$ coupler requires that $dC/d\lambda = 0$, which is obtained close to the cutoff wavelength of the second order mode of the composite structure [67], [68]. This has been used to design a coupler with wavelength-flattened behavior [69], [66]. However, the waveguides have an edge-to-edge separation of $\simeq 1\,\mu$m, whereby the cores are far too close for the design to be producible at *COM* (see section 3.3)[3]. To the best of my knowledge a *US* coupler with $dC/d\lambda = 0$ has never been fabricated. In any case this possibility has not been further investigated in the present work.

Before comparing the sensitivity with regards to the individual process parameters the functional form of eq. 5.15 is analyzed, as it can be assumed that fabrication variations to first order will lead to variations in the coupling coefficient. Hence the cross coupling is differentiated with respect to the coupling coefficient:

$$\frac{dP_c^{US}}{dC} = 2L\sin(CL)\cos(CL) \tag{5.16}$$

[3] It is also possible to achieve $dC/d\lambda = 0$ for a larger edge-to-edge gap [67], but this requires that the cores have a very low normalized frequency, which will lead to large bend losses.

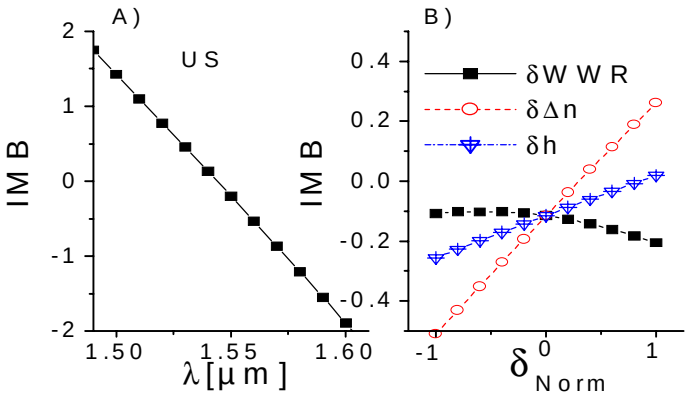


Figure 5.3: The simulated imbalance (in $dB$) of a $US$ coupler (which is insensitive towards variations in the $WWR$) as a function of $A$) the wavelength and $B$) the normalized process deviation $\delta_{Norm}$.

which is zero for a 0% and a 100% coupler, whereas it reaches its extremes for a 3 $dB$ coupler. Thus meaning that the 3 $dB$ coupler is difficult to produce as small deviations in the coupling strength lead to a large change in the cross coupling.

Fig. 5.3$A$ shows the wavelength response of a $US$ coupler with $W_1 = W_2 = 4.0\,\mu$m, $Sep = 9.0\,\mu$m and $L_{st} = 420\,\mu$m. The design is chosen because it is insensitive towards changes in the $WWR$ (see below). Its wavelength response is typical for $US$ couplers and shows that the imbalance changes linearly with the wavelength. For the considered design the slope is $-0.0033\ dB/$ nm showing that the imbalance changes 3.3 $dB$ over 100 nm.

Fig. 5.3$B$ shows the imbalance as a function of the normalized deviation $\delta_{Norm}$ (see eq. 5.5) in the $WWR$, step-index and height. The figure shows that the imbalance increases with both the step-index and the height. The reason is that an increase in either the height or the step-index will lead to an increase in the normalized frequency $V$, inducing a decrease in the coupling coefficient, whereby the imbalance increases (since the coupling strength is $\phi = \pi/2$). Fig. 5.3$B$ also shows that the imbalance is rather insensitive towards changes in the $WWR$. If the $WWR$ increases the confinement decreases which incurs

an increase in coupling coefficient. However, the edge-to-edge separation also increases, which leads to a decrease in coupling coefficient. Accordingly there exists a $WWR$ where the effects cancel each other and the coupling coefficient has an extremum (which is a minimum) [70]. This is basis of the chosen design, which to first order is independent of variations in the $WWR$. For this particular $US$ coupler the step-index is the most critical process parameter, where the considered limits leads to a deviation of up to 0.4 $dB$ from the nominal value.

**Uniform asymmetrical couplers**

In the uniform asymmetrical ($UA$) coupler the waveguides have different propagation constant ($\Delta\beta = \beta_2 - \beta_1 \neq 0$), which e.g. can be achieved by having different waveguide widths, i.e. $W_1 \neq W_2$. For the $UA$ coupler the transfer matrix is given as [67], [71]:

$$\underline{T}^{UA} = \begin{bmatrix} \cos(\kappa L) - i\Delta\beta(2\kappa)^{-1}\sin(\kappa L) & -iC\kappa^{-1}\sin(\kappa L) \\ -iC\kappa^{-1}\sin(\kappa L) & \cos(\kappa L) + i\Delta\beta(2\kappa)^{-1}\sin(\kappa L) \end{bmatrix} \tag{5.17}$$

where $\Delta\beta = \beta_2 - \beta_1$ is the difference between the propagation constants of the two (undisturbed) waveguides and the asymmetric coupling parameter $\kappa$ is:

$$\kappa = \sqrt{0.25\Delta\beta^2 + C^2} \geq C \tag{5.18}$$

Notice from eq. 5.17 that the output at arm 3 and 4 are not $\pi$ radians out of phase unless the coupler is symmetric, i.e. has $\Delta\beta = 0$. The cross coupling of the $UA$ coupler is:

$$P_c^{UA} = (\frac{C}{\kappa})^2 \sin^2(\kappa L) \tag{5.19}$$

where $(C/\kappa)^2 < 1$ gives the cross coupling amplitude for the $UA$ coupler. Eq. 5.19 shows that a change in the asymmetric coupling coefficient $\kappa$ affects both the cross coupling amplitude $(C/\kappa)^2$ and the coupling strength $\kappa L$. Like for the $US$ coupler the coupling coefficient has a maximum for closely spaced cores, which can be used to design an asymmetric 3 $dB$ coupler with a very wavelength flat cross coupling [66]. But the cores are far too close for the coupler to be fabricated at our process lab, and for all practical realizable couplers the coupling coefficient increases with the wavelength.

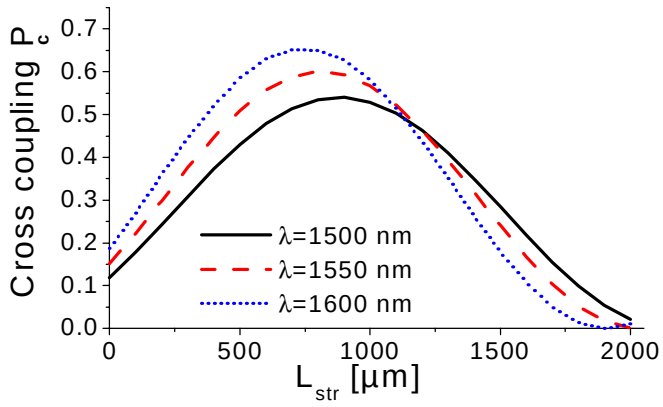


Figure 5.4: A $2D$ *BPM* simulation of the cross coupling for a *UA* coupler with: $W_1 = 5.70\,\mu$m, $W_2 = 4.95\,\mu$m and $Sep = 9.13\,\mu$m as a function of the length of the coupling region $L_{st}$ for three different wavelengths.

To examine the functional form of eq. 5.19 the cross coupling amplitude is differentiated with respect to the symmetrical coupling coefficient $C$:

$$\frac{\partial}{\partial C}(\frac{C}{\kappa})^2 = \frac{8C\Delta\beta^2}{\left(0.25\Delta\beta^2 + C^2\right)^2} > 0 \tag{5.20}$$

which shows that the cross coupling amplitude increases with the coupling coefficient. An increase in the symmetrical coupling coefficient, while keeping the waveguides unchanged ($\Delta\beta$ fixed), can be obtained by decreasing the separation between the waveguides. To first order it can also be obtained by increasing the wavelength, which shows that the cross coupling amplitude increases with the wavelength [71]. Thus both the asymmetric coupling coefficient $\kappa$ and the cross coupling amplitude $(C/\kappa)^2$ increases with the wavelength for all practical *UA* couplers. Consider the oscillatory term in eq. 5.19. A simple evaluation shows that the term increases with the coupling coefficient $\kappa$ for $0 < \kappa L < \pi/2$, whereas it decreases with the coupling coefficient and hereby the wavelength for $\pi/2 < \kappa L < \pi$. Thus wavelength-flattened 3 $dB$ coupling is achieved by a careful choice of $(c/\kappa)^2$ and $\kappa L$. Wavelength-flattened *UA* couplers have previously

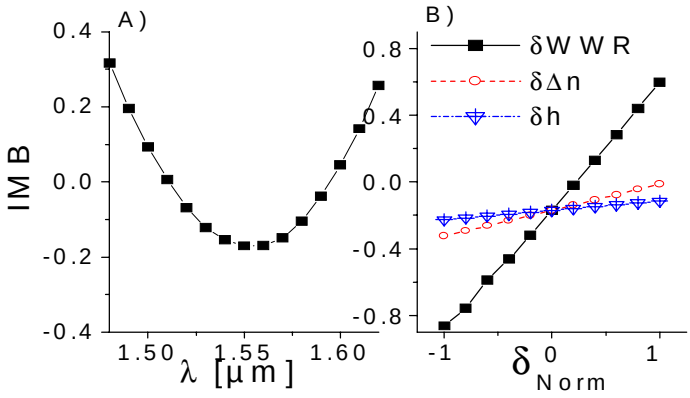


Figure 5.5: The simulated imbalance (in $dB$) of a $UA$ coupler as a function of $A$) the wavelength and $B$) the normalized process deviation $\delta_{Norm}$.

been reported both theoretically and experimentally [72], [20], [71].

Fig. 5.4 shows a $2D$ $BPM$ calculation of the cross coupling $P_c$ of a $UA$ coupler as a function of the length of its coupling region $L_{st}$ for the three wavelengths, $\lambda \in \{1500, 1550, 1600\}$ nm . The $UA$ coupler has: $W_1 = 5.70\,\mu$m, $W_2 = 4.95\,\mu$m and $Sep = 9.13\,\mu$m. The figure shows that when the wavelength increases from 1500 nm to 1600 nm the cross coupling amplitude increases from 0.54 to 0.66, whereas the length giving a maximum cross coupling decreases from 0.88 mm to 0.74 mm. Furthermore fig. 5.4 shows that for a length of $L_{st} = 1.1$ mm the cross coupling is very close to 0.50 for the three considered wavelengths. Thus this design has wavelength-flattened coupling from 1500 to 1600 nm. Fig. 5.5$A$ shows the simulated imbalance as a function of the wavelength for the above chosen $UA$ coupler, where $L_{st} = 1.12$ mm. It is seen that the imbalance has a minimum at $\lambda = 1.55\,\mu$m and only varies 0.2 $dB$ from 1500 nm to 1600 nm, which confirms that the design is wavelength-flattened.

Fig. 5.5$B$ shows the imbalance as a function of the normalized deviation $\delta_{Norm}$ in the waveguide width reduction, step-index and height. The imbalance is seen to increase with all three parameters. For the step-index and height the magnitude of the change is small, and with respect to these parameters the $UA$ coupler is more process tolerant than the $US$ coupler. However, deviations in

the $WWR$ leads to a change of imbalance of up to 0.8 $dB$ from the nominal value making the $UA$ coupler very sensitive to changes in the $WWR$.

To understand the effects of the deviations the cross coupling amplitude $(C/\kappa)^2$ and coupling coefficient $\kappa$ for the $UA$ coupler (see eq. 5.19) are found as a function of the process parameters. For the considered design an increase of $\delta WWR = 0.2$ induces a change of $\delta(C/\kappa)^2 \simeq -7\%$ and $\delta\kappa \simeq 1\%$. A numerical investigation shows that in general an increase in the $WWR$ incurs a large decrease in the maximal coupling amplitude and a small increase in the coupling coefficient. To achieve tolerance towards varying $WWR$ thus requires that a small change in coupling coefficient has a large effect, i.e. that $d\sin^2(\kappa L)/d\kappa$ is negative and large. A comparison with fig. 5.4 shows that the wavelength-flattened design is achieved close to the maximum cross coupling, where $d\sin^2(\kappa L)/d\kappa$ is small. Thus it is not possible to create a wavelength-flattened $UA$ coupler, which is insensitive to variations in the $WWR$. Accordingly the wavelength-flattened coupler is very sensitive towards variations in the $WWR$.

### 5.2.2 Unbalanced Mach-Zehnder interferometer couplers

Fig. 5.6 shows a schematic of the unbalanced Mach-Zehnder interferometer ($UMZI$) coupler. It consists of two $US$ couplers with coupling strengths of $\phi_1$ and $\phi_2$, whereas the phase difference in the interferometer arms is $2\theta$. In the figure the phase change is obtained by having a length difference $\Delta L$ between the arms, where $2\theta = \beta\Delta L$, but it could e.g. also be obtained by heating one of the arms to change its refractive index and thereby its total path length. The $UMZI$ coupler is assumed loss less (it consists of loss less components), whereby the coupling characteristics can be described by the cross coupling.

The basic idea of the unbalanced $UMZI$ coupler is to introduce an out-of-phase factor between the couplers to prevent the cross coupling from monotonically increasing with the wavelength. The operation may be viewed as error cancellation where a proper phase shift ensures that the second coupler cancels the deviations introduced by the first, provided that the deviations are similar in the two couplers. The design can be fabricated as either a planar [22] or a fiber component [73]. The cross coupling of the $UMZI$ can be found from a transfer matrix calculation [74]:

$$P_c^{UMZI} = \cos^2\theta\sin^2(\phi_1+\phi_2) + \sin^2\theta\sin^2(\phi_1-\phi_2) \tag{5.21}$$

The purpose of the unbalance is to introduce a phase change $0 < 2\theta < 2\pi$ and not to induce a periodic response as described for the filters with discrete delays

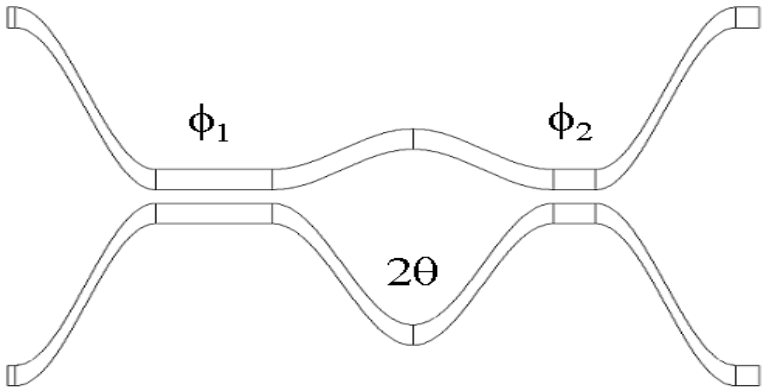


Figure 5.6: An *UMZI* coupler, which consists of two different *US* couplers with coupling strengths $\phi_1$and $\phi_2$ and interferometer arms with a phase delay of $2\theta$, where $\theta < \pi$.

(see section 2.9). To clarify this point consider the maximal phase difference of $2\theta = 2\pi$ and assume wavelength independent coupling. By eq. 2.33 this would result in a periodic response with a $FSR$ equal to the frequency of the light, whence the assumption of wavelength independent coupling clearly falls.

A wavelength-flattened design can be obtained by a numerical optimization of $\phi_1$, $\phi_2$ and $\theta$. Since $\cos^2\theta + \sin^2\theta = 1$ eq. 5.21 shows that $P_c^{UMZI}$ is limited by the two envelope functions $\sin^2(\phi_1 + \phi_2)$ and $\sin^2(\phi_1 - \phi_2)$, where the weight of the two terms depends on the phase $\theta$. The optimization approach is to choose $\phi_1$ and $\phi_2$ so that $\sin^2(\phi_1 + \phi_2)$ and $\sin^2(\phi_1 - \phi_2)$ is close to the desired coupling ratio in each their end of the wavelength region, and choose $\theta$ to ensure the correct evolution of the weight factors [22]. By using the Frechett-Powell optimization method a wavelength-flattened response can be found for cross coupling coefficients between 0% and 80%, whereas the design is not suitable for wavelength-flatness at higher cross couplings [19]. For a cross coupling coefficient that is equal to or less than 50% it is furthermore possible to find an analytical solution for the wavelength-flattened response, which for a 3 $dB$ coupler gives [74], [75]:

$$\phi_1 = \frac{\pi}{2} \qquad \phi_2 = \frac{\pi}{4} \qquad 2\theta = \frac{2\pi}{3} \tag{5.22}$$

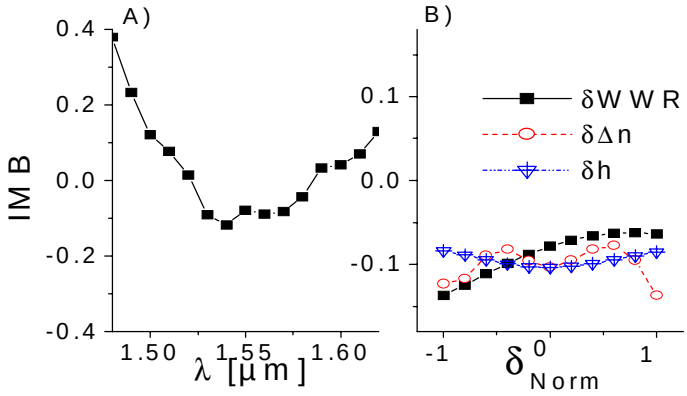


Figure 5.7: The simulated imbalance (in $dB$) of an *UMZI* coupler as a function of $A$) the wavelength and $B$) the normalized process deviation $\delta_{Norm}$.

whereby the length difference between the interferometer arms is:

$$\Delta L = \frac{2\theta}{\beta} = \frac{\lambda_0}{3n_{eff}} \tag{5.23}$$

where $\lambda_0$ is the central wavelength in the region of interest. Using these values as a starting point for the optimization a wavelength-flattened *UMZI* coupler was found with: $W_1 = W_2 = 5.7\,\mu$m, $Sep = 9.5\,\mu$m, $L_{st,1} = 1380\,\mu$m and $L_{st,2} = 500\,\mu$m and $\Delta L = 0.352\,\mu$m. Fig. 5.7$A$ shows a $2D$ *BPM* simulation of the imbalance as a function of the wavelength for the considered *UMZI* coupler. The imbalance varies less than 0.2 $dB$ from 1500 to 1600 nm, but for slightly lower wavelengths it increases rather quickly, e.g. $IMB(\lambda = 1480\,\text{nm}) \simeq 0.4\,dB$. Overall the wavelength-flatness is similar to that of the *UA* coupler.

Fig. 5.7$B$ shows the process tolerance of the *UMZI* coupler, which is superior to that of the directional couplers. The considered process variations all lead to changes in the imbalance of less than 0.1 $dB$.

The *UMZI* coupler is between 2 and 2.5 times as long as a directional coupler, which can pose a problem for some applications. A possible solution to this problem could be to produce the *UMZI* coupler at a higher step-index as the length scales inversely proportional with the step-index (see section 2.2). By

scaling the step-index by 2.5 the *UMZI* coupler will be as short as the directional coupler (at the original step-index). From eq. 5.7 the process sensitivity at the new index is obtained by scaling $\delta WWR$ and $\delta H$ with $2.5^{0.5} \simeq 1.6$. By comparing the deviations of the *UMZI* coupler at $\delta WWR = 0.016$ and $\delta H = 0.08\,\mu$m with the deviations of the *UA* coupler at $\delta WWR = 0.010$ and $\delta H = 0.05\,\mu$m it is seen that the *UMZI* coupler designed for $\Delta n = 0.025$ is more process tolerant than the *UA* coupler designed for $\Delta n = 0.010$.

### 5.2.3 Multi mode interference couplers

Multi mode interference (*MMI)* coupler works by interference between several guided modes. The first *MMI* couplers were fabricated in 1992 ([76]) and have since been produced by numerous university groups and companies (e.g. [77], [78], [79], [80], [81], [82], [83], [84]). So far the *MMI* couplers have mainly been produced in $III/V$ materials but also silica-on-silicon devices have been demonstrated. $1xN$ couplers were demonstrated in [85] for $N = 2, 4$ and 8. A variable splitting ratio has been demonstrated using $2x2$ *MMI* couplers in a very compact *MZI* configuration [86] or by the use of an angled *MMI* coupler [87]. The initial *MMI* based devices had problems with high crosstalk levels, but recently *MMI* based optical non-blocking $4x4$ and $8x8$ optical switches with cross talk suppression of more than 30 $dB$ have been reported [84], [88]. The *MMI* coupler is not a loss less component but by symmetry it is still possible to unambiguously define the bar and cross coupling for a $2x2$ *MMI* coupler.

The working principles of the *MMI* coupler has been described previously (e.g. [89]) and are only summarized here. For simplicity the description only covers rectangular index slab couplers (see fig. 5.8), where the width of the slab is constant throughout the structure, although other shapes can also be used [90], [91].

The"ideal *MMI*" is achieved in the limit of infinite confinement:

$$V^2 = k^2 W_{MMI} H (n_o^2 - n_{cl}^2) \rightarrow \infty$$

where $W_{MMI}$ is the *MMI* width, $H$ ($\ll W_{MMI}$) the height, $n_0$ the core index and $n_{cl}$ the cladding index. Consider the modes having higher order in the $x$-direction in fig. 5.8, but zero order in the $y$-direction. In the considered limit

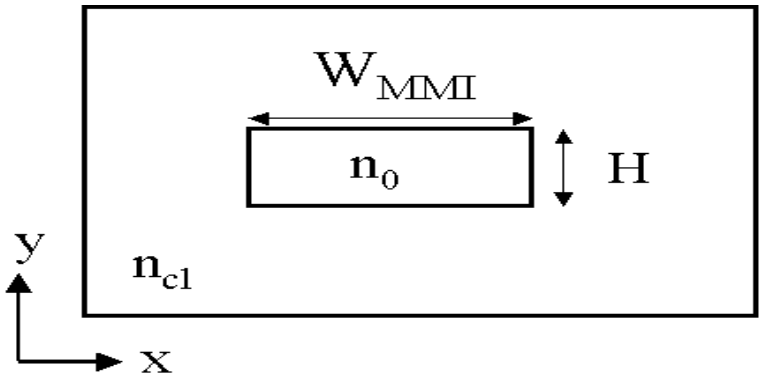


Figure 5.8: Cross section of the considered *MMI* structure, where $n_0$ and $n_{cl}$ is the index of the core and the cladding, and the core has height $H$ and width $W_{MMI}$.

the modal propagation constants are found analytically as [92]:

$$\beta_m = kn_{eff} \cdot \sqrt{1 - \frac{(m+1)^2}{W_{MMI}^2} \cdot \frac{1}{k^2 n_{eff}^2}} \tag{5.24}$$

$$\approx kn_{eff} - \frac{(m+1)^2}{2kn_{eff}W_{MMI}^2} \tag{5.25}$$

where $m$ is the number of the mode, and eq. 5.25 is obtained by a second order Taylor expansion of eq. 5.24. Define the modal phase difference at length $L$ as:

$$\Delta\phi_{0m} \equiv L(\beta_0 - \beta_m) = \frac{L}{(2W_{MMI}^2 kn_{eff})}(m^2 + 2m) \tag{5.26}$$

Notice that $(m^2 + 2m)$ is a positive integer, whereby the field will regenerate whenever $L$ becomes a multiple of:

$$L_c = 4\pi W_{MMI}^2 kn_{eff} = \frac{8\pi n_{eff} W_{MMI}^2}{\lambda} \tag{5.27}$$

where $L_c$ is denoted the characteristic length and it is worth noticing that it scales with $W_{MMI}^2$. For a propagation length given as a rational fraction of

$L_c$ the interference pattern can be described as a finite number of inversions ($\psi(x) -> \psi(-x)$) and translations ($\psi(x) -> \psi(x+\Delta)$) of the input field [89]. For $L = \frac{1}{2}L_c$ the output field becomes the inverted input field, while for $L = \frac{1}{4}L_c$ the output field becomes a superposition of $\psi(x)$ and $\psi(-x)$. This length can be used to construct a $2x2$ *MMI* coupler.

However, the regeneration will not be perfect since it relies on neglecting the higher order Taylor terms (the paraxial approximation). By including the next order Taylor term the phase difference $\Delta\phi_m$ at the characteristic length is changed by:

$$\begin{aligned} \delta_1\Delta\phi_m &= L_C k n_{eff} \left( -\frac{1}{8} \left( \frac{(m+1)^2}{W_{MMI}^2 k^2 n_{eff}^2} \right)^2 \right) \\ &= -\frac{1}{2} \frac{(m+1)^4}{W_{MMI}^2 k^2 n_{eff}^2} \cdot \pi \end{aligned} \tag{5.28}$$

where $\delta_1\Delta\phi_m$ is denoted the "phase error due to the Taylor expansion".

Consider a realistic *MMI* coupler with a finite normalized frequency. Here the mode fields are not strictly confined to the core but will penetrate into the cladding with increasing width as the mode number increases. This will change the propagation constants to higher values than for the ideal case. To keep the dispersion relation in a form similar to eq. 5.24 the monotonic increasing effective mode width function $W_e(m)$ is introduced:

$$\beta_m = k \cdot n_{eff} \cdot \sqrt{1 - (\frac{m+1}{W_e(m)})^2 \cdot \frac{1}{k^2 n_{eff}^2}} \tag{5.29}$$

where the effective index $n_{eff}$ must be found numerically. Using the effective mode width function the modified dispersion relation contributes to another phase error type found as:

$$\begin{aligned} \delta_2\Delta\phi_m &= L_c k n_{eff} (-\frac{1}{2} \frac{(m+1)^2}{k^2 n_{eff}^2 W_e(0)^2} + \frac{1}{2} \frac{(m+1)^2}{k^2 n_{eff}^2 W_e(m)^2}) \\ &\approx 4(m+1)^2 \frac{W_e(m) - W_e(0)}{W_e(m)} \cdot \pi \end{aligned} \tag{5.30}$$

and denoted "phase error due to mode width variation". A comparison of eq. 5.28 and eq. 5.30 shows that the errors have opposite sign and a different scaling

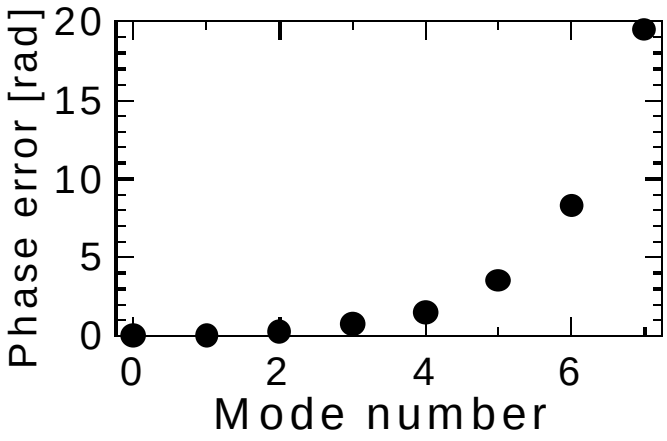


Figure 5.9: The modal phase errors of the guided modes of a *MMI* slab with $W_{MMI} = 40\,\mu$m and the characteristic length $L_c = 14.3\,$mm for $\lambda = 1550\,$nm.

behavior. Therefore it is possible to adjust the width of the *MMI* to minimize the sum of the two error terms at arbitrary positions of the excitation spectrum [92]. However, for the chosen index step this would require a structure that is several hundred microns wide, which is not feasible for a $2x2$ *MMI* coupler as it would increase the length enormously (see eq. 5.27). For feasible widths the "phase error due to mode width variation" dominates. Fig. 5.9 shows the phase errors of a multi mode slab with $W_{MMI} = 40\,\mu$m at the characteristic length $L_c = 14.3\,$mm as a function of the mode number for the slabs guided modes at a wavelength of $\lambda = 1550\,$nm. The figure shows that the phase error is very small for the lowest order modes, but increasing monotonically with the mode number. Thus a *MMI* coupler should be designed so the power in the lower order modes is maximized.

Recall that the equation for the characteristic length is eq. 5.27 is valid in the limit of infinite confinement. To estimate the characteristic length of a real *MMI* the *MMI* width should be replaced by an effective mode width, e.g. the width of the zero order mode:

$$L_c = \frac{8\pi n_{Sl} W_e^2(0)}{\lambda} \tag{5.31}$$

where $n_{Sl}$ is the effective index of a slab with an index of $n_{core}$ and a width equal to the height of the core, which is sandwiched between two layers with the index of the buffer $n_{buf}$. Within the effective index approximation the effective width of the zero order mode is [89]:

$$\begin{aligned} W_e(0) &= W_{MMI} + \frac{\lambda}{\pi}\left(\frac{n_{buf}}{n_{Sl}}\right)^{2\sigma}(n_{Sl}^2 - n_{buf}^2)^{-\frac{1}{2}} \\ \sigma &= \left\{ \begin{array}{ll} 0 & TE \\ 1 & TM \end{array} \right\} \end{aligned} \tag{5.32}$$

For the considered structure with index step $\Delta n = 10^{-2}$, height $H = 5.50\,\mu$m, $n_{buf} = 1.445$ at $\lambda = 1.55\,\mu$m the slab index is $n_{Sl} = 1.4543$. Thus the width correction at $\lambda = 1550\,$nm is $3.00\,\mu$m for $TE$ and $2.96\,\mu$m for $TM$ polarization. Using eq. 5.27 and eq. 5.32 the effects of changing the step-index can be examined. For simplicity the following calculation is for the same height and wavelength as above and only for $TE$ polarized light:

$$\Delta n = 0.009 \Rightarrow n_{Sl} = 1.4533 \Rightarrow W_e(0) - W_{MMI} = 3.18\,\mu\text{m} \tag{5.33}$$

For an $MMI$ coupler with $W_{MMI} = 40\,\mu$m this implies:

$$\frac{L_c(\Delta n = 0.009)}{L_c(\Delta n = 0.010)} = (\frac{43.18}{43.00})^2 \frac{1.4533}{1.4543} = 1.0075 \tag{5.34}$$

Eq. 5.34 shows that a change of step-index from $\Delta n = 0.010$ to $0.009$ (10%) only induces a decrease of 0.75% of the characteristic length of a $MMI$ coupler with $W_{MMI} = 40\,\mu$m and $H = 5.50\,\mu$m. This shows that a $MMI$ coupler is very insensitive towards variations in the step-index.

Due to the phase errors the $MMI$ coupler is not a loss less component, although the minimum theoretical loss can be very low (less than 0.1 $dB$). Furthermore the loss varies with the length achieving a local minimum at rational fractions of $L_c$. Neglecting the loss the transfer matrix for a 3 $dB$ $MMI$ coupler ($L = L_c/4$) is [93], [82]:

$$\underline{T}_{MMI} = \frac{1}{\sqrt{2}}\left[ \begin{array}{cc} 1 & -i \\ -i & 1 \end{array} \right] \tag{5.35}$$

where the output from arm 3 and 4 are $\pi$ radians out of phase. Eq. 5.35 has the same form as the transfer matrix of a 3 $dB$ $US$ coupler (see eq. 5.14). However, the similarity between the $MMI$ and the $US$ coupler is only present at the 3 $dB$

point. If the length of the *US* coupler is changed the coupling changes but the loss will remain zero, whereas a change in the *MMI* length can be regarded as a defocussing leading to an increase of the loss for both output arms, which implies that the imbalance will remain low. With respect to the imbalance the *MMI* coupler is thus expected to have better wavelength-flatness than the *US* coupler.

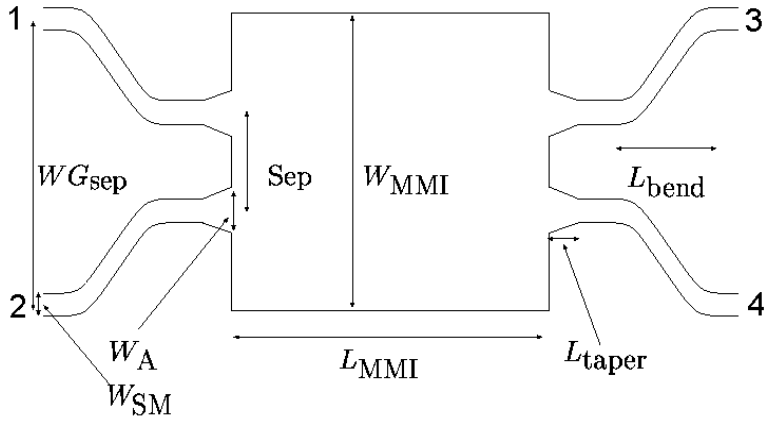


Figure 5.10: The $2x2$ *MMI* coupler design used in the investigation. The access waveguides have width $W_A$ and a separation between them of $Sep$. The *MMI* slab has length $L_{MMI}$ and width $W_{MMI}$.

Since the aim of this investigation is to find a process tolerant optical coupler the simple rectangular *MMI* structure is used. Fig. 5.10 shows the *MMI* design used in the investigation, where $L_{MMI}$ and $W_{MMI}$ is the length and width of the multi mode slab, $Sep$ is the center to center separation between the access waveguides, $W_A$ is the width of the access waveguide. $W_{SM}$ is the width of the initial single mode waveguide. After the bends the waveguides are adiabatically tapered from $W_{SM}$ to $W_A$, ensuring that it is the zero order mode of the access waveguide that excites the *MMI* structure.

Fig. $5.11A$ shows the simulated wavelength response of a *MMI* coupler with $L_{MMI} = 3540\,\mu$m, $W_{MMI} = 40.0\,\mu$m, $Sep = 26.8\,\mu$m, $W_A = 13.8\,\mu$m, $W_{SM} = 6.0\,\mu$m. The imbalance varies less than 0.2 $dB$ from 1480 nm to 1620 nm, whereby the wavelength performance is slightly better than that of the *UA* and

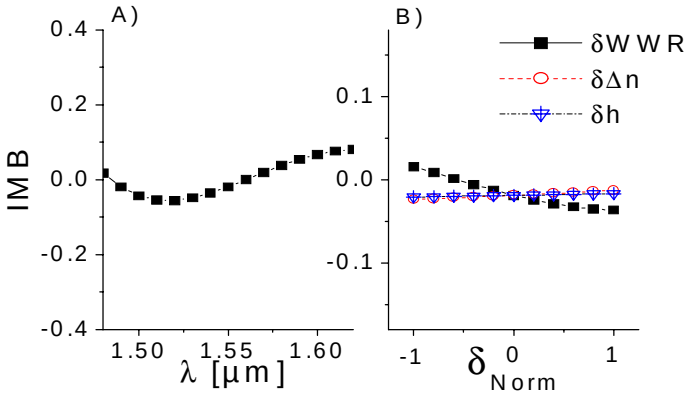


Figure 5.11: The simulated imbalance (in $dB$) of a *MMI* coupler as a function of $A$) the wavelength and $B$) the normalized process deviation $\delta_{Norm}$.

the *UMZI* coupler. Fig. 5.11$B$ shows that changes in the step-index and height have negligible effect on the imbalance, and that changes in the $WWR$ incur a change of less than 0.1 $dB$ in the imbalance of the *MMI* coupler. Thus the *MMI* coupler has even better tolerance towards the considered process parameters than the *UMZI* coupler.

The considered design is conservative in the sense that the *MMI* width and length are rather large, i.e. is longer than the *UA* coupler but shorter than the *UMZI* coupler. Decreasing the *MMI* width decreases the length of the *MMI* (see eq. 5.27). It also decreases the number of supported modes and increases the phase errors, see eq. 5.28 and 5.30, which limits the minimum possible width. Another limitation comes from the need to have a minimum distance between the centers of the access waveguides to prevent coupling between them. Simulations indicate that with the chosen index step $\Delta n = 0.010$ the minimum *MMI* width is approximately $\min(W_{MMI}) \simeq 20\,\mu$m. From eq. 5.27 this gives $\min(L_{MMI}) \simeq 0.9\,$mm, which is similar to the length of the coupling region in a directional coupler. This minimum size rectangular *MMI* has a simulated excess loss of 0.4 $dB$ and an imbalance of 0 $dB$, but the imbalance changes by 0.7 $dB$ from 1500 to 1600 nm, which is not quite as good as for the reference design. Another approach to reduce the length is to choose a parabolic *MMI*

design leading to a length reduction by a factor of three [90], but the trade-off is a decrease in the process tolerance[4]. Finally the access waveguides can be placed so that mode number $2, 5, 8..$ are not excited, which leads to a reduction of the *MMI* length by a factor of three [89]. Accordingly the *MMI* coupler is not necessarily longer than the directional coupler, and for waveguides with a larger step-index it might actually be shorter than directional couplers [94].

In conclusion the *MMI* coupler has better numerical specifications than any of the other considered types of couplers.

## 5.3 Experimental results

The simulations in section 5.2 were obtained using the $2D$ *BPM*, which in general is inaccurate (see appendix A). Thus the designs were fine tuned before mask layout using the $3D$ *BPM*. For the *US* and *UMZI* couplers this amounts to increasing the length of the coupling region by approximately 15%, whereas for the *UA* coupler the length of the coupling region is increased while the asymmetry is decreased[5]. For the *MMI* couplers the resemblance between the $2D$ and $3D$ *BPM* predictions is larger than for the directional coupler, e.g. the simulated optimum length changes by less than 2% and therefore only minor modifications of the $2D$ *BPM* design are needed.

The characterization results are obtained with a polarized laser at $\lambda = 1557\,\text{nm}$ and the polarization sensitivity is examined by scanning the polarization of the light. The wavelength dependency is found with a polarized *ASE* source and an optical spectrum analyzer (*OSA*) using a resolution of $res = 0.1\,\text{nm}$ (see section 3.2). It should be emphasized that all the widths are given in terms of the mask width ($W_M$). Because of the waveguide width reduction ($WWR$) they are larger than the actual widths on the wafer:

$$W_M = W + WWR \approx W + 1.8\,\mu\text{m} \tag{5.36}$$

where $W$ is the width on the wafer and the estimate of the $WWR$ is based upon pictures of the waveguides (see section 3.2).

[4] However, the authors ([90]) claim that for a fixed *MMI* length the process tolerance with respect to changes in the width is increased by using a parabolic design.

[5] Fixing the width of the wide core at $W_1 = 5.7\ \mu m$ and the edge-to-edge separation between the cores at $G_{E2E} = 3.8\ \mu m$ the width of the narrow core ($W_2$) had to be increased from $4.95\ \mu m$ to $5.15\ \mu m$. Using the new asymmetry the simulated cross coupling amplitude $(C/\kappa)^2$ is $0.73$ for the $2D$ *BPM* and $0.62$ for $3D$ *BPM*, corresponding to a difference of $15\%$ (see appendix A)

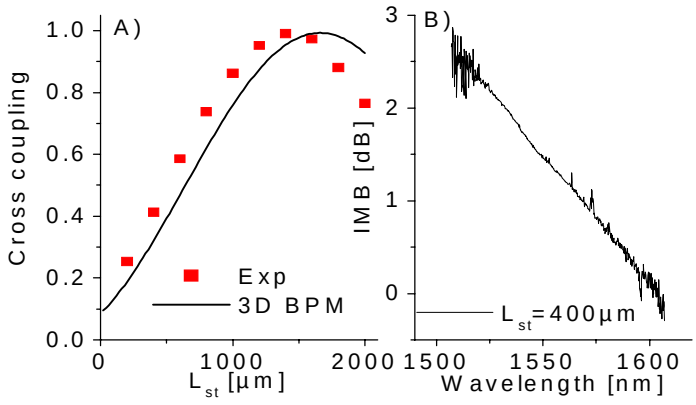


Figure 5.12: The measured and simulated cross coupling $P_c$ of *US* couplers as a function of *A*) the length of the coupling region $L_{st}$ and *B*) the wavelength.

### 5.3.1 Directional couplers

The results for the directional couplers are split into two parts, one for the *US* and another for the *UA* couplers.

#### *US* couplers

A set of *US* couplers that only differ by the length of the coupling region $L_{st}$ was fabricated. The measured cross coupling should follow a sine square curve (see eq. 5.15) whence it is possible to extract the coupling length by a fit.

Fig. 5.12*A* shows the measured and simulated (by $3D\ BPM$) cross coupling for a set of *US* couplers with $W_{M1} = W_{M2} = 7.50\,\mu$m, $Sep = 9.50\,\mu$m and different length of the coupling region $L_{st}$. Both curves follow the expected sine square behavior (see eq. 5.15), but the measurements have larger coupling strength than the simulations. A fit to the measurements gives a coupling coefficient that is 10% larger than from the simulations (hereby the coupling length becomes 10% smaller than from the calculation). Close to the 3 $dB$ point this gives a large deviation in the cross coupling of approximately $\delta P_c \simeq 0.10$, which by eq. 5.3 corresponds to a change in imbalance of $\delta IMB = 1.8\ dB$. A

comparison with the results from section 5.2.1 shows that the maximal simulated change of imbalance due to process parameter variation was $\delta IMB \simeq 0.4\ dB$. Fig. 5.12*B* shows the measured imbalance as a function of the wavelength for the *US* coupler with $L_{st} = 400\,\mu$m. The figure shows that the imbalance decreases linearly with the wavelength having a total change of $\delta IMB = 2.8\ dB$ over 100 nm, which is in accordance with the simulations. For the *US* coupler that is insensitive towards changes in the *WWR* a similar measurements gave a coupling length that was 18% smaller than simulated with the 3*D BPM* and a wavelength response that varied more than 3 *dB* over 100 nm.

As shown above the deviation between the measurements and simulations for the US couplers can not be explained from a variation of the process parameters within the given ranges. A numerical investigation shows that it is not possible (by extending the range of the process parameter deviation) to find a set of values for the process parameters that describes all the couplers. Thus the measurements can not be explained with the step-index waveguide model. Furthermore the measurements confirm that the *US* coupler does not have wavelength-flattened coupling.

### *UA* couplers

As the *UA* coupler is very sensitive towards changes in the asymmetry several sets of couplers with different asymmetry were fabricated. All the couplers have $W_{M1} = 7.5\,\mu$m and $G_{E2E} = 2.0\,\mu$m and for each set $W_{M2}$ is fixed at either 6.80, 6.90 or 7.00 $\mu$m, whereas the length of the coupling region $L_{st}$ is varied. The measurements are shown as symbols in fig. 5.13, whereas the 3*D BPM* simulations are shown as lines.

The figure shows that for $W_{M2} = 6.80\,\mu$m the measurements and simulations deviate by up to 10% of the input power, whereas the deviations are smaller for the other considered asymmetries. To make a further comparison both the measured and the simulated results are fitted to eq. 5.19. It is found that the measured cross coupling amplitude in general is between 10 and 15% larger than the simulated cross coupling amplitude. The fits to the coupling length are quite uncertain as there only is five measurement points in each set and the coupling length is correlated with the equivalent bend length $\delta L_b$. To estimate the coupling length it was assumed that the measured value of the equivalent bend length is equal to the simulated value. Using this assumption the measured coupling length is between 5 and 10% smaller than the simulated coupling length, which is in good agreement with the results for the *US* coupler. The fits indicate show that the close resemblance between the measurements and

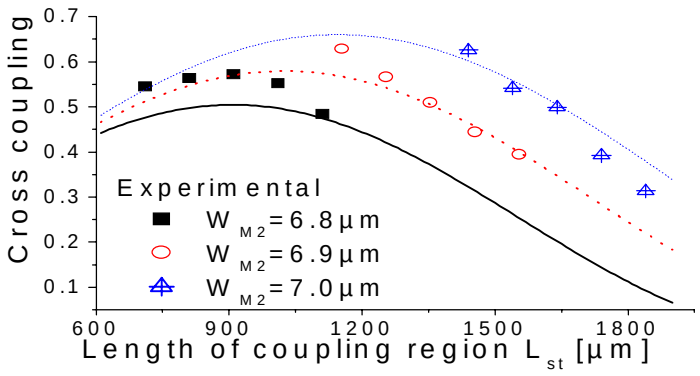


Figure 5.13: The measured (symbols) and $3D$ *BPM* simulated (lines) cross coupling for three sets of *UA* couplers as a function of the length of the couplin region $L_{st}$. The couplers all have $W_{M1} = 7.5\,\mu$m, but the width of the narrow core is different from set to set (from 6.8 to 7.0 $\mu$m).

simulations for $W_{M2} = 6.9\,\mu$m and $W_{M2} = 7.0\,\mu$m is coincidental.

The measured wavelength response is also slightly different than the simulated response. However, as several couplers were fabricated it is anyhow possible to find a wavelength-flattened coupler among them. The coupler parameters are: $W_{M1} = 7.5\,\mu$m, $W_{M2} = 6.8\,\mu$m and $L_{st} = 1.12\,$mm, and its measured imbalance as a function of wavelength is seen as a dotted line on fig. 5.14. The curve has large fluctuations close to the edges of the wavelength range due to the low power levels of the source (see section 3.5). By using a 5 point adjacent averaging. the full line is obtained, which has a deviation in the imbalance of less than 0.15 *dB* over the entire wavelength interval. This is as good as the simulated wavelength flatness. By comparing fig. 5.13 with fig. 5.4 it is seen that in both cases wavelength-flattened coupling is obtained at the second cross point as a function of the length of the coupling region for a structure having a cross coupling amplitude of approximately 0.60, whence the measurements have the same functional form as the simulations.

The simulations presented in section 5.2 showed that the *UA* coupler is very sensitive towards changes in the *WWR*. The process sensitivity of *UA* couplers was examined by measuring the same sets of couplers on several nominally

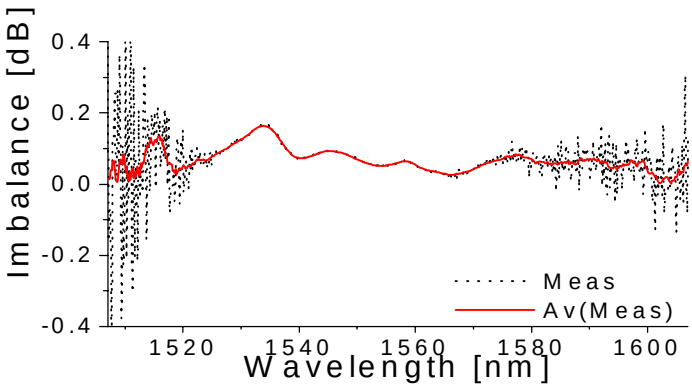


Figure 5.14: Wavelength response of a wavelength-flattened *UA* coupler measured on an *OSA* with a resolution of $res = 0.1\,\mathrm{nm}$. The dotted line is the raw data, whereas the full line is obtained by a 5 point adjacent averaging.

identical wafers. Fig. 5.15 shows the measured cross coupling for the set with $W_{M1} = 7.5\,\mu\mathrm{m}$ and $W_{M2} = 6.8\,\mu\mathrm{m}$ on two nominally identical wafers (#1 and #2). In general the cross coupling is larger on wafer #1 than on wafer #2 and the difference is approximately 2% of the input power. A measurement shows that the local value of the $WWR$ is approximately $0.2\,\mu\mathrm{m}$ higher on wafer #1 than on wafer #2. From fig. 5.5 it is seen that an increase of $\delta WWR = 0.2\,\mu\mathrm{m}$ induces a change of imbalance of 0.8 $dB$, which by eq. 5.3 amounts to a change of the cross coupling of $-4.4\%$ of the input power. Consequently the measured difference in $WWR$ can quantitatively explain the measured difference in cross coupling. Similar curves for the other asymmetries show the same behavior with an even larger deviation between 0.03 and 0.05.

In conclusion it is possible to fabricate wavelength-flattened *UA* couplers with an imbalance of less than 0.2 $dB$ over 100nm, but the measurements confirm that the architecture is very process sensitive whence these couplers require very strict fabrication control to have a reasonable yield.

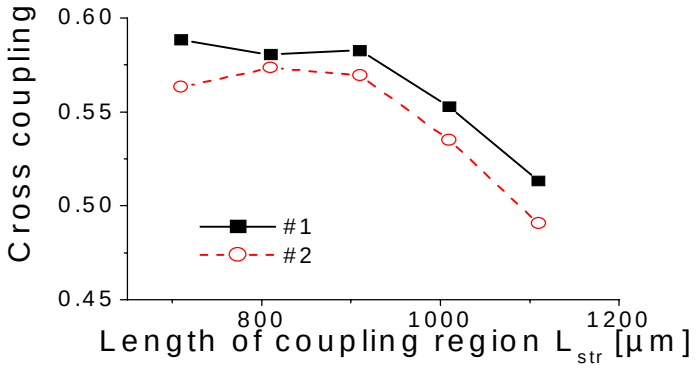


Figure 5.15: The measured cross coupling $P_c$ as a function of the length of the coupling region $L_{st}$ for a set of *UA* couplers, which was fabricated on two nominally identical wafers.

### Polarization dependency

The polarization dependency was estimated by scanning the polarization of the light that is sent through the waveguides. The measured power transfer fluctuates due to polarization dependent loss ($PDL$) and polarization dependent coupling ($PDC$). Recall from section 4.1 that the $PDL$ of a straight waveguide is below 0.1 $dB$. As the couplers are generically loss less the remaining fluctuation in the power transfer are ascribed to $PDC$. The measured variation in $dB$ increases as the power transfer decreases, which can be ascribed to that the $dB$ scale is logarithmic. For power transfers less than $-10$ $dB$ the fluctuations is more than $\delta P > 0.5\,dB$, whereas for power transfers close to unity it approaches the $PDL$ for a straight waveguide ($\delta P \approx 0.1$ $dB$).

For 3 $dB$ couplers the measured fluctuations are typically $\delta P \approx 0.3 - 0.4\,dB$ for *US* couplers and $\delta P \approx 0.2$ $dB$ for *UA* couplers. Notice that the fluctuation is larger for the *US* than for the *UA* coupler. This is probably caused by that 3 $dB$ point being the position where the *US* coupler is most sensitive towards changes in the coupling strength, which is not the case for the *UA* couplers.

The measured birefringence of single-mode standard waveguides is on the order of $\Delta n_{eff} \approx 10^{-5}$ (see section 4.3) and accordingly it can not explain

the measured *PDL*. However, in general the measured birefringence is different than the geometrical birefringence, which probably is due to stress induced birefringence (see section 4.3). It would therefore be interesting to measure the birefringence of the two supermodes in the coupling region, but this has not been done.

### 5.3.2 *UMZI* couplers

Due to processing problems all the fabricated *UMZI* couplers had air-bubbles between the waveguides in the coupling region (see section 3.3) and therefore did not work at all. However, *UMZI* couplers have been fabricated by others, and their results show the desired wavelength-flattened and process tolerant response [22], [75].

### 5.3.3 *MMI* couplers

A reference *MMI* design was found from numerous simulations. It has parameter values: $L_{MMI} = 3540\,\mu$m, $W_{MMI} = 40.0\,\mu$m, $Sep = 26.8\,\mu$m, $W_A = 13.8\,\mu$m, $W_{SM} = 6.0\,\mu$m (compare with fig. 5.10). To find the importance of the different design parameters, they were varied from their reference value one at a time.

The presented measurements are obtained with *TM* polarized light at a wavelength of $\lambda = 1550\,$nm, which is ensured by measuring the reflection spectrum from a reference waveguide with an inscribed weak Bragg grating, where the polarization is changed until only the resonance peak from the *TM* polarization is observed, see section 3.5.

#### Width of the access waveguides

The modal excitation spectrum depends on the input field and thereby on the width of the access waveguides ($W_A$). A simulation shows that for the considered reference design the power in the lower order modes increase with the size of the access waveguide width, which by comparison with fig. 5.9 shows that the average phase error decreases with the access width. Accordingly the excess loss is expected to decrease with the access waveguide width. Furthermore it has been reported that the fabrication tolerances increase with the access waveguide width [95], [89].

The access waveguide width is varied from $7.8\,\mu$m to $15.8\,\mu$m. Fig. 5.16 shows the simulated and measured *MMI* excess loss as a function of the access waveguide width. As expected the simulated excess loss initially decreases with

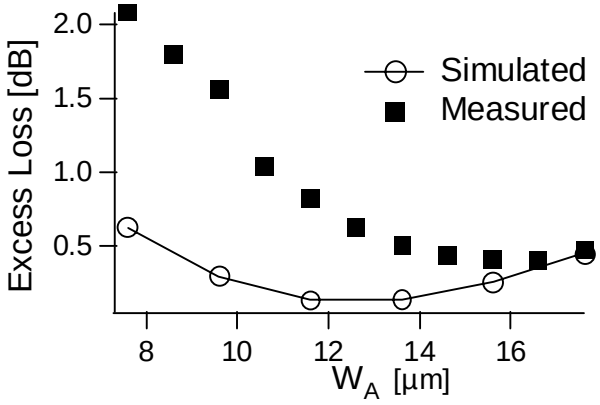


Figure 5.16: The excess loss of the *MMI* coupler as a function of the access waveguide width $W_A$.

$W_A$, but then it reaches a minimum from which it again increases. This happens because the access waveguides start to exceed the width of the *MMI* structure (at $W_A = 13.2\,\mu$m). Another effect is that the optimum length changes with the mode spectrum due to phase errors. Since the *MMI* length is fixed in this series it will not remain the optimum length for all values of $W_A$. The measured curve on fig. 5.16 shows the same qualitative behavior as the simulated curve, except for that the increase of the excess loss starts at a larger value of $W_A$. The measured excess loss is also larger than the simulated excess loss. For the optimum design the simulated excess loss is 0.07 $dB$, whereas the measured loss is approximately 0.4 $dB$.

The results show that it is advantageous to use wide access waveguides, but these should not exceed the *MMI* slab.

**Separation between the access waveguides**

The modal excitation spectrum also depends on the separation between the access waveguides. This spacing should be sufficient to prevent coupling in the access waveguides as this decreases the components process tolerance and wavelength flatness. Simulations show that for the considered step-index a separation larger than $15\,\mu$m is required. Accordingly the separation was varied

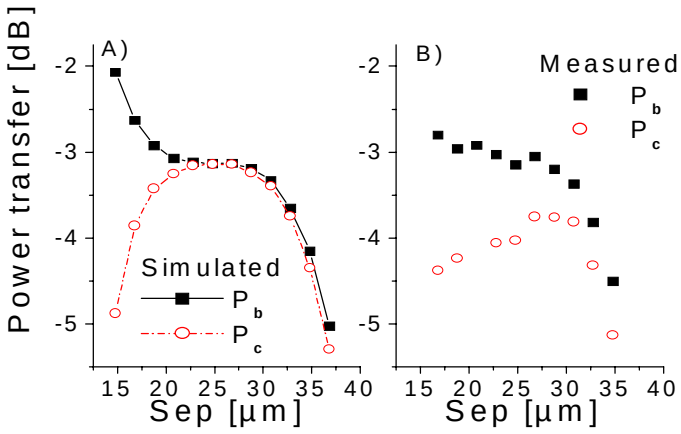


Figure 5.17: The *A*) simulated and *B*) measured bar $P_b$ and cross coupling $P_c$ of the *MMI* coupler as a function of the separation between the access waveguides *Sep*.

from 15 $\mu$m to 35 $\mu$m for the reference design.

Fig. 5.17 shows the simulated and measured power transfer. The simulated results show that for separations smaller than approximately 23 $\mu$m (57% of the *MMI* width) the bar coupling $P_b$ is larger than the cross coupling $P_c$. For separations between 23 $\mu$m and 28 $\mu$m the bar and cross couplings are nearly identical and furthermore the absolute value is nearly constant, while for separations larger than 28 $\mu$m the total power transfer decreases, because a substantial fraction of the access waveguide exceeds the *MMI* width. The measured power transfer shows the same behavior as the simulated curve except that the cross coupling is slightly less than the bar power.

It can be concluded that the separation can be chosen within a quite wide range. For the reference design a separation between 23 $\mu$m and 28 $\mu$m can be used, which corresponds to between 57 and 70% of the *MMI* width.

### Length sensitivity of the *MMI*

If the *MMI* length $L_{MMI}$ is slightly different from the optimal length this can be regarded as a defocussing effect as the power in both arms decreases, whence

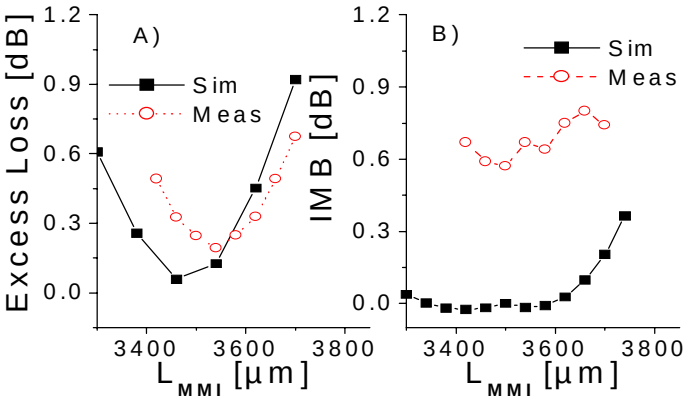


Figure 5.18: The measured and simulated $A$) excess loss and $B$) imbalance as a function of the $MMI$ length $L_{MMI}$ for a variation of $\pm 5\%$ from the optimum length.

the excess loss increases while the imbalance remains low, see section 5.2.3.

In this investigation the $MMI$ length $L_{MMI}$ is varied with $\pm 5\%$ from the simulated optimum length. Fig. 5.18$A$ shows the simulated and measured excess loss, while fig. 5.18$B$ shows the imbalance as a function of the $MMI$ length. The simulated excess loss varies from 0.07 $dB$ to 0.6 $dB$, whereas the measured excess loss varies from 0.4 $dB$ to 0.7 $dB$. Furthermore the measured excess loss has its minimum at a larger length than the simulations. The difference in length is $\delta L_{MMI} \approx 80\,\mu$m, which is equivalent to 2% of the $MMI$ length. By eq. 5.27 this could be explained by a deviation of 1% in the $MMI$ width. Fig. 5.18$B$ shows that the simulated imbalance is close to zero in the entire range whereas the measured imbalance is close to 0.6 $dB$. The variation in both the measured and simulated imbalance is less than 0.2 $dB$ over the entire range.

Consequently the $MMI$ couplers have excellent tolerance towards the $MMI$ length, but the measured imbalance of 0.6 $dB$ is unexpected. A closer inspection of the measured data for the previously presented $MMI$ couplers shows that the unexpected imbalance is also present when the separation between the access waveguides (see of fig. 5.17) or the access waveguide width is varied. Furthermore this effect is seen on several wafers and can not be dismissed as a singular

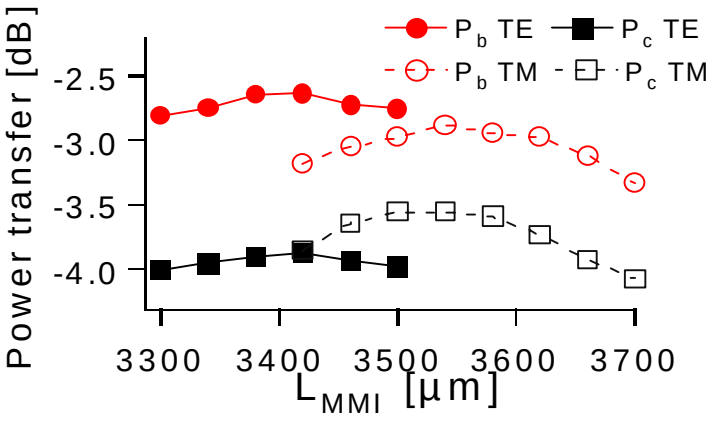


Figure 5.19: The measured bar ($P_b$) and cross ($P_c$) coupling for the *MMI* couplers as a function of the *MMI* length $L_{MMI}$ for both the *TE* and *TM* polarization.

effect.

### Polarization dependency

To examine the polarization sensitivity the power transfer was measured using both the *TE* and the *TM* polarization, see fig. 5.19. The figure shows a large difference between the two polarizations. For the *TE* polarization the excess loss has a minimum at $L_{MMI} \approx 3.42\,\mathrm{mm}$ whereas for the *TM* polarization the minimum is at $L_{MMI} \approx 3.54\,\mathrm{mm}$. The polarization induced change in power transfer changes with the *MMI* length, reaching values of more than 1.0 $dB$. Notice that the optimum length is larger for the *TM* polarization than for the *TE* polarization, which is in accordance with the simulations presented in section 5.2.3, since $n_{eff}(TM) < n_{eff}(TE)$. In section 4.3 it was shown that a straight waveguide with a width of $40\,\mu\mathrm{m}$ has a substantial birefringence of $\Delta n_{eff} = 4.7 \cdot 10^{-4}$. However, a simulation which utilizes the measured birefringence predicts a change in length, which is an order of magnitude smaller than the measured change. Furthermore the imbalance is approximately $IMB \approx 1.2\ dB$ for the *TE* polarized light, whereas it was only 0.6 $dB$ for the *TM* polarized light, which is also unexplained.

In conclusion the measurements show that the *MMI* couplers have a large polarization dependency, which is not present in the simulations. The polarization dependency can not be explained by assuming that the waveguide has a step-index profile, where the step-index for each polarization is chosen to match the measured effective index. Furthermore the imbalance is twice as large for the *TE* as for the *TM* polarization. It must be concluded that the waveguides can not be accurately described by a step-index model.

**Wavelength response**

Changing the signal wavelength corresponds to scaling the *MMI* structure. Eq. 5.27 shows that the characteristic length is inversely proportional to the wavelength, but to first order this is expected to be the only effect of changing the wavelength. It was previously shown that the *MMI* coupler is insensitive towards changes of the *MMI* length, and accordingly the same behavior is expected as a function of the wavelength.

The wavelength response is measured for different *MMI* lengths around the reference design. It is found that the wavelength having minimum imbalance increases approximately 15 nm ($\approx 1\%$) when the *MMI* length increases by 40 $\mu$m ($\approx 1\%$). The measured and simulated spectra for a *MMI* with length $L_{MMI} = 3580\,\mu$m are shown in fig. 5.20. The simulated imbalance is less than 0.1 $dB$ from 1500 to 1600 nm, which is a very wide band response. The measured imbalance is positive with a minimum value of 0.5 $dB$ at a wavelength of $\lambda = 1540$ nm and changes 0.5 $dB$ over 75 nm, which is a wide band response but not as good as simulated. As the *MMI* couplers were measured to be very sensitive to the polarization the deviation from the simulated result can be caused by the polarization varying with the wavelength.

## 5.4 Discussion of the measurements

The general agreement between the measurements and the simulations is good. The measurements have the same function form as the simulations, which shows the viability of the model. However, there are some differences between the simulations and the measurements. For the directional couplers the measured coupling length was in general shorter than the simulated coupling length. As a curiosity it can be mentioned that the predictions from the $2D$ *BPM* is closer to the measured results than the results from the $3D$ *BPM*, but this must be caused by coincidence since the $2D$ *BPM* is inaccurate. It was shown that the

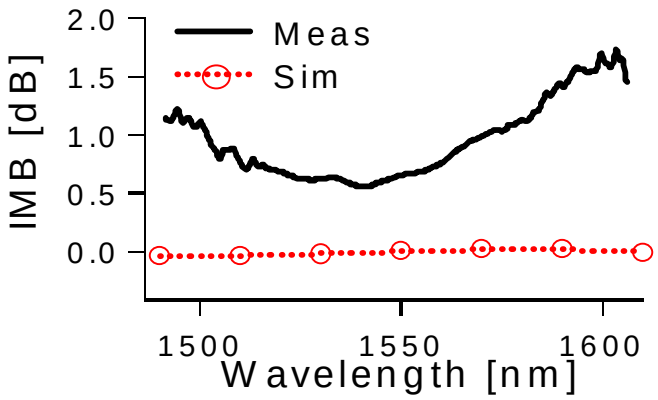


Figure 5.20: The measured and simulated wavelength response of the $2x2$ *MMI* coupler with length $L_{MMI} = 3.58\ mm$.

discrepancy between the measurements and simulations can not be explained by process variations of the waveguide height and step-index or the waveguide width reduction ($WWR$). For the *MMI* couplers the investigation revealed two problems: an unexpected large polarization dependency and an unexpected imbalance. The considered process variations leads to changes in the optimum *MMI* length, but can not explain neither the polarization dependency or the imbalance.

The measurements show that there is something wrong in our description of the waveguides, and it must be concluded that our waveguides can not be accurately described by a step-index model. There are several possible explanations. As described in section 3.2 the sample is annealed at high temperature between the depositions steps to stabilize the glass. During the anneal of the topcladding it is possible that there is diffusion of germanium out of and boron into the core, which would lead to a graded index profile. Another possibility is that the etching process gives non rectangular waveguides, although scanning electron microscopy ($SEM$) pictures of the waveguides after the etch indicate that this is not a major problem. Finally stress induced index variations will, besides giving rise to birefringence, also introduce a weak spatial variation of the refractive index across the components on the wafer. Recall that in section 4.3 it was shown that the birefringence of our straight waveguide is small for

standard waveguides, but increases rapidly with the waveguide with and for large widths it is more than an order of magnitude larger than the geometrical birefringence, which indicates a significant stress induced birefringence. Accordingly it is plausible that our waveguides in general suffer from stress induced problems.

### 5.4.1 Effects of a graded index distribution

It has been chosen to study the effect of a graded index distribution on *MMI* couplers. By symmetry it must be expected that the error in the index distribution are symmetrical across the *MMI* slab. The simplest possible error is a parabolic perturbation of the index of the core across the *MMI*:

$$n(x) = n_{clad} + \Delta n \left( 1 + \epsilon \cdot \left( \frac{x - x_0}{W_{MMI}/2} \right)^2 \right) \tag{5.37}$$

where $x$ is the transverse coordinate, $x_0$ is the center position of the *MMI* core and $\epsilon$ the perturbation strength of the parabolic perturbation. Using this graded index distribution the power transfer of the reference *MMI* coupler was simulated using $2D$ *BPM*. The length was varied between $L_{MMI} \in \{3.4; 3.7\}$ mm (i.e. within $\pm 5\%$ of the optimum *MMI* length) for $\varepsilon = 0.00$ and $\varepsilon = \pm 0.01$. The results from these simulations are shown in fig. 5.21. All three curves have the same shape. For $\varepsilon = 0$ the imbalance is centered around zero and is in all cases less than 0.2 $dB$ (as shown in section 5.2.3). For $\varepsilon = 0.01$ the imbalance is changed by $-1$ $dB$ while it for $\varepsilon = -0.01$ is changed by $+1$ $dB$. From these results the imbalance is estimated to be

$$IMB \approx -10^{-2}\varepsilon \tag{5.38}$$

whereby an error of $\varepsilon = -0.006$ could explain the measured imbalance of 0.6 $dB$. This error corresponds to a change of the index of $\varepsilon \cdot \Delta n \simeq -6 \cdot 10^{-5}$ at the edge of the *MMI* slab (i.e. a decrease of 0.6% of the step-index).

### 5.4.2 *UV*-trimming the *MMI* couplers

According to the presented theory, it is possible to decrease the observed imbalance by increasing the refractive index at the sides of the *MMI*. As germanium-doped silica is photosensitive this can be achieved by a *UV*-exposure with a

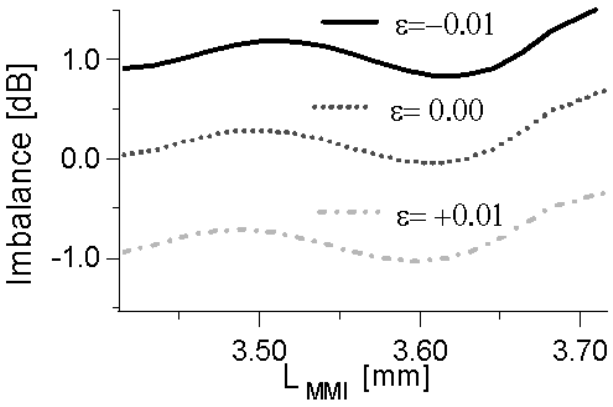


Figure 5.21: The effect of the parabolic index error $\varepsilon$ on the imbalance of the *MMI* coupler as a function of the *MMI* length $L_{MMI}$. An error $\varepsilon = \pm 0.01$ corresponds to a profile where the index at the edge of the core is increased/decreased by 1% of the step index.

focused beam with high intensity, whence the theoretical prediction is examined by trimming the *MMI* couplers with *UV*-light. Traditional single mode fibres are glued to arm 1 and 4 of the *MMI* with the lowest excess loss ($0.2\ dB$), and the pigtailed *MMI* is connected to a $1.557\,\mu$m laser, enabling a measurement of the cross coupling. The light at the wafer has the *TM* polarization. The signal is split before the *MMI* enabling for compensation of fluctuations in the laser power (see section 3.5). A test measurement showed that on a time scale of 30 mn the compensated cross coupling fluctuated less than $\pm 0.03\ dB$.

The *MMI* coupler is trimmed by scanning a *UV* beam along its sides, where the center of the *UV* beam is aligned to the edge of the *MMI*. The *UV* beam has a power of 28 mW and a $1/e^2$ diameter of $9.5\,\mu$m at the sample (25% of the *MMI* width). The fluence per scan is determined by the scan speed. After trimming both sides of the *MMI* the cross coupling is measured, whereupon another scan can be performed. The *UV*-trimming experiment took 25 mn and the measurement uncertainty is set to $\pm 0.03\ dB$. Fig. 5.22 shows the change in the compensated cross coupling $P_c$ as a function of the accumulated fluence at the edge of the *MMI* slab. By definition the change in cross coupling is zero before the first scan. The first scan increases the cross coupling by 0.13 $dB$,

while the subsequent scans each give a very small increase in the cross coupling.

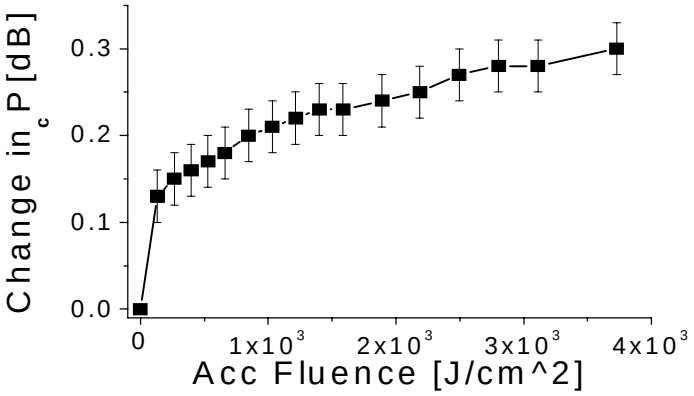


Figure 5.22: The change in cross power $P_c$ as a function of the accumulated fluence at the edge of the *MMI* coupler during the *UV*-trim. Before the trimming starts the change in cross power by definition is zero.

However, the figure clearly shows that the cross coupling increase with the accumulated fluence. At the end of the experiment the overall change is 0.3 $dB$. Furthermore there is no sign of that the limit for the trim induced change in the cross coupling is obtained.

The obtained results are in agreement with the presented theory. They show that it is possible to remove an unwanted imbalance by *UV*-trimming the *MMI*. This means that the performance of the *MMI* depends critically on the refractive index distribution thus reducing the fabrication tolerances of *MMI* couplers significantly.

### 5.4.3 Comparison with *MMI* couplers fabricated at Lucent Technologies Bell Labs

During my visit at Lucent Technologies Bell Labs I was allowed to place a set of *MMI* couplers on a mask that was processed in silica-on-silicon with a step-index of $\Delta n = 0.0116 = 0.008 n_{buf}$ and a height of $H = 6.4\,\mu$m. The *MMI*

couplers on this mask are obtained from the previously presented *MMI* couplers by scaling, in accordance with section 2.2. Consequently these *MMI* couplers can be compared directly with the previously presented couplers.

Fig. 5.23*A* shows the measured imbalance of the fabricated *MMI* couplers for a unknown linear polarization at a wavelength of $\lambda = 1557\,\text{nm}$. The excess loss has not been plotted, but it has a minimum of 0.2 $dB$ at $L_{MMI} = 3.15\,\text{mm}$ and varies by 0.8 $dB$ over the displayed range. The polarization dependent loss is $0.2 - 0.3\ dB$, which is much lower than what was obtained for the *MMI* couplers fabricated at *COM*. The figure shows the imbalance is decreasing with the *MMI* length from approximately 0.8 $dB$ at $L_{MMI} = 2.9\,\text{mm}$ to approximately 0.1 $dB$ at $L_{MMI} = 3.2\,\text{mm}$. Fig. 5.18*B* shows the measured imbalance as a function of the wavelength from $\lambda = 1507\,\text{nm}$ to $1607\,\text{nm}$ of the *MMI* coupler with $L_{MMI} = 3.15\,\text{mm}$. It is seen that the imbalance is between $0.0dB$ and 0.1 $dB$ over the entire wavelength range, which is as good as simulated and confirms that it is possible to fabricate *MMI* couplers with a very wavelength flattened behavior over a wavelength range of 100 nm.

These measurements show that the *MMI* couplers fabricated at Lucent Technologies Bell Labs have superior performance to the similar *MMI* couplers fabricated at *COM*. This confirms the hypothesis of a processing problem at *COM*, which hinders us in making high quality *MMI* couplers.

## 5.5 Summary

In this chapter planar $2x2$ optical 3 $dB$ couplers were examined. The couplers are basic building blocks in the design of optical devices in a *WDM* network. Hence it is essential that they have high tolerance towards inevitable process variations. Wavelength-flattened coupling is also important as many planar optical components are used over a wide wavelength range (1500 nm to 1600 nm).

Three different types of couplers were examined numerically: uniform directional couplers, interferometer based couplers and multi mode interference couplers. It was shown that for practically realizable uniform couplers the coupling coefficient increased with the wavelength. This implied that the cross coupling amplitude increased with the wavelength for uniform asymmetric couplers. Uniform symmetrical couplers are not wavelength flattened, but uniform asymmetric couplers can be designed for wavelength-flattened behavior with an imbalance of less than 0.2 $dB$ over the considered wavelength range. The trade off is a reduced process tolerance making the component very sensitive towards variations in the waveguide width reduction. The unbalanced Mach-Zehnder in-

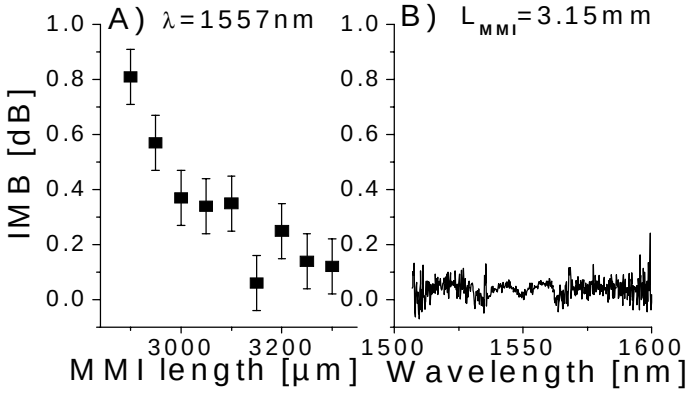


Figure 5.23: The measured imbalance of *MMI* couplers fabricated at Lucent Technologies Bell Labs as a function of *A*) the *MMI* length for a wavelength of $\lambda = 1557\,\mathrm{nm}$ and *B*) the wavelength for a *MMI* length of $L_{MMI} = 3.15\,\mathrm{mm}$.

terferometer coupler introduces an out-of-phase factor between the couplers to prevent the coupling ratio from monotonically increasing with the wavelength. The obtainable wavelength-flatness is similar to that of the uniform asymmetric coupler, but the process tolerance is much better. The coupler is more than twice as long the uniform coupler, but a numerical analysis showed that it can be scaled to the same length as the uniform asymmetrical coupler (at the original step-index) while maintaining superior process tolerance. The multi mode interference (*MMI*) coupler is not inherently loss less, but with respect to the imbalance the *MMI* coupler has wavelength-flattened performance. The numerical results showed better process tolerance and shorter length than the *UMZI* coupler. Consequently the numerical analysis showed that *MMI* couplers have better overall specifications than the other considered couplers.

The measurements for the uniform symmetrical couplers agrees quite well with the simulations, whereas the agreement is less for the uniform asymmetrical couplers. Although the general behavior was as simulated and a wavelength-flattened coupler was found. The measurements confirmed that this coupler type is very process sensitive, with a measured wafer-to-wafer variation for nominally identical coupler of up to 4% of the input power. It was emphasized that

complete agreement could not be achieved between the measurements and the simulations, even if the range of the process parameters were extended beyond what was expected. This meant that out waveguides can not be described as having a step-index refractive index profile. Due to processing problems the fabricated *UMZI* couplers had air bubbles in the coupling region and did not work. For the *MMI* couplers the agreement between measurements and simulations was reasonable. Fabricated couplers have a minimum loss of 0.4 $dB$ and the loss over the considered wavelength region is less than 0.7 $dB$. Furthermore the dependence of the access waveguide width and separation between the input waveguides was as simulated. However, the measured *MMI* couplers have large polarization dependent loss ($> 1$ $dB$) and an unexpected imbalance on the order of 0.6 $dB$. These effects were found for all fabricated *MMI* couplers and on several wafers. A numerical investigation showed that a parabolic error in the index distribution, with an error at the *MMI* edge of 0.5% of the step-index, can explain this effect. Such an error could be explained by non uniform stress, diffusion or variation of the waveguide height. It was shown that the imbalance can be removed by *UV*-trimming the *MMI* slab, which was in accordance with the theory. The observed discrepancies between the simulations and the measurements are likely to be caused by general fabrication problems. A set of similar *MMI* couplers, fabricated at Lucent Technologies Bell Labs, showed superior performance to the *MMI* couplers fabricated at *COM*, which corroborated the hypothesis of fabrication induced problems. In any case the measurements showed that the process tolerance of *MMI* couplers is less than what has previously been assumed.

# Chapter 6

# Multiplexers for waveguide amplifiers

This chapter concerns planar pump/signal multiplexers (*MUX*) for erbium doped waveguide amplifiers (*EDWA*), where the pump wavelength is 980 nm and the signal wavelength is between 1500 nm and 1600 nm. Several different architectures are considered as: a uniform symmetrical (*US*) directional coupler, a multi mode interference (*MMI*) coupler and a new design consisting of a point-symmetric Mach-Zehnder interferometer (*MZI*) of two uniform asymmetrical couplers. Experimentally data are presented for the *US* coupler and the *MMI* coupler *MUX*.

Parts of this work has resulted in a manuscript that has been accepted for presentation at *Integrated Photonics Research 2002* [96].

## 6.1 Introduction

The erbium doped fiber amplifier (*EDFA*) provides highly efficient amplification of an optical signal with a wavelength close to 1550 nm. The *EDFA* consists of a silica fiber with an incorporated low concentration of erbium ions and has a typical fiber length of $10 - 20$ m. By using a strong pump at either $\lambda = 980$ nm or 1480 nm a population inversion is created in the erbium ions, whence an optical signal in the third telecommunication window can be amplified by stimulated emission. Since the amplifier is made in silica fiber it can be connected directly to a standard fiber with basically no loss. The *EDFA* has a low noise

figure, negligible polarization dependence, no inherent crosstalk between different *WDM* channels and typical has a bandwidth of $30 - 40\,\text{nm}$, covering the so-called $C$-band [97]. However, it can also be designed to provide amplification in the $L$-band [98] and by using a dual stage amplifier it is hereby possible to achieve gain over a 80 nm passband [99].

The waveguide analogy to the *EDFA* is called the erbium doped waveguide amplifier (*EDWA*). The hitherto presented *EDWA's* cannot achieve the same total amount of amplification as the *EDFA* and therefore they can not compete with *EDFA's* for long haul applications. The main reason that *EDWA's* are interesting is that they allow for integration of several components on the same chip as a pump/signal *MUX*, an isolator or an optical tap for monitoring the output power and furthermore several *EDWA's* can be placed on the same chip to create an amplifying array. This minimizes the number of necessary fusion splices, whence the *EDWA* can achieve lower cost, higher reliability and smaller size than the *EDFA*. The marked for *EDWA's* is still in its infancy, but *EDWA's* have a very large potential e.g. in *METRO* networks to boost the power after it has passed through an optical cross-connect or to balance the power in different *WDM* channels [100].

At *COM EDWA's* have been processed in silica-on-silicon using a similar process to what is used for standard passive waveguides, the only principle difference is the addition of rare-earth dopants to the gas mixture. Accordingly the waveguides are highly compatible with standard fiber and integrated optics technology. To prevent clustering of the erbium ions in the glass their concentration is low, resulting in a low gain coefficient of 0.3 $dB/\,\text{cm}$, but by using a curled waveguide it has been possible to achieve a small signal net gain of more than 12 $dB$ over the entire $C$-band. The processing of *EDWA*'s is outside the scope of this work, but can for example be found in [101], [29].

It must be noticed that there are other possibilities to make *EDWA's*. By changing the host glass from to silica to either aluminosilicate or phosphate-based glasses the maximum dissolvable erbium concentration increases, whereby a gain coefficient of more than 3 $dB/cm$ have been reported [102], [103], [104]. However, phosphate glasses have narrower gain spectrum and alumina-based waveguides have significantly higher index than standard fibers, which complicates packaging of these components. Each of the sketched techniques have it pros and cons and it is currently unresolved which of them will become dominant.

This work focuses on design of an optical 980/1550 nm *MUX* for an *EDWA*. Ideally the *MUX* should have low loss at the pump wavelength ($< 0.5\ dB$) and at the signal wavelengths in particular ($< 0.3\ dB$), low fabrication and polarization

sensitivity and a small size (preferable less than 10 mm). The small size is important as the space on the wafer is restricted but also to minimize signal absorption in the *MUX* before the pump is multiplexed[1]. In continuation of chapter 5 and the previous discussion of the amplification band of the *EDWA* it is investigated how to design a *MUX* with a passband from 1500 nm to 1600 nm.

### 6.1.1 Choice of architecture

In the literature several different architectures has been considered to multiplex two widely spaced wavelengths. Here the uniform symmetrical coupler, the multi mode interference coupler and a new architecture consisting of a point-symmetrical Mach-Zehnder interferometer (*MZI*) of two uniform asymmetrical couplers are analyzed. Other possibilities are an asymmetric $Y$-branch splitter or a filter with discrete delays.

In the asymmetric $Y$-branch splitter the output waveguides are designed to have different dispersion, so that the difference between the effective index of the arms change sign between the pump and the signal wavelength [106] and the pump and signal are routed to different arms. To obtain the desired dispersion relation the waveguides must have different height, whence the device requires a more complex two-mask process and accordingly this architectures has not been considered.

In a filter with discrete delay the delay introduces a wavelength dependent phase shift, which determines where the signal is routed (assuming wavelength independent coupling). A simple example is a standard unbalanced *MZI* with two identical 3 *dB* couplers, in which the free spectral range is the inverse of the path length difference (see eq. 2.33). Another example is an unbalanced *MZI* structure consisting of a 4-port non-uniform coupler and a 3-port symmetrical $Y$-branch combiner, where the non-uniform coupler ensures that the pump and signal enter the interferometer arms with equal strength and a phase difference of either 0 or $\pi$ rad. By appropriate choice of the interferometer path length difference the phase difference will be zero at the symmetric $Y$-branch combiner for both wavelengths, whence the wavelengths are multiplexed [107], [108]. More complex multiple stage discrete filters are also a possibility, see e.g. [19]. However, filters with discrete delays in general are long, which is a critical issue for the pump/signal *MUX*. Accordingly these filters might primarily be of use for multiplexing either 1310/1550 nm or channels within the $C$-band.

[1] It is possible to make an active/passive interface on the wafer with very low loss [105], whence the multiplexer can be made in passive glass and the amplifier in active glass. However, this technique adds additional processing steps and should, if possible, be avoided.

### 6.1.2 Choice of multi or single-mode waveguides

It is desirable to use single-mode waveguides for optical components, but as shown in chapter 2 the normalized frequency is inversely proportional with the wavelength (see eq. 2.14) thus changing significantly from 1550 nm to 980 nm. This implies that a typical single-mode waveguide at 1550 nm is multi mode at 980 nm. For a rectangular step-index core with step-index $\Delta n = 0.010$ and waveguide height $H = 5.5\,\mu$m eq. 2.14 shows that a single-mode waveguide at $\lambda = 980$ nm has a width that is smaller than $W < 2.7\,\mu$m. This gives a normalized frequency of $V(1550\,\text{nm}) = 1.5$, whence it has very weak confinement leading to large bend loss.

In this work it was decided to work with waveguides that are multi mode at $\lambda = 980$ nm to extend the design flexibility at $\lambda = 1550$. If higher order modes of the waveguide (at $\lambda = 980$ nm) are excited this will lead to an increase in the excess loss as the higher order modes have low confinement, which leads to large bend losses. This problem is therefore expected to give a larger excess loss at low wavelengths and to decrease the tolerance with respect to alignment of the fiber to the input waveguide. A possible solution would be to use a design, where one input arm is straight and the other one is curved where the straight arm should be used as input for the pump. This was investigated in collaboration with Rasmus Sandberg in [109], but the measurements did not show an increase in excess loss for excitation through the curved input arm as compared to the straight arm, which indicates that the problem is insignificant. In addition to this, the design with one straight arm is not symmetrical outside the coupling region and thus can not achieve 100% coupling. A set of $2D$ $BPM$ simulations show that with this design it is not possible to achieve a maximum coupling of more than approximately 99% at $\lambda = 1550$ nm, giving a maximum isolation of 20 $dB$ [109]. Consequently the symmetrical design with two curved input arms seems to be better than the alternative design with one straight waveguide.

## 6.2 Theoretical investigation

In the following section simulation data for three different $MUX$ architectures are presented. The data are obtained using either $2D$ or $3D$ $BPM$ assuming rectangular step-index waveguides (for a comparison of the method see appendix A). The step-index is chosen to be $\Delta n = 0.010$ and the waveguide height is $H = 5.5\,\mu$m. Recall that the designs can be scaled to a different step-index using the scaling law that was derived in section 2.1.

### 6.2.1 Directional coupler *MUX*

The simplest possible $MUX$ is the uniform symmetrical ($US$) directional coupler, which can be produced either in a fiber [73] or a waveguide version [110]. The cross coupling in a $US$ coupler is (see section 5.2.1):

$$P_c^{US} = \sin^2[\frac{\pi(L_{st} + \delta L_b)}{L_{cp}}] \equiv \sin^2(\phi) \tag{6.1}$$

where $L_{st}$ is the length of the coupling region, $L_{cp}$ is the full coupling length, $L_b$ gives the coupling in the bends and $\phi$ is denoted the coupling strength. Eq. 6.1 shows that 100% cross coupling is obtained for coupling strengths that satisfy $\phi = \pi/2 + m\pi$, where $m \in N$.

The wavelength dependency can be found by differentiating eq. 6.1:

$$\frac{dP_c^{US}}{d\lambda} = 2\cos(\phi)\sin(\phi)\frac{d\phi}{d\lambda} \tag{6.2}$$

which shows that a 100% cross coupler will have $dP_c^{US}/d\lambda = 0$ implying that the architecture is wavelength-flattened around this maximum. The wavelength flatness of the maximum is extended if furthermore $d\phi/d\lambda = 0$, which can be achieved for a coupler with very closely spaced cores [69]. However, this coupler can not be produced due to process limitations (see section 3.2). For practically realizable couplers $d\phi/d\lambda > 0$. This implies that if the wavelength is decreased the cross coupling will decrease and eventually become negligible so that all the light will go straight to the bar port.

Fig. 6.1 shows a $2D$ $BPM$ calculation of the bar and cross coupling as a function of the wavelength for a $US$ coupler with a width of $W = 4.0\,\mu$m, center-to-center separation of $Sep = 9\,\mu$m and a length of the coupling region of $L_{str} = 1.25$ mm, which is chosen to give a coupling strength of $\phi = \pi/2$ at $\lambda = 1550$nm,[2]. The figure shows that around the pump wavelength of $\lambda = 980$nm the bar coupling ($P_b$) is high, but decreasing with the wavelength. At $\lambda = 980$nm it is $P_b \simeq -0.2\ dB$ and for wavelengths smaller than $\lambda = 1.06\,\mu$m it is higher than $-0.5\ dB$. The cross coupling ($P_{cr}$) has a maximum at $\lambda = 1.55\,\mu$m and is higher than $-0.2\ dB$ from $1.5\mu m$ to $1.6\mu m$. Fig. 6.1 shows that a $US$ coupler can be used as a 980/1550nm $MUX$ by using one input arm for the pump and the other input arm for the signal.

To investigate whether it is possible to increase the wavelength flatness the spectral response was simulated for three different $US$ couplers having the same

[2] These values of the width and separation gives a design that is insensitive towards variations in waveguide width reduction ($WWR$).

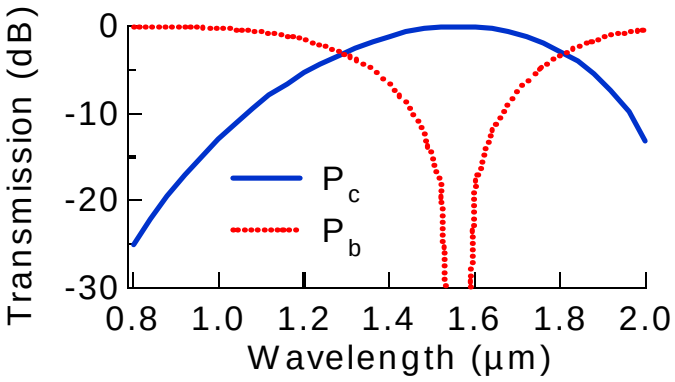


Figure 6.1: The simulated bar ($P_b$) and cross coupling ($P_c$) of a uniform symmetrical coupler as a function of the wavelength.

core width ($W = 4\,\mu$m), but different center-to-center separation in the coupling region, see fig. 6.2. For a separation of $Sep = 8.0\,\mu$m the length of the coupling region is $L_{st} = 0.72\,$mm, whereas a separation of $Sep = 10.0\,\mu$m requires a length of $L_{st} = 2.09\,$mm. The figure shows that the flatness of the maximum decreases with the separation between the waveguides. A direct comparison shows that the bandwidth over which $P_c > -0.3\ dB$ decreases from 170 nm at $Sep = 8\,\mu$m to $110\,\mu$m at $Sep = 10\,\mu$m. The trade off is that the coupling increases at small wavelengths (which can be seen on the left side of fig. 6.2), where the pump loss at $\lambda = 980\,$nm increases from 0.1 $dB$ at $Sep = 10\,\mu$m to 0.3 $dB$ at $Sep = 8\,\mu$m. The investigation shows that the best choice of separation depends on the exact specifications for which the $MUX$ is needed.

It was shown in chapter 5 that it is possible to design a $US$ coupler, which is tolerant towards changes in the waveguide width reduction, whence the most critical parameter becomes the step-index. For the chosen index step and height and for a separation of $Sep = 9.0\,\mu$m this is obtained with a waveguide width of $W = 4.0\,\mu$m, the design values that were previously presented. Simulations show that for this design the effect of a process deviation of $\delta\Delta n = 2 \cdot 10^{-4}$ is to induce a wavelength shift of approximately $\delta\lambda = 10\,$nm. Using the considered deviation the simulated minimum cross coupling over the considered wavelength range decreases to $P_c \simeq -0.3\ dB$, which is on the verge of commercially acceptable

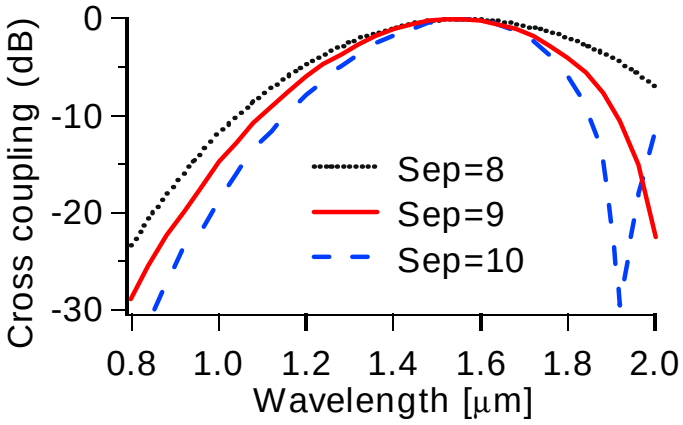


Figure 6.2: The $2D$ *BPM* simulated cross coupling $P_c$ for three different *US* coupler *MUXs* having waveguide widths of 4 $\mu m$ and different center-to-center separation $Sep \in \{8.0, 9.0, 10.0\}$ $\mu m$.

specifications.

### 6.2.2 Multi mode interference coupler MUX

In section 5.2.3 it was shown that a $2x2$ *MMI* coupler with infinite normalized frequency ($V = \infty$) regenerates the input field at any length that is an integer multiple of the characteristic length:

$$L = 0.5qL_c \qquad q \in N \tag{6.3}$$

$$L_c = 4\pi W_{MMI}^2 k n_{eff} = \frac{8\pi n_{eff} W_{MMI}^2}{\lambda} \tag{6.4}$$

where the image occurs at the cross arm if $q$ is odd and at the bar arm if $q$ is even. Eq. 6.3 shows that the *MMI* coupler can be used as a *MUX* if the length is chosen so:

$$L = 0.5pL_c(\lambda_1) \quad \wedge \quad L = 0.5qL_c(\lambda_2) \Rightarrow \tag{6.5}$$

$$\frac{p}{q} = \frac{n_{eff}(\lambda_2)}{n_{eff}(\lambda_1)} \frac{\lambda_1}{\lambda_2} \simeq \frac{\lambda_1}{\lambda_2} \tag{6.6}$$

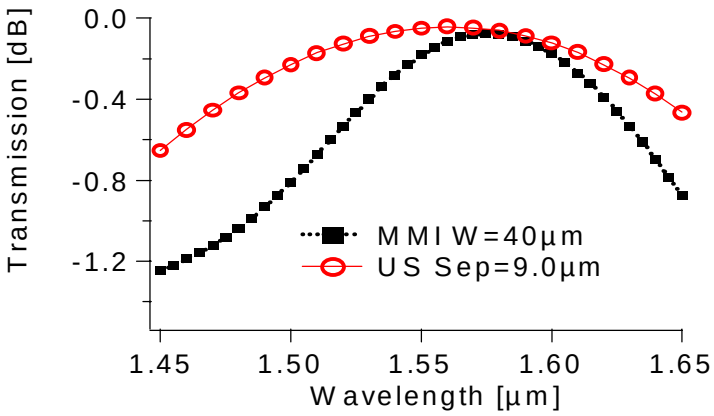


Figure 6.3: The simulated cross coupling $P_c$ as a function of the wavelength for a *MMI* coupler with $W_{MMI} = 40\,\mu$m and a *US* coupler with $Sep = 9.0\,\mu$m and $W = 4.0\,\mu$m.

where $p, q \in N$ and $p - q$ is odd. Inserting a pump wavelength of $\lambda_1 = 980\,$nm and a signal wavelength of $\lambda_2 = 1550\,$nm gives $\lambda_1/\lambda_2 = 0.63 \approx 2/3$, which shows that one can choose $p = 2$ and $q = 3$. For a real *MMI* the ratio of the characteristic lengths depends on the *MMI* width, whence it can be chosen to optimize the *MUX* [111]. Furthermore the characteristic length will be different for *TE* and *TM* polarized light, but it has been shown that by choosing a width in between the best value for the two polarizations a polarization independent *MUX* can be obtained [112].

For a dual-channel amplifier another possibility is to construct a *MUX*, which is a combination between a $1x2$ *MMI* and a $2x2$ *MMI*, whereby it has three input arms and two output arms. The pump enters the multi mode region through the central input port, which by symmetry yields the same power at both output ports, whereas the two signals enter from each their input port. The main advantage of this architecture is that by choosing $q = 1$ it is a factor of three shorter than the conventional $2x2$ *MMI MUX* [113]. However, it has larger loss and a lower process tolerance than the standard architecture, and is therefore discarded.

To investigate whether a *MMI* coupler is suitable for a pump/signal *MUX* a number of $2D$ *BPM* simulations were conducted. These simulations indicate

that the wavelength flatness of the *MMI* coupler is independent of the *MMI* width (in accordance with section 5.2.3). Thus a width of $W_{MMI} = 40\,\mu$m is chosen, as this is the same width as for the investigation of the 3 *dB MMI* coupler. Fig. 6.3 shows the simulated cross coupling as a function of the wavelength for a *MMI* coupler with width $W_{MMI} = 40\,\mu$m, access waveguide width $W_A = 19.0\,\mu$m, separation between the access waveguides $Sep_{MMI} = 26.0\,\mu$m and *MMI* length $L_{MMI} = 7.02\,$mm (compare with fig. 5.10). For reference the figure also contains the previously presented spectrum for the *US* coupler with a separation between the waveguides of $Sep = 9.0\,\mu$m. The figure shows that the wavelength response of the *MMI* coupler is not as flat as that of the *US* coupler. For wavelengths between 1500 nm and 1600 nm the minimum cross coupling of the *MMI* is $P_{cr} = -0.8\ dB$, which shows that the *MMI* coupler is not suitable as a *MUX* for a wide wavelength range. Notice that for 3 *dB* coupler the opposite conclusion was reached in chapter 5. The reasons are that the wavelength flatness of the *US* coupler is larger for a 100% than for a 3 *dB* coupler, and that the claimed wavelength flatness of the *MMI* coupler in chapter 5 is with regards to the imbalance, which is flattened because the excess loss of both arms have similar form as a function of the wavelength. Another concern with *MMI* couplers is that fabricated *MMI* couplers have an minimum excess loss of typically $0.2-0.3\ dB$, which is comparable to the maximum signal loss of the *US* coupler (due to coupling to the wrong arm) over the considered wavelength range. This indicates that the signal loss in the *MMI* coupler will be larger than in the *US* coupler.

Because of these effects the *MMI* coupler does not seems as a viable architecture for a pump/signal *MUX*.

### 6.2.3 Point symmetric Mach-Zehnder interferometer *MUX*

A uniform asymmetric (*UA*) 3 *dB* coupler can not have 100% cross coupling due to its asymmetry and therefore can not be used as a *MUX*. If instead two identical *UA* couplers are placed in a point-symmetric *MZI* (see fig. 6.4*A*) the cross coupling is [19]:

$$P_c = 1 - (1 - 2P_c^{UA})^2 \tag{6.7}$$

where $P_c^{UA}$ is the cross coupling of the individual uniform asymmetric couplers. Eq. 6.7 shows that 100% cross coupling is obtained if the constituent couplers are at the 3 *dB* point. Furthermore the first derivative of eq. 6.7 with respect

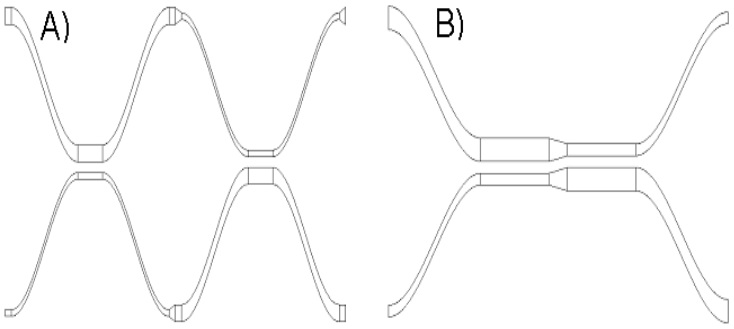


Figure 6.4: A schematic of *A*) a point symmetric *MZI* of two identical *UA* couplers where the widths are interchanged bewteen the two couplers and *B*) a similar *MZI* where the intermediate bends have been replaced by adiabatic tapers.

to the cross coupling of the individual couplers is zero at the 3 *dB* point:

$$\frac{\partial P_c}{\partial P_c^{UA}} = 4(1 - 2P_c^{UA}) \Rightarrow \frac{\partial P_c}{\partial P_c^{UA}}(P_c^{UA} = 0.5) = 0 \tag{6.8}$$

Thus the deviation from 100% cross coupling of the *MZI* is smaller than the deviation in the individual couplers from 50% coupling. Consequently the wavelength flatness of the *MZI* is larger than that of its couplers; a calculation shows that: $P_c^{UA} = 0.45 \Rightarrow P_c = 0.99$. In either case it is advantageous if the constituent couplers are wavelength flattened, which is achieved by a careful choice of asymmetry and coupling length (see section 5.2.1).

At the pump wavelength the point-symmetric *MZI MUX* works by having negligible coupling in analogy with the *US* coupler *MUX*. However, eq. 6.8 shows that for small values of $P_c^{UA}$ the *MZI*'s cross coupling will increase roughly as $4P_c^{UA}$ (because $\partial P_c/\partial P_c^{UA} \simeq 4$). Thus indicating that the *MZI* might suffer from large loss at the pump wavelength.

If the *MZI* is designed as in fig. 6.4*A* it will be roughly two times as long as the *US* coupler. Recall that the size of the *MUX* is critical, and since the path length difference between the interferometer arms is zero the only functionality of the bends is to separate the two arms before the width tapering is performed. Accordingly the bends can be replaced by adiabatic tapers inside the coupling

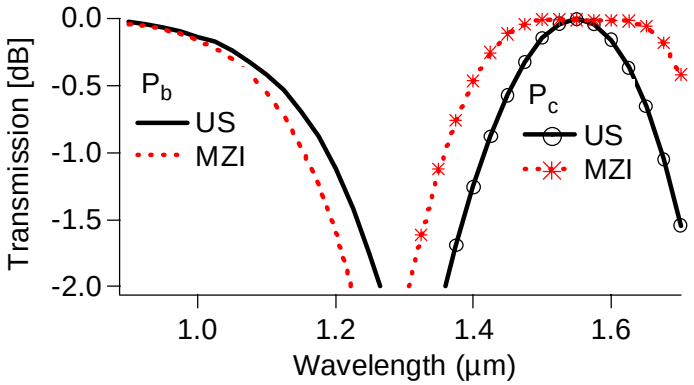


Figure 6.5: A $3D$ *BPM* simulation of the wavelength response of the point symmetric *MZI* coupler. The left side shows the bar coupling $P_b$ and the right side the cross coupling $P_c$. For comparison the figure also contains simulation data for a *US* coupler.

region to shrink the component size, see fig. 6.4*B*.

Rasmus Sandberg has conducted a number of simulations to find an optimized design for this architecture. Fig. 6.5 shows a $3D$ *BPM* simulation of the wavelength response of a point-symmetric *MZI* coupler with widths $W_1 = 5.43\,\mu$m, $W_2 = 5.08\,\mu$m, center-to-center separation of $Sep = 11.0\,\mu$m, coupling region length $L_{st} = 3.1\,$mm and a linear taper between the two regions with a length of $L_{tap} = 300\,\mu$m, [3]. For comparison the figure also contains a $3D$ *BPM* simulation of the wavelength response of a *US* coupler. The figure shows that the point-symmetric *MZI* has similar bar coupling at the pump wavelength as the *US* coupler, with $P_b(\lambda = 980\,\text{nm}) \simeq -0.15\ dB$. This is somewhat surprising, but is caused by that the asymmetry increases as the wavelength decreases, whence the cross coupling amplitude at the pump wavelength is small. The figure furthermore shows that the region over which the cross coupling is high is extended as compared to the *US* coupler. The bandwidth at $-0.1\ dB$ is approximately 200 nm and 250 nm at $-0.2\ dB$, which is more than a factor of two larger than that of the *US* coupler.

[3] It is unfortunate that the considered center-to-center separation is so large, as it gives an impression of a rather long multiplexer. By choosing a smaller separation it is possible to find a smaller device with similar performance.

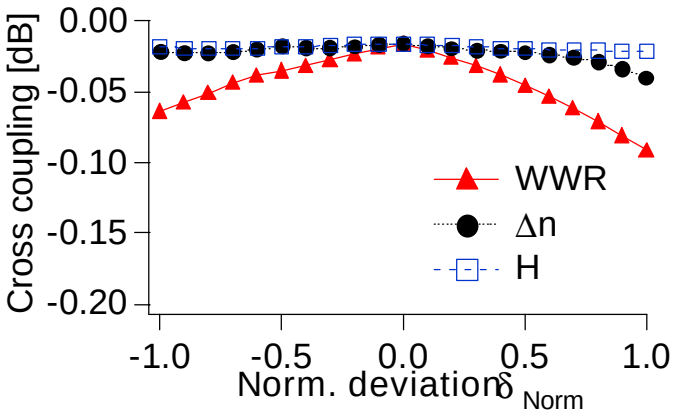


Figure 6.6: The smallest value of the simulated cross coupling (by $2D$ $BPM$) of the optimized point symmetric $MZI$ over a wavelength range from $\lambda = 1500\,\text{nm}$ to $1600\,\text{nm}$ as a function of the normalized deviation in the process parameters: waveguide width reduction $WWR$, step-index $\Delta n$ and height $H$.

To investigate the process tolerance of the point-symmetric $MZI$ the waveguide width reduction $WWR$, step-index $\Delta n$ and height $H$ are varied from their nominal value. As the $MUX$ is investigated from $\lambda = 1500\,\text{nm}$ to $1600\,\text{nm}$ the worst case behavior over this passband is considered. Fig. 6.6 shows the minimum value of the cross coupling from $\lambda = 1500\,\text{nm}$ to $1600\,\text{nm}$ as a function of the normalized deviation in the process parameters (defined in equation 5.5). The figure shows that the point-symmetric $MZI$ is very tolerant towards changes in all the three considered parameters. The deviations in step-index and height have nearly no effect, and even for the maximum deviation in $WWR$ the cross coupling is still more than $-0.1\,dB$ over the entire wavelength range. The simulations show that the point-symmetric $MZI$ has better process tolerance than the $US$ coupler. Consequently it is very well suited for multiplexing signals for $EDWA$'s. It furthermore has the advantage that one design can be used over the entire considered wavelength range, which eliminates the need for fine tuning the coupler depending on the particular application.

### 6.2.4 *MUX* for 980/1550 nm and 1480/1550 nm

The previous discussion described a 980/1550 nm *MUX* for *EDWA's*. However, it is also possible to pump the *EDWA* at a wavelength of $\lambda = 1480\,\text{nm}$. Conventionally a 1480/1550 nm *MUX* is fabricated as an unbalanced *MZI*, where the path length difference is chosen to ensure a half period of $\delta\lambda = 70\,\text{nm}$, which corresponds to a free spectral range of the *MZI* of:

$$FSR = 2(\frac{c}{1480nm} - \frac{c}{1550mn}) \simeq 1.8 \cdot 10^{13}\,\text{Hz} \tag{6.9}$$

by eq. 2.33 this can be obtained with an interferometric path length difference of:

$$\Delta L = \frac{1}{FSR}\frac{c}{n_{eff}} \Rightarrow \Delta L \simeq 11\,\mu\text{m} \tag{6.10}$$

Assume that this path length difference between the two arms is obtained by making one arm straight and letting the other arm consist of four concatenated circular arcs. A path length integral and a Taylor expansion shows that the path length difference is related to the length along the propagation axis by:

$$L \simeq (4R)^{2/3}(6\Delta L)^{1/3} \qquad \Delta L << R \tag{6.11}$$

For $R = 10\,\text{mm}$ and $\Delta L = 11\,\mu\text{m}$ this gives $L \simeq 4.8\,\text{mm}$. Thus it is possible to create a planar *MZI MUX* with an acceptable length. The coupling at low wavelengths for an unbalanced *MZI* can be estimated from the wavelength dependency of the *US* coupler. In section 6.2.1 it was shown that a *US* coupler *MUX* has a bar coupling at the pump wavelength of $P_b(\lambda = 980\,\text{nm}) \simeq -0.15\ dB$. By comparison with eq. 6.1 it is seen that this corresponds to a coupling strength of:

$$P_b(\lambda = 980nm) \simeq -0.15dB \Rightarrow \phi \simeq 0.17 \tag{6.12}$$

To estimate the worst case behavior assume that the phase difference between the two arms is zero at $\lambda = 980\,\text{nm}$, whence the bar coupling is given from twice the coupling strength of the individual couplers:

$$P_b(\lambda = 980nm, 2\phi) \simeq -0.5dB \tag{6.13}$$

which is in the high end of the range of acceptable losses at the pump wavelength. Another issue is that due to the path length difference the response of the *MZI* is not flat from 1500 to 1600 nm.

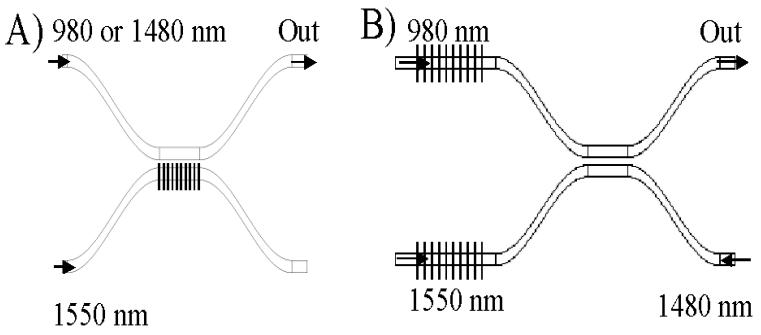


Figure 6.7: Schematic of possible *MUX* architectures for both 980/1550 nm and 1480/1550 nm. *A*) a grating frustrated coupler and *B*) an interferometer based coupler, where the pump signals at 980 nm and 1480 nm enter through different arms. In both cases the grating has a resonance wavelength of $\lambda = 1480$ nm.

The previously discussed architectures for 980/1550 nm *MUX*s can not be used directly as 1480/1550 nm *MUX*s. But by post processing the *US* coupler it might be possible to create a *MUX* that works for both wavelengths bands. One possibility is to inscribe a strong Bragg grating in one of the waveguides in the coupling region, see fig. 6.7*A*. Close to the resonance the Bragg grating introduces dispersion, whereby the coupler effectively becomes asymmetric. If the Bragg grating is sufficiently strong it will effectively frustrate the coupler and prevent any coupling at the grating wavelength [114], [115]. It is not trivial to fabricate a grating frustrated coupler with good specifications, e.g. the Bragg grating should only be present in one waveguide, which requires shielding one waveguide with an opaque pattern or using a tightly focused laser beam to inscribe the grating. Another problem arises due to coupling of the scattered light with the cladding modes, which might be a problem for this implementation. A practical problem is that the fabrication of the Bragg grating will induce a general change of index in one arm of the coupler and induce an asymmetry in the coupler. However, this can subsequently be removed by *UV*-trimming the other arm [116].

Fig. 6.7*B* shows another possible architecture, which is similar to a Mach-Zehnder optical add/drop multiplexer, where the Bragg grating has a resonance wavelength of $\lambda = 1480$ nm. The $\lambda = 1480$ nm pump is multiplexed from the

hitherto unused arm in the coupler, provided that the coupler has $3.dB$ cross coupling at 1480 nm. The Bragg grating has no effect at neither $\lambda = 980\,\text{nm}$ nor $\lambda = 1550\,\text{nm}$. Accordingly it requires 100% cross coupling at 1550 nm. Consequently the coupler must have a larger wavelength dependency than the previously described *US* couplers. This can be achieved by using a coupler with a larger coupling strength.

## 6.3 Experimental investigation

The *MUX*s that are presented in the following section were fabricated using the standard recipe for passive waveguides at *COM* and have a step-index of $\Delta n = 0.010$ and height of $H = 5.5\,\mu\text{m}$. The measurement of the *MUX*s were performed by Rasmus Sandberg using an unpolarized white light source (see section 3.5). The spectra were recorded on an optical spectrum analyzer using a resolution of $res = 5.0\,\text{nm}$, whence it is not possible to detect rapid variations with the wavelength. These measurements give a qualitative analysis of the *MUX*s.

Fig. 6.8 shows the bar and cross coupling from $\lambda = 900\,\text{nm}$ to 1600 nm, where fig. 6.8*A* is for a *US* coupler with width $W = 4.0\,\mu\text{m}$ and separation $Sep = 9.0\,\mu\text{m}$ and fig. 6.8*B* is for a *MMI* coupler with width $W_{MMI} = 40\,\mu\text{m}$ and length $L_{MMI} = 7.0\,\text{mm}$. For the *US* coupler the functional form of the spectrum is in good agreement with the simulations. The bar coupling at the pump wavelength is $P_b(\lambda = 980\,\text{nm}) = -0.2\ dB$, which is as good as simulated. This particular coupler achieves its maximum cross coupling at $\lambda \simeq 1.53\,\mu\text{m}$ where the difference between the two arms is 17 $dB$. Compared to the maximum cross coupling the *US* coupler has a $-0.2$ $dB$ spectral width of 86 nm and a $-0.3$ $dB$ spectral width of 122 nm, which is in agreement with the simulated spectral dependency (see section 6.2.1). A comparison between measurements and simulations for numerous couplers [109] showed, that it is not possible to find a fixed value for the process parameters, which describes all the *US* couplers. This means that it is not possible to describe the couplers completely within the step-index refractive profile model.

With regards to the *MMI* couplers the similarity between the measurements and simulations is very poor (compare fig. 6.8*B* and fig. 6.3). This shows that we have very large problems in making *MMI* couplers, in agreement with what was found for 3 $dB$ couplers (chapter 5).

The new architecture with the point-symmetric *MZI MUX* has not been fabricated, yet. Measurement show that our waveguides can not be completely

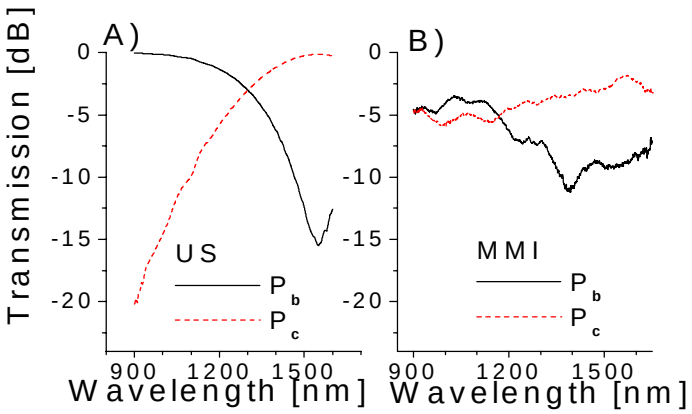


Figure 6.8: The measured bar $P_b$ and cross coupling $P_c$ as a function of the wavelength of $A$) a *US* coupler and $B$) a *MMI* coupler.

described within a rectangular step-index model. However, the fabricated couplers have similar wavelength dependency to the simulations and furthermore it has been possible to fabricate a wavelength flattened *UA* 3 $dB$ coupler (see section 5.3). In conclusion it seems possible to fabricate a wavelength flattened point-symmetric *MZI MUX* by including several slightly different designs on the wafer.

## 6.4 Summary

This chapter concerned planar pump/signal multiplexers for erbium doped waveguide amplifiers, where the pump wavelength was 980 nm and the signal wavelength was between 1500 nm and 1600 nm. The simplest possible solution was the uniform symmetrical (*US*) coupler, which utilized that the coupling coefficient is much larger at 1550 nm than at 980 nm. Thus the coupler was designed to have 100% cross coupling at 1550 nm and very small coupling at 980 nm (with a bar coupling of approximately $-0.15$ $dB$). Simulations showed that a *US* coupler has a $-0.2$ $dB$ passband of approximately 100 nm where the passband width increased slightly with the coupling coefficient. The main conclusion was that

the coupler should be as process tolerant as possible, which was achieved by choosing a design that is insensitive to variation in the waveguide width reduction. The effect of inevitable process parameter variation was to shift the wavelength of maximum coupling by up to 10 nm thus increasing the maximum signal loss over the passband to 0.3 $dB$, which is on the verge of commercially acceptable specifications. Multimode interference (*MMI*) couplers were also considered. However, the simulated wavelength flatness was inferior to that of the *US* coupler and furthermore *MMI* couplers have an excess loss even at the optimal wavelength. Therefore a *MMI* coupler is not an optimal choice for this application. Finally a new design consisting of a point-symmetric Mach-Zehnder interferometer of two identical uniform asymmetrical couplers was considered. To minimize the length of the design the intermediate bends were replacing by adiabatic tapers. Simulations showed that the new design had low loss at the pump wavelength (less than 0.2 $dB$) and a very wavelength flattened cross coupling with a $-0.1$ $dB$ passband of approximately 200 nm. The simulations furthermore showed that the architecture maintained a signal loss of less than 0.1 $dB$ from 1500 to 1600 nm even when realistic process variations were taken into account. Accordingly it had better process tolerance than the *US* coupler. Thus it is very well suited for multiplexing signals for *EDWA*'s, and furthermore has the advantage that one design can be used over the entire considered wavelength range, which eliminates the need for fine tuning the coupler depending on the particular application.

The measurements for fabricated *US* couplers qualitatively were in agreement with the simulations, giving a pump loss of $-0.1$ $dB$at $\lambda = 980$ nm and a $-0.2$ $dB$ wavelength band of more than 80 nm. However, as in chapter 5, the measurements and simulation did not agree completely, which showed that the step-index model is not an adequate description of the waveguides. For *MMI* couplers the measured performance was very poor, which confirmed our previously described problems with fabricating these components. The new point-symmetric *MZI* architecture has not been fabricated yet, but it seems possible to do achieve excellent performance by including several slightly different designs on a wafer.

The chapter also contained a brief discussion of possible architectures for *MUX*s that work at both 980/1550 nm and 1480/1550 nm, where both an unbalanced interferometer and two different grating based structures were considered.

# Chapter 7

# $1x4$ passive optical *MUX/DEMUX*

This chapter concerns a $1x4$ generalized Mach-Zehnder interferometer (*GMZI*) based passive optical multiplexer/demultiplexer. However the design can be generalized to a $1xN$ optical *MUX/DEMUX*, as long as $N$ is small. The interferometer arms in the *GMZI* have lengths that differ by units of a discrete delay and each contain a single-stage all-pass filter. Some different optical multiplexers are sketched followed by a description of single-stage all-pass filters. The transmission and dispersion spectrum of the *GMZI* are calculated, and it is shown that the all-pass filters incur an excellent transmission, but the tradeoff is a detrimental cubic like dispersion. Accordingly it is investigated how to minimize the dispersion by appropriate choice of the all-pass filters and by inclusion of additional non linear phase filters. It is shown that the dispersion is reduced by more than an order of magnitude by placing a three-stage all-pass filter on the input arm. A loop transmission simulation shows that the compensating all-pass filter significantly improves the performance if several *GMZI's* are cascaded. Finally the requirements for fabricating the sketched *GMZI* are considered, including its process tolerance.

The presented material is mainly based on work performed in collaboration with Christi K. Madsen during a six months stay at Lucent Technologies Bell Labs, Murray Hill, New Jersey, USA. Parts of this chapter have been accepted for publication in the journal *Optics Letters* [117], while other parts have been accepted for presentation at the *European Conference on Optical Communica-*

*tion* 2002 [118].

## 7.1 Introduction

$1xN$ passive optical multiplexers are used in wavelength division multiplexed ($WDM$) networks as multiplexers/demultiplexers ($MUX/DEMUX$) of the individual wavelength channels or as interleavers/deinterleavers in which a number of these channels are routed collectively. For large $N$ passive optical $MUX$s are conventionally fabricated as waveguide grating routers ($WGR$)[1]. The $WGR$ is a rather complicated component, but its complexity does not scale linearly with $N$ and thus it is possible to make $WGR$'s for a large number of channels. $WGR$'s with a Gaussian passband have essentially no dispersion [119] and can have very low crosstalk. The trade-off for increasing passband flatness is an increase in the passband loss and dispersion [120], [121], [122]. For small $N$ there are several other possibilities than the $WGR$ to build optical $MUX$s, e.g. based on gratings [123], thin film [124] or interferometer components [125], [126]. In this work integrated optical interferometer based components are considered. A $1xN$ optical interferometer can be constructed either as a cascade of $2x2$ interferometers with free-spectral ranges ($FSR$) that vary by powers of two from stage to stage [125], or as a $1xN$ generalized Mach-Zehnder interferometers ($GMZI$) [126]. The two different architectures have identical responses, whence the discussion is restricted to the $1xN$ $GMZI$ without loss of generality. In principle the $1xN$ $GMZI$ could be constructed for any $N$, but it is in practice limited to low $N$ by the difficulty of making uniform, loss less $NxN$ couplers for large $N$. Inherently the spectral response of a $1xN$ $GMZI$ has large cross talk between adjacent bands and lacks passband flatness [125], but it is possible to improve this performance by including carefully chosen single-stage all-pass filters in each interferometer arm [126]. For simplicity the discussion in this chapter is restricted to a $1x4$ $GMZI$ used as a $DEMUX$, although the architecture may generally be used for other values of $N$ and as a $MUX$.

## 7.2 All-pass filters

An all-pass filter is a device with a unit amplitude transfer. All-pass filters are not minimum phase filters and their amplitude and phase response do not obey the Kramers-Kroning relation [119]. A single-stage all-pass filter can be

[1] Waveguide grating routers are also referred to as arrayed waveguide gratings or phasars.

realized as an optical $2x2$ coupler where one arm is fed back to the input (a ring coupler) or as two reflectors separated by a distance $L$, where the first reflector is partial whereas the second is a 100% reflector. The single-stage all-pass filter is characterized by its $FSR$, pole magnitude ($\rho$) and position of the resonance within the $FSR$, which is given by a phase parameter ($\phi$). In the ring coupler implementation the $FSR$ is given from the ring circumference, the pole magnitude (the through port amplitude of the coupler) and the position of the resonance (from the phase after traversing the ring once). In the reflecting cavity implementation the $FSR$ is given from twice the cavity length, the pole magnitude from the partial reflectance and the position of the resonance from the phase after traversing the cavity once. The transfer function of a single-stage all-pass filter is [25]:

$$T(z) = \exp(-i\phi)\frac{\rho\exp(i\phi) - z^{-1}}{1 - \rho\exp(-i\phi)z^{-1}} \tag{7.1}$$

where the unit delay $z^{-1}$ is defined as: $z^{-1} = \exp(-i\omega\Delta T)$ and the pole magnitude must satisfy: $0 \leq \rho < 1$. By using the definition for the normalized frequency $f_N$ (eq. 2.35) it is seen that: $z^{-1} = \exp(-i2\pi f_N)$. Eq. 7.1 shows that a single-stage all-pass filter has one zero and one pole, which are mirror images about the unit circle thus giving unit magnitude response for all frequencies. The filters phase is:

$$\theta \equiv \tan^{-1}[\frac{\mathrm{Im}(T)}{\mathrm{Re}(T)}] \tag{7.2}$$

$$= \tan^{-1}[\frac{(1-\rho)\sin(2\pi f_N + \phi)}{2\rho - (1+\rho^2)\cos(2\pi f_N + \phi)}] \tag{7.3}$$

Fig. 7.1 shows the phase response as a function of the normalized frequency for three different all-pass filters having the same $FSR$ and $\phi = \pi$ (giving resonance at $f_N = 0.5$ ) but with pole magnitudes of $\rho \in \{0; 0.25; 0.50; 0.75\}$. The figure shows that the phase at resonance ($f_N = 0.5$) and anti-resonance ($f_N \in \{0, 1\}$) is independent of the pole magnitude. For zero pole magnitude $\rho = 0$ the phase is linear with the frequency, but for non-zero pole magnitude the phase response is non-linear with a deviation from the linear response that increases with the pole magnitude. Close to the resonance the slope is increased, and close to anti-resonance it is decreased. Notice that the slope close to anti-resonance decreases with the pole magnitude.

The normalized dispersion is obtained by differentiating the phase response $\theta$ twice with regards to the normalized frequency (eq. 2.37). For a single-stage all-pass filter it is:

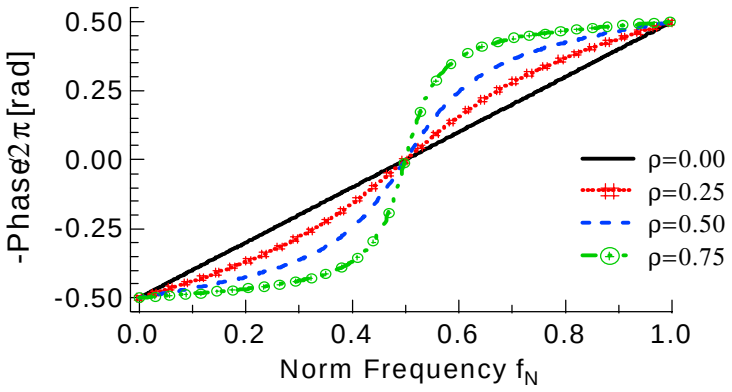


Figure 7.1: The phase response of single-stage all-pass filters with $\phi = \pi$ as a function of the normalized frequency $f_N$ for pole magnitudes of $\rho = \{0; 0.25; 0.50; 0.75\}$. The filters have resonance at $f_N = 0.5$ and anti-resonance at $f_N = 0$.

$$D_N = \frac{4\pi\left(\rho^2 - 1\right)\rho[\sin\left(2\pi f_N + \phi\right)]}{[1 + \rho^2 - 2\rho\cos\left(2\pi f_N + \phi\right)]^2} \tag{7.4}$$

Eq. 7.4 shows that the normalized dispersion is identically zero for $\rho = 0$, which was expected since the phase response is linear for $\rho = 0$. The normalized dispersion is plotted in fig. 7.2 as a function of the normalized frequency for all-pass filters with $\phi = \pi$ for pole magnitudes of $\rho \in \{0; 0.25; 0.50\}$. The normalized dispersion is zero at resonance and at anti-resonance. Close to resonance ($f_N = 0.50$) the normalized dispersion is decreasing with the frequency while close to anti-resonance it is increasing with the frequency. Fig. 7.2 shows that the maximal normalized dispersion increases with the pole magnitude. As the pole magnitude approaches unity the maximal normalized dispersion increases rapidly, e.g. the maximum dispersion for $\rho = 0.75$ is more than five times as large as than for $\rho = 0.50$. Furthermore the width of the region, in which the normalized dispersion increases with the frequency, also increases with the pole magnitude. An analysis of eq. 7.4 shows that the increasing region is larger than the decreasing region for all non-zero pole magnitudes, whereas they are

of equal size for $\rho = 0$.

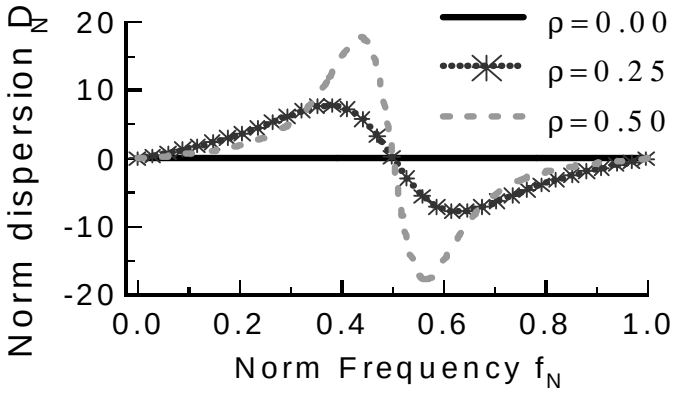


Figure 7.2: The normalized dispersion of a single-stage all-pass filter with $\phi = \pi$ as a function of the frequency for pole magnitudes of $\rho \in \{0; 0.25; 0.50\}$. Close to anti-resonance ($f_N = 0.50$) the normalized dispersion is decreasing with the frequency.

If several single-stage all-pass filters are cascaded or placed in a lattice architecture they form a new all-pass filter, which is termed a multiple-stage all-pass filter [127]. It can be shown that any desired phase response can be approximated by a multiple stage all-pass filter [128].

## 7.3 Working principles of the $1x4$ *GMZI*

The following section describes the working principles of the $1x4$ *GMZI* with all-pass filters. The passband is assumed to be 60% of the channel spacing. The layout of a $1x4$ *GMZI* with ring couplers as all-pass filters in the interferometer arms is shown schematically in fig. 7.3. It consists of a uniform $1x4$ coupler, 4 interferometer arms with delays differing by units of $\Delta T$ and a uniform $4x4$ coupler. The couplers are assumed to be wavelength independent over the wavelength range of interest[2]. Let the interferometer arms be designated

[2] For a practical implementation the $FSR$ is on the order of a nanometer. For an interleaver appplication the $DEMUX$ should work over several $FSR's$. Thus it is desirable that the

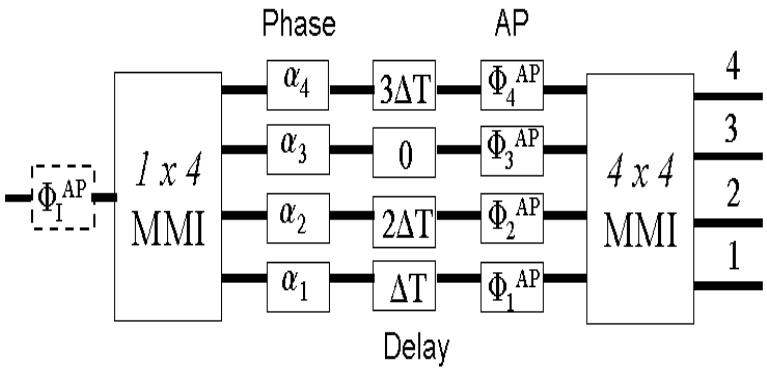


Figure 7.3: Schematic of a $1x4$ *GMZI* using *MMI* couplers as splitter and combiner. The phase controllers are denoted by $\alpha_q$, and the all-pass filters by $\Phi_q$. The delays are given directly in terms of the unit delay $\Delta T$. The dotted box on the input arm shows the additional all-pass filter used for dispersion compensation (see section 7.5).

by $q$. On each interferometer arm there is a phase controlling element ($\alpha_q$) and an all-pass filter having a delay of $\Delta T^{AP}$ a pole magnitude $\rho_q$ and a frequency of $\phi_q$. The reflective cavity implementation is similar to the architecture shown in 7.3. However, it is folded around the all-pass filters whence the path length differences should be halved.

Consider the standard $1x4$ *GMZI* without the all-pass filters. The phase in each interferometer arm varies linearly with the frequency. As the arms have different delay the slope of phase response is different and the phase differences between the arms varies linearly with the frequency. At the center of each of the four passbands the phase differences are equal to an integer number of $\pi/2$ thus all the light is guided to one specific output channel. However, the phase difference changes when the frequency moves away from the center of the passband resulting in a decrease in transmission. Therefore the standard $1x4$ *GMZI* lacks passband flatness. It furthermore has large crosstalk between adjacent bands [126]. The purpose of the all-pass filters is to maintain the frequency difference between the interferometers arms constant over the entire passband. Since this is required for all the channels it implies that the all-

couplers have a wavelength flattened performance over at least **20** $nm$.

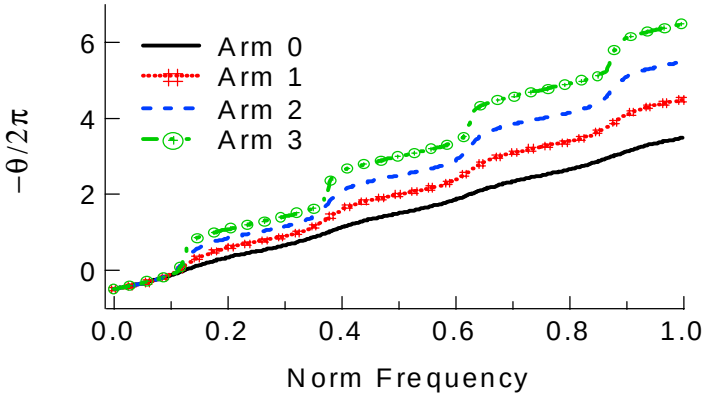


Figure 7.4: The phase response of the interferometer arms in the *GMZI* after inclusion of the optimized all-pass filters.

pass filters should have a $FSR$, which is equal to the channel spacing (i.e. 4 times smaller than the $FSR$ of the $GMZI$), whereby $\Delta T^{AP} = 4\Delta T$. Recall from section 2.7 that the total phase of a cascade of components is equal to the sum of the individual phase and from section 7.2 that a single-stage all-pass filter flattens the phase response close to its anti-resonance with a slope that decreases with the pole magnitude. It is seen that the phase difference is flattened by adding single-stage all-pass filters in the $GMZI$ arms, which are at anti-resonance at the central frequency ($\phi = \pi$) and have pole magnitudes that decrease with the length of the arm. By minimizing the deviation in phase difference over the passband the following pole magnitudes were found $\rho = [0.148, 0.383, 0.611, 0.851]$ [129], resulting in the phase response shown in fig. 7.4. Fig. 7.4 shows that the phase response is flattened around the four passbands at $f_N \in \{0; 0.25, 0.50; 0.75\}$.

Given the phase response of the interferometer arms and assuming ideal splitting the transmission spectrum is found by a norm preserving discrete Fourier transform [25]. The transmission spectres of the 4 arms have identical shape, but are shifted with an integer number of channel spacings. The origin of the symmetry is that the transmission spectres in the standard $1x4$ $GMZI$ have identical shape and that the all-pass filters have identical response for all 4 channels (as their $FSR$ is equal to the channel spacing). Fig. 7.5 shows the

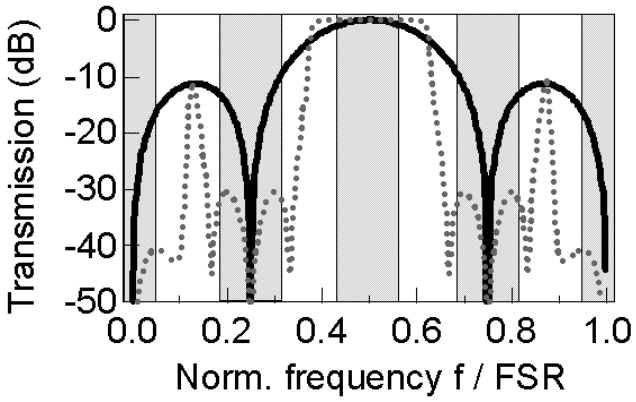


Figure 7.5: The transmission response of the $1x4$ *GMZI* with (dots) and without all-pass filters (full line) in the interferometer arms. The passbands are indicated as transparent patterned boxes.

transmission spectrum of one arm of the *GMZI* with (dots) and without (line) optimized all-pass filters in the interferometer arms. Patterned boxes indicate the position and width of the 4 passbands. The figure shows that the response is flattened with a loss over the considered passband of less than 0.05 $dB$ (as compared to 1.2 $dB$ for the standard *GMZI*). The crosstalk suppression over the passband of the other channels is more than 31 $dB$ (as compared to 13 $dB$). Fig. 7.5 also shows that the *GMZI* has two unwanted transmission peaks with a power of $-11$ $dB$, which are situated 1.5-channel spacing from the central frequency and accordingly they are outside the passband of all the channels. Their origin is that the phase response of single-stage all-pass filters at resonance and anti-resonance is independent of the pole magnitude (as shown in section 7.2), leaving the phase difference and the transmission at the center of each channel and at the midpoint between adjacent channels unchanged.

To examine the flatness of the transmission the bandwidth narrowing induced by cascading the *GMZI* is calculated. Define the bandwidth narrowing factor as the ratio of the $-3$ $dB$ filter bandwidth after transmission through the considered number of filters to the $-3$ $dB$ filter bandwidth after one filter. The bandwidth narrowing factor is found by matrix algebra on the filters transfer

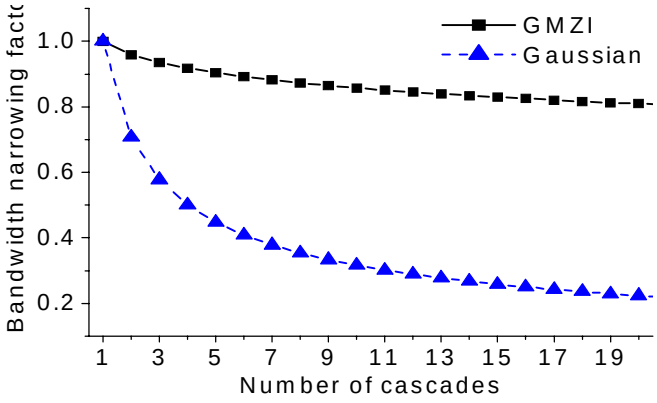


Figure 7.6: The bandwidth narrowing factor (at $-3$ $dB$) as a function of the number of casdades. Data are shown for the *GMZI DEMUX* and for a filter with a Gaussian transmission. The *GMZI* has superior performance to the Gaussian filter.

matrix, and thus is independent of the signal bandwidth. Fig. 7.6 shows the bandwidth narrowing factor for the considered *GMZI DEMUX* and for a filter with a Gaussian amplitude transfer (which resembles that of the *GMZI* without all-pass filters). The figure shows that the bandwidth decreases rapidly for the Gaussian filter, where the bandwidth is halved after transmission through 4 components. In comparison the decrease is slow for the *GMZI*, which maintains more than 80% of the original bandwidth after transmission 20 components.

## 7.4 Dispersion of the $1x4$ *GMZI DEMUX*

The trade-off involved in adding all-pass filters to the *GMZI* is that they have a non-zero dispersion. Consequently it becomes relevant to study the *GMZI*s dispersion, which is done using a combination of the transfer matrix method and a $Z$-transform analysis. The transfer matrices of the *MMI* couplers, phase controlling elements, delays and all-pass filters can all be found in the literature [25]. The calculation of the total transfer matrix is straightforward although

lengthy, giving 4 transfer functions of the following form:

$$T_{1,m}(z) = \frac{\sum_{r=0}^{19} b_m(r) z^{-r}}{1 + \sum_{s=1}^{4} a(4s) z^{-4s}} \tag{7.5}$$

where $m$ is the number of the output arm and the filter coefficients $b_m(r)$, $a(s)$ depend on the pole magnitudes in the single-stage all-pass filters. The coefficients are not given here, but can be found in appendix C. Notice that the denominator only contains terms corresponding to an integer number of round trips in the ring couplers ($a_4, a_8, a_{12}$ and $a_{16}$) and that the coefficients in the denominator are independent of the choice of output arms. The coefficients in the numerator depend on the choice of output arm (i.e. on $m$), but are related by:

$$b_2(r) = i^m b_1(r) \qquad b_3(r) = i^{(3m+2)} b_1(r) \qquad b_4(r) = i^{2m} b_1(r) \tag{7.6}$$

where $r$ is the order of the term as defined in eq. 7.5. Eq. 7.6 shows that the numerator polynomials resemble each other, e.g. the norm is independent of $m$.

The frequency dependence can be found by a $Z$-transform of the transfer function (see section 2.9). It was shown in section 7.3 that the transmission amplitudes have the same shape for the different output arms. An analysis of eq. 7.5 and 7.6 shows that this is not only valid for the amplitude but also the phase response. Thus the dispersion of all the output arms have identical shape and it is sufficient to consider one output arm, which simplifies the problem considerably. The normalized dispersion of the *GMZI* with the optimized all-pass filters as a function of the normalized frequency is shown in fig. 7.7. Notice that only frequencies in the passband are shown, which is different than on the prior graphs. Fig 7.7 shows that the normalized dispersion is increasing with the frequency over the passband. It is zero at the center of the passband is anti-symmetric around this point, and has a cubic shape. The effect of this type of dispersion is pulse broadening on the rising edge of the pulse and an oscillatory trailing part of the pulse [127]

The origin of the dispersion shape is the all-pass filters are, since they are the only dispersive elements in the *GMZI*. They are at anti-resonance at the center of the passband and thus add normalized dispersion that is increasing with the frequency (see section 7.2). The maximal normalized dispersion in the passband occurs at its edges and is $\max\{D_N\} \simeq \pm 50$. The average normalized dispersion slope over the passband is found from a linear fit: $\overline{S}_N = 5.1 \cdot 10^2$. Fig. 7.7 also shows a linear fit to the dispersion and the difference between the dispersion of the *GMZI* and the linear fit. The difference has maximum amplitude of

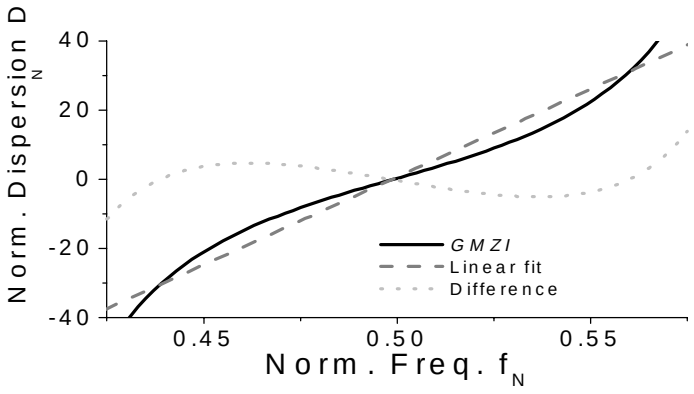


Figure 7.7: The normalized dispersion of the *GMZI* in the passband, a linear fit to the dispersion (dashed line) and the difference between the two (dots).

$\max\{D_N^{Dif}\} \simeq \pm 12$ at the edges of the passband, but also has two local extremes within the passband. To benchmark the size of this dispersion consider an implementation with a $FSR = 100\,\mathrm{GHz}$ at a wavelength of $\lambda = 1550\,\mathrm{nm}$. By using the formulas given in section 2.9 the dispersion parameter at the edges is: $\max\{D\} = \pm 6.3 \cdot 10^2\,\mathrm{ps\,/\,nm}$, which can be compared to that a $10\,Gb/s$ can stand a cumulative dispersion of $\pm 8.0 \cdot 10^2\,\mathrm{ps\,/\,nm}$ before incurring a system penalty on the order of $1\,dB$ [25]. However, since the dispersion varies over the passband and is zero at the passband center it is actually more relevant to consider the dispersion slope. The average dispersion slope is: $\overline{S} = -7.9 \cdot 10^3\,\mathrm{ps\,/\,nm^2}$ and the maximum difference between the *GMZI* and the linear fit $\max\{D^{Dif}\} \simeq \pm 1.5 \cdot 10^2\,\mathrm{ps\,/\,nm}$. A typical dispersion shifted single-mode fiber has a dispersion slope of $S_{fib} \simeq 0.09\,\mathrm{ps\,/(nm^2 \cdot km)}$ [2], whence the average dispersion slope corresponds to a fiber with a length of $L \simeq 8.7 \cdot 10^4\,\mathrm{km}$. Another study ([23]) shows that a filter with zero dispersion in the center of the passband and a linear dispersion slope of $S = 3.4 \cdot 10^4\,\mathrm{ps\,/\,nm}$ gives rise to a system penalty on the order of $2\,dB$ for a $10\,Gb/s$ system. Ignoring the deviation from the linear dispersion slope this shows that a cascade of 4 *GMZI*s should have a dispersion induced penalty on the order of $2\,dB$ (this topic is discussed further in section 7.6). These comparisons show that the dispersion of the *GMZI* is significant whence it is important to reduce it.

The original optimization of the *GMZI* [129] was based on trying to equalize the phase difference between the arms over the passband. It this work it is examined whether the dispersion can be reduced without while maintaining excellent transmission. For this purpose an error function $\varepsilon_x(f_N)$, which depends on both the transmission $T(f_N)$ and the normalized dispersion $D_N(f_N)$, is defined:

$$\varepsilon_x(f_N) = g[T(f_N)] + xh[D_N(f_N)] \tag{7.7}$$

where $x \in R$ is termed the weight factor, and $g$ and $h$ are real valued functions that are increasing with the numerical size of the argument. The error function is increasing with both the loss and the normalized dispersion. Notice that the weight factor determines which error term is dominant, and that $x = 0$ corresponds to the previous optimization. By summing the error function over a discrete set of frequencies $\{f_N^q\}$ covering the passband the total error is found:

$$E_x = \sum\nolimits_q \varepsilon_x(f_N^q) \tag{7.8}$$

For a given weight factor optimizing the *GMZI* amounts to minimizing the total error by varying the all-pass filters pole magnitudes[3]. To minimize the dispersion a large weight factor should be chosen to ensure that the error term from the normalized dispersion is dominating. Accordingly it is chosen so the error from the dispersion is an order of magnitude larger than the error from the transmission. Thus the following pole magnitudes are found: $\rho = [0, 0.194, 0.433, 0.707]$. The new optimization maintains an excellent transmission spectrum with a passband loss of less than 0.06 $dB$ and a crosstalk suppression of more than 32 $dB$, but it has a slightly slower transmission roll-off. The normalized dispersion is again increasing in the passband with a cubic shape although with a smaller amplitude having a maximum dispersion of $\max\{D_N\} \simeq \pm 43$, which is 15% less than from the original optimization. A linear fit to the dispersion in the passband gives an average slope which is 13% lower than the original optimization. Thus the dispersion is reduced, but the remaining dispersion is also substantial. The optimization leading to a smaller dispersion has smaller pole magnitudes than the original optimization. This is in agreement with section 7.2, where it was shown that the maximal dispersion of a single-stage all-pass filter increases with the pole magnitude.

[3] To ensure that the transmission $T$ is less than $-30dB$ over the other passbands an extra error term can be added to the error function. This term is negligible if $T < -30dB$ and extremely large if $T > -30dB$.

All the different optimizations leads to a normalized dispersion with a cubic shape, which is caused by the single-stage all-pass filters being on anti-resonance at the center of the passband and have a $FSR$ equal to the channel spacing. The dispersion shape is related to the ratio between the channel width and the ring $FSR$ and consequently it is to first order independent of $N$, which incurs that an interferometer based $1x2$ $MZI$ with all-pass filters in the interferometer arms will also have a significant dispersion over the passband.

## 7.5 Compensation of the dispersion

To compensate for the dispersion it is necessary to add normalized dispersion, which is zero at the center of the passband and is decreasing over the passband, i.e. to reduce the average slope of the normalized dispersion. As sketched in the previous section it is in theory possible to use a dispersion shifted fiber that has zero dispersion at the center of the passband. However, this would require an enormous amount of fiber ($L \simeq 8.7 \cdot 10^4$ km for a $GMZI$ with $FSR = 100GHz$) and therefore clearly is not a viable solution. Furthermore the main motivation for using planar structures is that it enables integration of several structures on the same wafer. Hence it shall be investigated how to achieve dispersion compensation on the same wafer as the $GMZI$ by using additional nonlinear filters. It is desirable to keep the losses low and, whence the discussion of the additional filters will be restricted to all-pass filters.

A possible solution would be to use multiple-stage all-pass filters in each interferometer arm as it is hereby possible to approximate any phase response [130], [128]. However, it was previously shown that all the channels have the same dispersion. Thus it is possible to compensate them all by placing an all-pass filter with a $FSR$ equal to the channel spacing on the single input arm. This is a simpler solution than placing the filters on the interferometer arms and it has a smaller number of stages. It furthermore has the advantage that by the principle of reciprocity the additional all-pass filter does not change the transmission spectrum of the filter [19]. Notice that the equation for the normalized dispersion (eq. 7.4) is derived for an all-pass filter with a unit delay, whereas the all-pass filters in the $GMZI$ has a delay of $4\Delta T$. Accordingly the filters normalized dispersion with respect to the $GMZI$ is $16D_N$.

To compensate the anti-symmetric dispersion of the $GMZI$ requires that the all-pass filter have opposite anti-symmetry. If a single-stage filter is used to add decreasing normalized dispersion it must be on resonance at the central frequency (i.e. $\phi = 0$), whereas a two-stage filter has rings with equal pole magni-

tude ($\rho_1 = \rho_2$) and opposite phases ($\phi_1 = -\phi_2$). A three-stage filter has one ring on resonance at the central frequency ($\phi_1 = 0$) and the two others have identical pole magnitude ($\rho_2 = \rho_3$) and opposite phases ($\phi_2 = -\phi_3$). The all-pass filters can be optimized by the same routine as in the previous section, where the total error $E_x$ (see eq. 7.7 and 7.8) is minimized by changing the filter coefficients. Fig. 7.8 shows the normalized dispersion of the *GMZI* as well as the normalized dispersion after compensation with optimized single-stage and three-stage all-pass filters, respectively. The two-stage filter is not shown, as it does not improve the performance. The single-stage all-pass filter has: $(\rho, \phi) = (0.093, 0)$, whereas the three-stage filter has: $(\rho, \phi) = [(0.151, 0), (0.179, 1.54), (0.179, -1.54)]$. Fig. 7.8 shows that the single-stage all-pass filter flattens the dispersion at the center of the passband, but that it does not cover the entire passband. This agrees with section 7.2, where it was shown that the width of the decreasing region is smaller than the width of the increasing region. Thus a single-stage filter can maximally decrease the dispersion slope in a band with a width of 50% of the channel spacing, which is smaller than the considered passband (60% of the channel spacing). The three-stage filter gives a very flat profile over the entire passband, with a maximal normalized dispersion of $D_N = 3.0$, which is a factor of 16 less than the value from the original *GMZI*. A linear fit to the dispersion slope gives $\overline{S}_N^C \simeq 1.2$, which is several orders of magnitude smaller than before the compensation. A closer examination shows that the compensated dispersion is rippled with three local maxima and minima in the passband. The full period of the ripple is $\Delta f_N \simeq 0.05$ and the full amplitude is $\Delta D_N = \max D_N - \min D_N \simeq 3$. For a $FSR = 100\,\mathrm{GHz}$ this corresponds to: $\Delta\lambda \simeq 40\,\mathrm{pm}$ and $\Delta\tau \simeq 0.3\,\mathrm{ps}$ leading to a product of $\Delta\lambda\Delta\tau \simeq 10\,\mathrm{ps}\cdot\mathrm{pm}$. In comparison a product of $1700\,\mathrm{ps}\cdot\mathrm{pm}$ has been reported to give a power penalty of 0.5 $dB$ [131].

## 7.6 The dispersion induced power penalty

To further examine the dispersion induced power penalty of the *GMZI DEMUX* a loop transmission simulation was performed (by Christophe Peucheret), using the following settings. The output from a continuous wave laser (average power of 0 $dBm$ and negligible line width) is modulated externally with a pseudo random bit sequence (*PRBS*) signal with a $2^{10} - 1$ word length in a chirp free Mach-Zehnder modulator with an extinction ratio of 30 $dB$. The *PRBS* signal has a bitrate of 10 $Gbit/s$ and a nonreturn-to-zero format with a rise time of 20% of the bit slot. The signal is sent through a cascade of *DEMUX*s

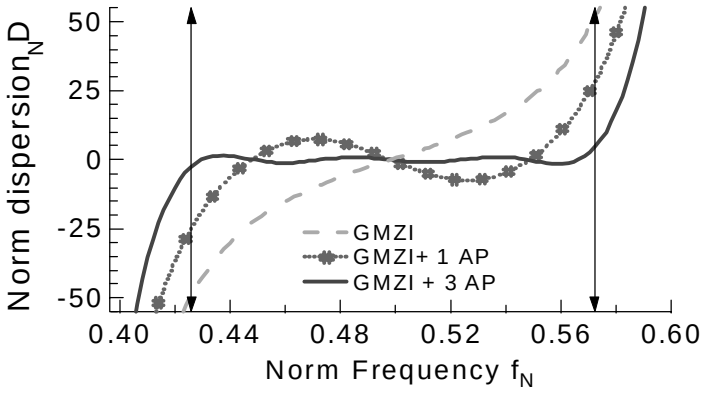


Figure 7.8: The normalized dispersion of the $1x4$ *GMZI DEMUX* with single-stage all-pass filters in the arms before compensation, and after compensation with a single- or a three-stage all-pass filter. The passband is in between the arrowed lines.

and subsequently received in a *PIN* photodiode[4] with a post-detection electrical (fourth order Bessel) filter with a bandwidth of 75% of the bit rate. This gives a back-to-back sensitivity of $-21.7\ dBm$ for a bit-error-rate (*BER*) of $10^{-9}$. Non-idealities in the transfer function of the *DEMUX* induce intersymbol interference and close the received signal eye, which leads to an increase in the *BER*. The power penalty of the *DEMUX* is given as the power increase at the receiver leading to a restoration of the original *BER*. The estimate of the power penalty is based on a Gaussian *BER* evaluation taking intersymbol interference between three consecutive bits into account [132]. To consider a cascade of *DEMUX*s it has been assumed that the individual *DEMUX*s have identical transfer function and detuning of the central frequency from its nominal value. In the following simulations it has been assumed that the *DEMUX* has unit amplitude transfer as the purpose of the simulations is to evaluate the importance of the dispersion. However, the amplitude transfer of the *DEMUX* is very close to unity (section 7.3) and accordingly an inclusion of the correct transmission spectrum only incurs a minor correction.

[4]The *PIN* photodiode has a responsivity of 1.2 $A/W$ and a thermal noise with single-sided density of 15 $pA/Hz^{0.5}$.

Fig. 7.9 shows the simulated dispersion induced power penalty for the *DEMUX* without the compensation filter as a function of the detuning of the central frequency. The figure contains data for 1 and a cascade of 3, 5 and 10 *DEMUX*s as well as the dispersion of a single *DEMUX* with zero detuning. At zero detuning the power penalty is small for a 1 and a cascade of 3, 5 *DEMUX*s, but it increases to 2 *dB* for a cascade of 10 *DEMUX*s. The figure shows that the tolerable detuning decreases with the number of *DEMUX*s. A single *DEMUX* has a 2 *dB* penalty bandwidth of 20 GHz, which decreases to 6 GHz for a cascade of 5 and less than 4 GHz for a cascade of 10 *DEMUX*s. Accordingly dispersion limits the number of *DEMUX*s that can be cascaded before incurring a power penalty, in agreement with section 7.4.

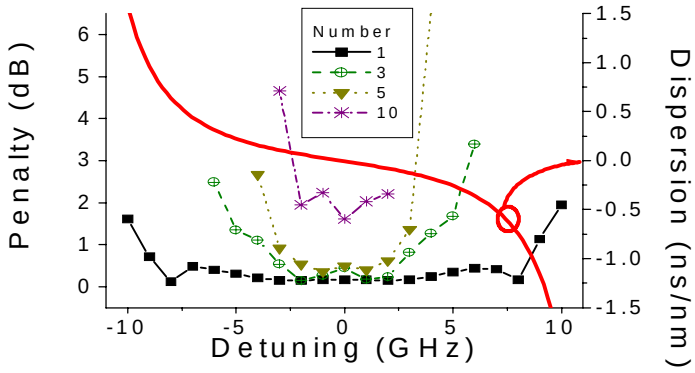


Figure 7.9: The simulated dispersion induced penalty of the *GMZI DEMUX* with optimized all-pass filters as a function of the detuning from the center frequency. Data are shown for a cascade of 1, 3, 5 and 10 demultiplexers.

Fig. 7.10 shows the simulated dispersion induced power penalty for the *DEMUX* with the three-stage all-pass compensation filter as a function of the detuning of the central frequency. The figure contains results for 1 and a cascade of 3, 5 and 10 *DEMUX*s and the dispersion of the dispersion compensated *DEMUX* with zero detuning. At zero detuning the power penalty is below 0.4 *dB* even for a cascade of 10 *DEMUX*s, furthermore the 2 *dB* penalty bandwidth is 10 GHz for a cascade of 5 and 6 GHz for a cascade of 10 *DEMUX*s. Conse-

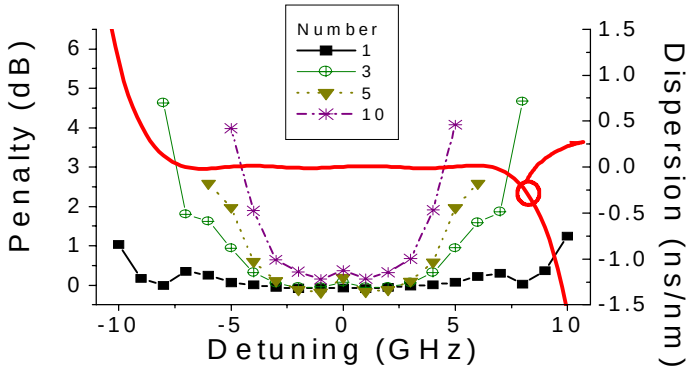


Figure 7.10: The simulated dispersion induced penalty of the *GMZI DEMUX* with optimized all-pass filters and a dispersion compensating filter as a function of the detuning from the center frequency. Data are shown for a cascade of 1, 3, 5 and 10 demultiplexers.

quently the three-stage all-pass compensating filter significantly improves the tolerance for cascading the considered *DEMUX*.

## 7.7 Fabrication of the $1x4$ *GMZI DEMUX*

In the following the feasibility of fabricating the described $1x4$ *GMZI DEMUX* is examined by including non-idealities in the transfer matrices of the individual components (see appendix C), whereafter the new transfer function can be determined. It is assumed that the all-pass filters are realized as ring couplers and that the *GMZI* is fabricated in silica-on-silicon with an index contrast of $\Delta n/n = 2\%$. The $FSR$ of the *GMZI* is chosen as $FSR = 100\,\mathrm{GHz}$, incurring that the ring couplers have $FSR^{AP} = 25\,\mathrm{GHz}$. For a circular ring this is obtained by choosing a radius of $r = 1.32\,\mathrm{mm}$. The total size of the *GMZI* is $50\,\mathrm{mm}\,x\ 20\,\mathrm{mm}$ and if the dispersion compensating three-stage all-pass is included the size becomes approximately $80\,\mathrm{mm}\ x\ 20\,\mathrm{mm}$. Waveguides, ring couplers and *MMI* couplers with this step-index have been produced at Lucent Technologies Bell Labs. The propagation loss of these waveguides have been

measured to be $PL = 0.1\ dB/cm$. By using segmented tapers [48] the coupling loss to standard fiber was reduced to $CpL = 0.4\ dB/facet$. The total loss for a straight waveguide with a length of 80 $mm$ is $L \simeq 1.6\ dB$, whereas the ring loss has been measured to be $L_R = 0.5\ dB$. To achieve flexibility in the design the circular ring coupler can be replaced by the so called race track architecture, which consists of two half circles that are connected by two straight waveguides. Thus the length of the straight can be varied to achieve the desired coupling ratio. Furthermore the simple ring coupler can with advantage be replaced with the more process tolerant asymmetric *MZI* ring coupler with heaters in the interferometer arms [133].Fig. 7.11 shows a mask lay-out of the $1x4$ *GMZI*, where the above described features have been implemented.

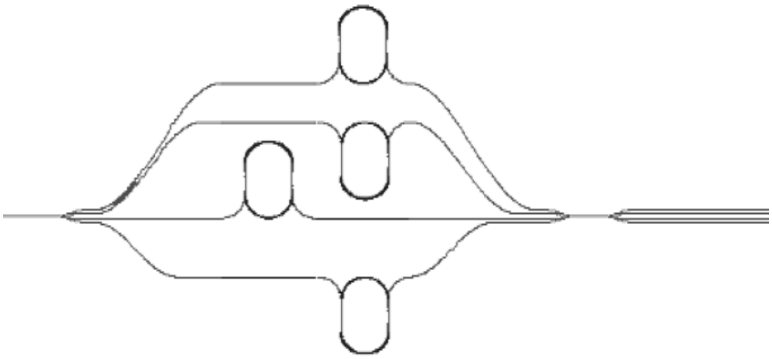

Figure 7.11: Mask lay-out of a $1x4$ *GMZI* router with $FSR = 100\,\mathrm{GHz}$. The $1x4$ splitter is realized as a *MMI* coupler. Phase controlling is achieved by heating the waveguides. The different offsets give the desired delays and the all-pass filters are realised as asymmetric *MZI* couplers.

Using the measured ring loss, the transmission of the *GMZI* was simulated, see fig. 7.12. The figure shows the simulated transmission spectrum of the *GMZI* with and without a loss of 0.5 $dB$ per ring coupler, as well as the transmission of the *GMZI* without the dispersion compensating all-pass filters. The ring loss leads to a loss of 1.9 $dB$ in the passband of which approximately 80% stems from the additional dispersion compensating ring couplers. Fig. 7.4 shows that the dispersion compensated *GMZI* has passband ripple below 0.1 $dB$ and crosstalk suppression above 30 $dB$. With regards to the passband flatness and crosstalk

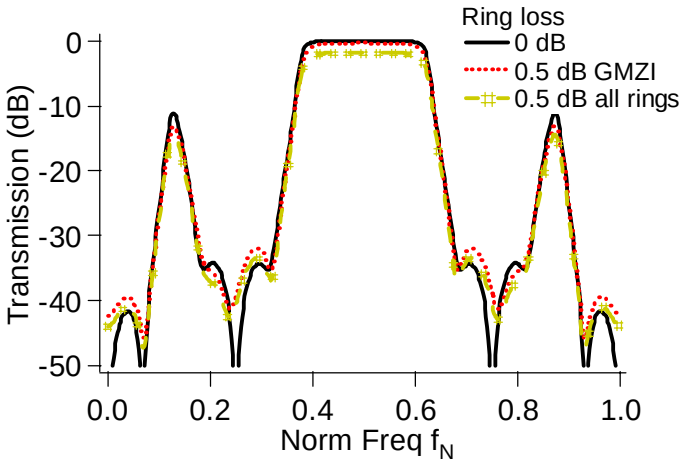


Figure 7.12: Simulated transmission of the *GMZI DEMUX* assuming no ring loss, a ring loss of 0.5 $dB$ in the *GMZI* rings and a loss of 0.5 $dB$ in all the rings.

suppression the dispersion compensating filters improve the performance of the *GMZI*.

The coupling coefficients in the ring couplers are assumed to scale collectively as the ring couplers are placed close to each other on the wafer, i.e.

$$\kappa = (1 + x)\kappa_{ideal} \tag{7.9}$$

where $x << 1$ and $\kappa_{ideal}$ is the calculated coupling coefficient. A calculation shows that the error only has a minor effect on the transmission in the passband, but that they reduce the crosstalk suppression. To maintain a crosstalk suppression of more than 30 $dB$ requires that $|x| < 0.03$, and an error of $|x| = 0.05$ gives a crosstalk suppression of $-26$ $dB$.

A similar analysis shows that a phase error in the interferometer arms of $|\Delta\theta| \simeq 0.1$ $rad$ can be tolerated. This is not a large tolerance, but it should be kept in mind that the phases in the *GMZI* can be measured using low-coherence interferometry [134], and subsequently be compensated by the phase controlling elements. This diminishes the importance of the initial phase errors.

Finally the *MMI* coupler is considered. At Lucent Technologies Bell Labs a number of $1x4$ and $4x4$ *MMI* couplers have been fabricated in silica-on-silicon

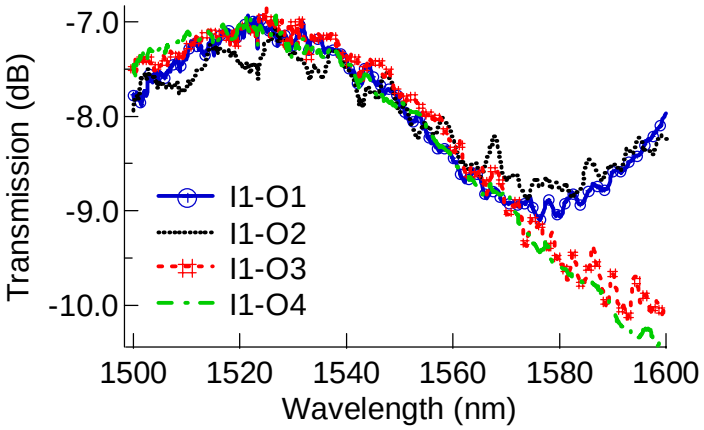


Figure 7.13: Measured transmission spectrum for a $4x4$ *MMI* from input arm 1 (I1) to the 4 different output arms (O1 to O4).

using a design similar to what was described in chapter 5. The transmission spectrum of a fabricated $4x4$ *MMI* coupler is shown on fig. 7.13. The shown *MMI* coupler has a maximum transmission at $\lambda = 1520\,\text{nm}$, where it has an excess loss of 1.3 $dB$. From 1500 nm to approximately 1560 nm the power in the four arms are nearly identical (in contrast to the *MMI* couplers fabricated at *COM*, where an unexpected imbalance was seen, see section 5.2.3). Between 1540 nm and 1570 nm the transmission of all 4 arms decreases while for larger wavelength the power in output arms $O1$ and $O2$ increase, whereas the power in output arm $O3$ and $O4$ decrease.By inserting the measured transfer amplitudes into the transfer matrix and assuming ideal phases the spectral width of the *GMZI* is examined. Fig. 7.14 shows the simulated transmission using the measured *MMI* transmission at 1540 nm.The full line gives the transmission from input arm $I1$ to output arm $O1$, whereas the dotted line shows the transmission from input arm $I1$ to output arm $O3$. The figure shows similar performance for the two arm combinations, although the crosstalk suppression is less for $I1-O3$ than for $I1-O1$, which is caused by slightly different transmission amplitudes. Similar simulations using the measured transmission amplitudes for other wavelength show, that from 1500 nm to 1540 nm the *GMZI* has a passband loss of

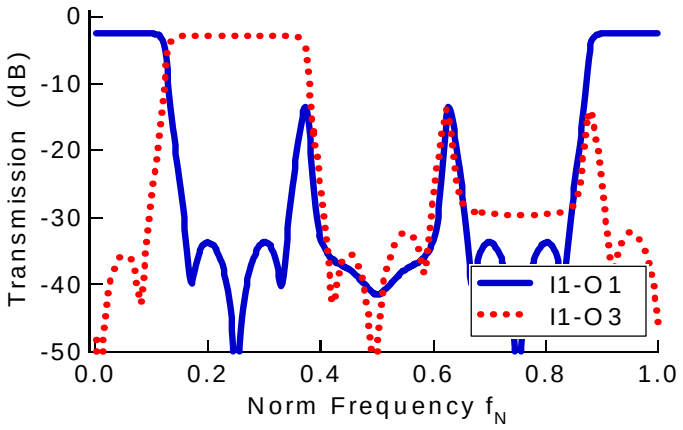


Figure 7.14: Simulated transmission of the *GMZI DEMUX* using the measured MMI transmission at 1540 nm for input arm $I1$ to output arm $O1$ (full line) and output arm $O3$ (dotted line).

less than 3 $dB$ and a crosstalk suppression of more than 26 $dB$. For large wavelengths the cross talk suppression decreases as the difference between the transmission amplitudes increases.

To sum up the fabrication tolerances it has been shown that the measured ring loss of 0.5 $dB$ gives a total loss of 2 $dB$ (of which $80-85\%$ is in the dispersion compensating all-pass filter) and reduces the crosstalk suppression by 1.8 $dB$. A systematic error in the coupling coefficients in the ring couplers of a few percent is tolerable,which seems possible to achieve using the process tolerant asymmetric *MZI* ring coupler with heaters in the interferometer arms [133]. Phase errors should not be a problem since they can be measured and compensated with the phase controlling elements. The measured amplitude spectrum of a $4x4$ *MMI* coupler shows that the *GMZI* has a operating bandwidth on the order of 40 nm. Within these limits the *GMZI* is expected to have a loss of $L_R \simeq 6-7\ dB$ of which 1.6 $dB$ is the loss in a straight waveguide with the same length, 2 $dB$ is the loss from the ring couplers and $2-3\ dB$ is the loss from the *MMI* couplers. The expected passband ripple is approximately 0.1 $dB$ and the crosstalk suppression 25 $dB$.

## 7.8 Summary

In this chapter a $1x4$ generalized Mach-Zehnder interferometer (*GMZI*) based passive optical *MUX/DEMUX* with single-stage all-pass filters in the arms was described. The architecture can also be used as e.g. a $1x2$ or $1x8$ *MUX/DEMUX*, where the difficulty in scaling to a large number of channels stems from that the splitter and combiner should be uniform. The interferometer arms lengths differ by units of a discrete delay, whence the component is an optical filters with discrete delays (see section 2.9). The chapter gave an introduction to $1xN$ passive optical multiplexers for *WDM* networks, followed by a description of optical all-pass filters. Thereafter the working principles of the *GMZI* were sketched and it was shown how the phase difference between the interferometer arms can be flattened around the centers of all the passbands by including all-pass filters in the interferometer arms. Thus the *GMZI* achieves a flat passband with low loss throughout the passband and a crosstalk suppression of more than 30 $dB$, as previously described in the literature [129].

By using a combination of the transfer matrix method and a $Z$-transform the analysis was extended to cover dispersion. It was shown that the transmission and dispersion spectra from the *GMZI* have identical shape for the different output arms, whence it was sufficient to consider a single output arm. Due to the all-pass filters the *GMZI* had a mainly cubic dispersion over the channel passband, which was zero at the center of the passband but had a substantial size near the edges of the passband. For a *GMZI* with a $FSR = 100\,\mathrm{GHz}$ the maximal dispersion over a 60% passband was $\pm 600\,\mathrm{ps\,/\,nm}$. A linear fit gave an average dispersion slope in the passband of $\overline{S} = -7.9 \cdot 10^3\,\mathrm{ps\,/\,nm^2}$, which was compared with that a dispersion slope of $3.4 \cdot 10^4\,\mathrm{ps\,/\,nm^2}$ has been reported to give a significant power penalty [23]. It was therefore relevant to reduce the *DEMUX*s dispersion, while maintaining the excellent transmission spectrum. Hence an error function that increased with both the loss and the dispersion over the passband was defined. Thus the optimization consisted of reducing the error by varying the all-pass filter coefficients. It was found that the maximum dispersion could be reduced by approximately 15% by choosing different all-pass filter coefficients. However, the remaining dispersion was substantial. To accomplish a further reduction it was necessary to use additional non-linear phase filters. Because the dispersion was the same from channel to channel, they could all be compensated with an all-pass filter on the input arm of the $1xN$ *DEMUX*. A single-stage all-pass filter could reduce the maximal dispersion by a factor of two whereas a three-stage all-pass filter could reduce the dispersion by a factor of sixteen. By a loop transmission simulation the dispersion induced power

penalty was estimated. It was confirmed that dispersion limits the number of *DEMUX*s which can be cascaded before incurring a power penalty, especially if the central frequency of the *DEMUX* was slightly detuned from its nominal value. Inclusion of the compensating all-pass filter significantly decreased the power penalty at zero detuning and increased the tolerable detuning of the center frequency. Consequently it gave a considerable improvement for cascading the *GMZI DEMUX*. Finally the fabrication requirements and process tolerances for the *GMZI* multiplexer were evaluated. The transfer function was reevaluated based on measured transfer amplitudes from ring and *MMI* couplers and for straight waveguides. In conclusion it should be possible to construct a $1x4$ *MUX/DEMUX* with $FSR = 100\,\mathrm{GHz}$ having a loss of approximately 6 $dB$, a passband ripple of 0.1 $dB$ and a crosstalk suppression of 25 $dB$ over a operation window of 40 nm.

# Chapter 8

# Model for *UV*-written components

In this chapter an empirical model for the waveguiding properties of directly *UV*-written planar waveguides in silica-on-silicon is developed. Herein the waveguides are described by a rectangular core step-index profile, where the model parameters are found by comparing the measured waveguide width and effective index with modal field simulations. The model is used as input for beam propagation method simulations in order to design *UV*-written optical components, and the model is compared with a measurement of the refractive index profile.

Parts of this chapter has been accepted for publication in *Applied Optics* [135], while other parts have been presented at the conference *Bragg Gratings, Poling, and Photosensitivity 2001* [136].

## 8.1 Introduction

The direct *UV*-writing technique is an alternative fabrication method to the standard cleanroom methods (chapter 3), which can fabricate low loss waveguides with low polarization sensitivity (chapter 4). A drawback of the *UV*-writing technique is that the *UV* induced index change in the core layer occurs by a non-linear process, which is not well understood and accordingly the refractive index profile of the waveguides is unknown. Until now, simple components such as couplers and splitters have been developed using an iterative procedure

to optimize the component performance [137], [138], [139]. However, this approach is not feasible for constructing more complicated components. It thus becomes necessary to numerically model the waveguiding properties of directly $UV$-written waveguides and to establish experimental methods for extracting model parameters. Accordingly a numerically model of the waveguiding properties of directly UV-written waveguides is needed. The success criterium for the model is whether it can achieve sufficient accuracy to be usable for lay-out of UV-written waveguide components. To quantify this requirement the predictions of the model for simple test structures should be within 10% from the measured values.

Prior to this work Maxwell et. al. have used UV written directional couplers to give an estimate of the UV induced refractive index change [137]. The method used there, however, was based on adjusting the index step to fit a measured spectral response and was not validated by further experiments.

## 8.2 Constructing the model

To describe the waveguiding properties a rectangular core step-index profile is chosen, so that a width, $W$, and a step-index, $\Delta n$ (relative to the unexposed core), describe each waveguide. In prior work it has been suggested that the index change decays exponentially in the vertical direction due to strong $UV$ absorption [52]. It is also reasonable to assume that the index distribution in the horizontal direction can be approximated by a Gaussian function, since this is the form of the $UV$-writing beam. However, such subtleties of the index distribution can only be determined using dedicated and complex setups [41].

In this chapter it is investigated whether an equivalent step-index profile extracted from simple measurements can be used to accurately describe the waveguiding properties. Hence, the square index profile is chosen because it is of the simplest possible form for a planar waveguide, not because it is anticipated that it describes the actual index distribution.

It was shown in section 4.2 that it is possible to assign a width to a UV-written waveguide by taking an optical picture of it. The measured width is roughly a factor of two larger than the spot size of the laser at the sample and decaying with the scan velocity (see fig. 4.5). This indicates that the index change process is saturated in the centre of the beam, and that the refractive index does not have a step-index profile. Accordingly it is not a priori clear how the assigned width relates to the actual index distribution of the waveguide. However, it is assumed that within a scaling factor $x$ this width describes the

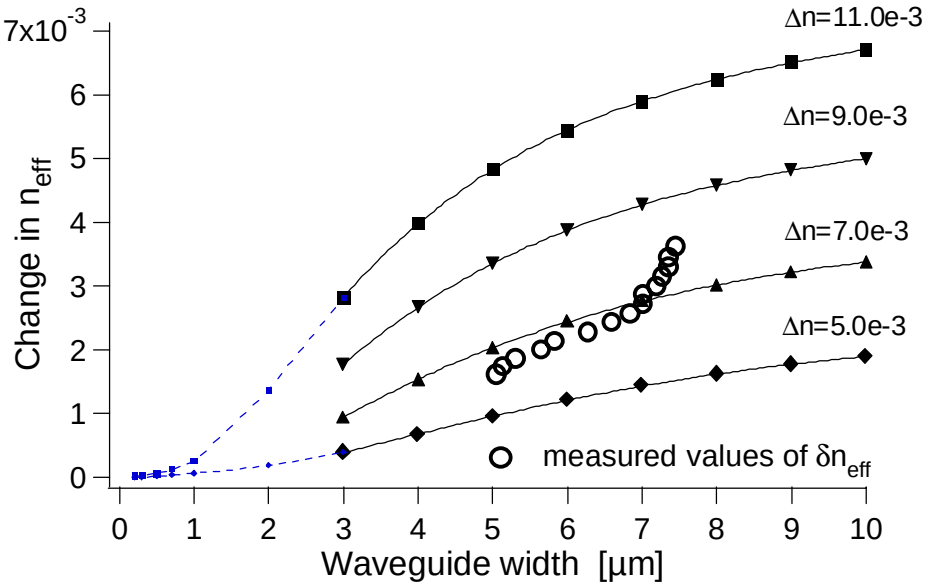


Figure 8.1: The simulated change in effective index as a function of the width for a step-index of 0.004 (diamonds), 0.006 (triangles), 0.008 (circles) and 0.010 (squares). The figure also shows the measured change in effective index as a function of the width (open circles), for a width scaling factor of $x = 1.0$. The left side of the figure contains simulations for small waveguide widths, which are used to find the convergence value of the effective index.

characteristic width of the waveguides, i.e. that the form of the index distribution remains fairly constant within the sampled range of scan velocities. The scaling factor is a free parameter in the model, representing the fact that the actual index profile may not be rectangular.

The effective index of the waveguides was measured as described in section 4.3. It was found that the effective index decreases with the scan velocity (see fig. 4.8). The effective index converges towards that of the slab structure when the waveguide becomes weak, and this convergence value was estimated by inducing progressively weaker waveguides (using low power of the $UV$-writing beam and high scan velocities).

To relate the measured width and effective index to an equivalent step-index the finite difference method is used. Simulations are performed for rectangular core waveguides having a width ranging from $3.0\,\mu$m to $13.0\,\mu$m and a step-index ranging from 0.003 to 0.011. For a waveguide surrounded by a buffer with uniform index the effective index converges to the index of the background in the limit of a vanishing waveguide. However for our waveguides the index of the buffer is slightly higher than that of the topcladding (see chapter 4) thus the convergence value is found by simulating waveguides with very small width. The thickness and index of each glass layer used in these simulations is equal to those of the sample and fixed boundary conditions are used.

Fig. 8.1 shows the simulated change in effective index (from that of the slab structure) as a function of the width for various step-index values. As expected, the change in effective index grows with the width of the waveguide and the step-index. Fig. 8.1 also shows the measured change in effective index as a function of the waveguide width (using $x = 1.0$). By comparison with the simulated curves it is seen that for small widths the equivalent step-index of the $UV$-written waveguides is approximately 0.006, whereas for large widths it is close to 0.008. Accordingly the equivalent step-index is at least a factor of six larger than the unintended asymmetry in refractive indices of the stack layers. This explains why the asymmetry does not prevent the realization of low loss $UV$-written waveguides. Using fitted polynomials to interpolate between the simulated curves the equivalent step-index is obtained numerically for each waveguide. As previously mentioned the scaling factor $x$ between the measured width and the characteristic width that results in the most accurate $BPM$ modeling, is treated as a free parameter. Accordingly, the equivalent step-index is extracted using various scaling factors, chosen to be $x = 0.8$, 1.0 and 1.2.

Fig. 8.2 shows the resulting equivalent step-index values as a function of the scan velocity. When the scaling factor increases (i.e. wider waveguides) the equivalent step-index decreases in order to result in the same effective index.

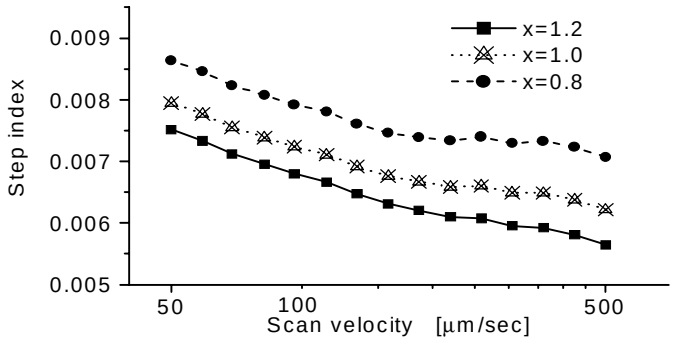


Figure 8.2: The derived equivalent step index for $UV$-written waveguides as a function of the applied scan velocity for a width scaling factor of $x = 0.8$ (circles), $x = 1.0$ (triangles) and $x = 1.2$ (squares).

In addition it is seen that the step-index decreases with the scan velocity, as expected when the index change increases with the time of $UV$ exposure. For a scaling factor of $x = 0.8$ the index step has a small bump for high scan velocities, which is contrary to this expectation. This may be an indication that a scaling factor of $x = 0.8$ does not yield a reasonable description of the waveguides.

## 8.3 Validation of the model

Before the step-index values derived for $UV$-written waveguides above can be given any credit the validity of the measurement technique must be tested. The first test is to apply the parameter extraction technique to a standard cleanroom fabricated sample with a known index step. In a second test the initial motivation for developing the technique is followed, namely to achieve a desired device performance in a single iteration by applying $BPM$ simulations to accurately predict the waveguide layout and subsequently the simulated and measured wavelength dependency is examined. Finally the extracted model is compared to direct measurements of the refractive index profile.

### 8.3.1 Reproducing the step-index of standard cleanroom fabricated waveguides

It was previously shown that standard cleanroom fabricated waveguides can be described as step-index rectangular cores (see chapter 3). The sample used for this test has a step-index value of $\Delta n = 0.0081 \pm 0.0003$, a core height of $H = 6.1\,\mu$m and widths ranging from 5.0 to 13.0$\,\mu$m. The waveguide widths and effective indices of this sample has been measured using the techniques described in chapter 4 and a numerical step-index model was extracted using finite difference simulations based on actual sample data. Since these waveguides are expected to have a rectangular index profile it was chosen not to use a free scaling parameter for the width measurements. By comparing the simulated and measured effective index the step-index value was extracted for each waveguide. The result is shown in fig. 8.3. The figure shows that the step-index

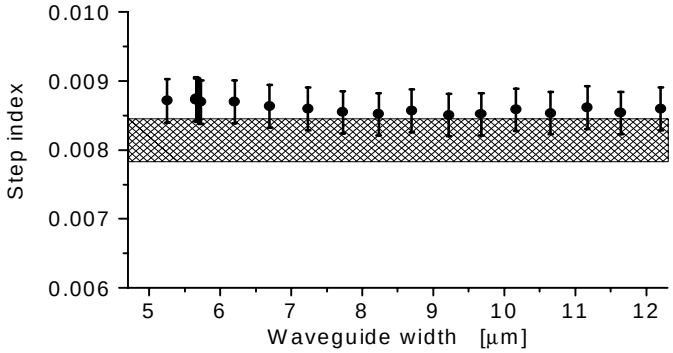


Figure 8.3: The equivalent step index derived for standard waveguides as a function of their width. The size of the error bars is mainly given by the uncertainty of the core layer height. Aso shows is the step index value interval stated by the manufacturer as a cross hatched area.

is independent of the waveguide width, with an average value of $0.0086 \pm 0.0003$. The slight systematic deviation from the expected value is comparable to the uncertainty following from the precision with which the core layer thickness is known. Hence, this test shows that it is possible to reproduce the step-index

value of cleanroom fabricated waveguides.

### 8.3.2 Prediction the coupling of directional couplers

In the next test the model of $UV$-written waveguides is used to achieve a desired directional coupler performance in a single iteration using $BPM$ simulations to predict the appropriate waveguide layout. Directional couplers are chosen as a test component, as they are widely used as building blocks in integrated silica-on-silicon devices as e.g. optical switches and gain equalizers [7]. Furthermore, the coupling length of directional couplers depends critically on the evanescent tail of the modal fields inside the coupling region as mode fields depend strongly upon the waveguide properties. The couplers are written so that the dual input/output waveguides have a separation of $80\,\mu$m, while the waveguides are connected to the central coupling region by circular arc $S$-bends with a radius of 24 mm. The length of the central coupling region $L_{st}$ will be either 10 mm or 20 mm.

The design goal is to obtain full cross coupling of the power at $\lambda = 1557$ nm (with a coupling strength of $\phi = \pi$), which is achieved by varying the center-to-center spacing $Sep$ of the waveguides in the coupling region. The applied scan speed is $v_{sc} = 120\,\mu\mathrm{m}/s$. To predict which center-to-center spacing yields full cross coupling for the two lengths a $3D$ $BPM$ with a finite difference mode solver is used. The actual geometry of the coupler is used in the simulation and accordingly the coupling in the bends is automatically included. $BPM$ simulations are performed for scaling factors of 0.8, 1.0 and 1.2, indicating that for a length of $L_{st} = 10$ mm the center-to-center spacing should be $14.1/14.8/15.6\,\mu$m for scaling factors of $x = 0.8/1.0/1.2$, respectively. Accordingly couplers with length $L_{st} = 10$ mm and center-to-center separation of $14.0\,\mu$m and $15.4\,\mu$m are fabricated. Based on similar simulations for a length of $L_{st} = 20$ mm it was chosen to fabricate couplers with a spacing between $15.4\,\mu$m and $16.8\,\mu$m. Note that the range of separations chosen here is much narrower than would normally be applied during a first iteration, illustrating the potential of the technique for reducing the device development time. The couplers are evaluated as described in section 3.5 by measuring the transmitted power in the two output arms at $\lambda = 1557$ nm using $TM$ polarization[1]. The coupler excess loss is roughly 0.3 $dB$ with respect to a 30 mm long straight reference waveguide, which itself has an insertion loss of 0.8 $dB$. The measured cross coupling, defined as the fraction of

[1] The polarization dependency of the $UV$- written waveguides is quite low and thus the corresponding data for the $TE$ polarization does not differ significantly (see chapter 4).

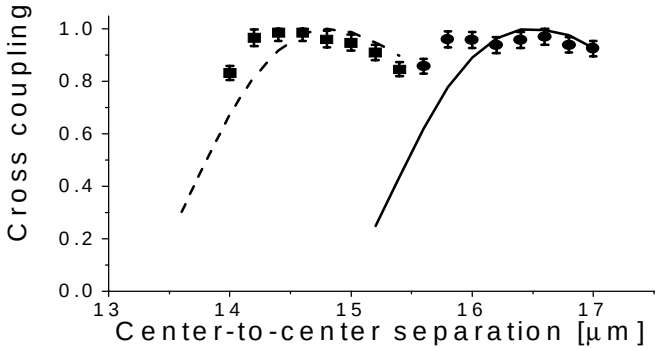


Figure 8.4: The measured (symbols) and simulated (curves) cross coupling for $UV$-written directional couplers. The width scaling factor used in the simulations is $x = 1.0$. The length of the central coupling region is 10 mm (left side of the graph) and 20 mm (right side of the graph).

transmitted, cross-coupled power, is independent of which input arm is excited. The measured cross coupling is close to unity along the sampled range of both series. This is in good agreement with the $BPM$ predictions for a scaling factor of $x = 1.0$, as shown in fig. 8.4. The uncertainty of the measured power is $\pm 0.1\ dB$, giving rise to the error bars shown in the figure. The measured and simulated cross coupling are similar over the entire range, but this is partly due to that the cross coupling has a maximum in the range, and similar curves close to 50% coupling would therefore give larger deviations. However, a numerical investigation shows that the center-to-center values giving a fixed cross coupling ratio to first order is independent of the size of that coupling ratio (see appendix C). Thus the measured center-to-center spacing for which the maximum cross coupling is achieved is compared with the simulations. The measured values are approximately $Sep = 15.8\,\mu$m and $16.4\,\mu$m for a coupling region length of $L_{st} = 10$ mm and 20 mm, respectively. These values are only 3% less than the predictions of the $x = 1.0$ model. From the figure it is evident that a small systematical error may persist since the simulated curves peak at a slightly larger spacing, which indicates that the simulated coupling coefficient is slightly larger than the measured coupling coefficient. The $BPM$ simulations show that this

difference may be due to the core layer actually being 6% thicker than stated value (i.e. around the upper end of the thickness uncertainty window). Another reason for the discrepancy could be that a scaling factor slightly different from $x = 1.0$ should be used, but since the error is comparable to that arising from the core layer uncertainty, it is not possible to make a firm conclusion on this point. In the remaining part of this chapter the scaling factor is set to unity.

### Wavelength dependency of the couplers

Furthermore the wavelength dependency of the couplers is found by using a polarized *ASE* source. Fig. 8.5 shows two examples of these measurements as compared with *3D BPM* simulations using the scaling factor of $x = 1.0$, which was previously found to be appropriate. Fig. 8.5*A* shows the measured and simulated (*3D BPM*) cross coupling for a coupler with coupling region length $L_{st} = 10\,\text{mm}$ and center-to-center separation $Sep = 14.4\,\mu\text{m}$, whereas fig. 8.5*B* is for a coupler with $L_{st} = 20\,\text{mm}$ and $Sep = 16.0\,\mu\text{m}$. The figure shows that

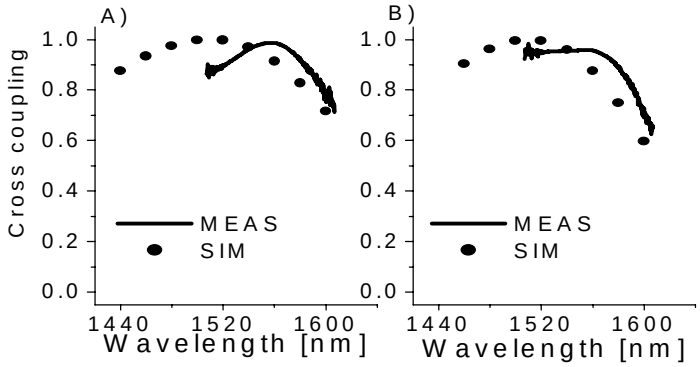


Figure 8.5: The measured and simulated (*3D BPM*) cross coupling of *UV*-written directional couplers as a function of the wavelength. *A*) Coupling region length $L_{st} = 10\,\text{mm}$ and center-to-center separation $Sep = 14.4\,\mu\text{m}$ and *B*) $L_{st} = 20\,\text{mm}$ and $Sep = 16.0\,\mu\text{m}$.

in general the measured and simulated curve have similar shape, although the measured curve is not quite as flat as the simulated curve. Furthermore the

simulated wavelength of maximal cross coupling is smaller than its measured counterpart. Since the coupling coefficient increases with the wavelength this indicates that the simulated coupling coefficient is larger than the measured coupling coefficient, which is in agreement with fig. 8.4. The difference between the wavelengths giving maximum cross coupling is largest for the couplers where the discrepancy between the measured and simulated curve on fig. 8.4 is large, but is in all cases less than 4%. Thus these measurements corroborate the model within the given uncertainties.

### 8.3.3 Comparison with a measurement of the refractive index profile

As another test the refractive index profile was measured using commercially available equipment (OWA-9500 from EXFO Electro-Optical Engineering Inc.). According to its specifications, the OWA-9500 has a spatial resolution of $\leq$ 0.6 $\mu$m in the horizontal (i.e. across the width of the waveguide) and $\leq 0.5\,\mu$m in the transverse direction, whereas the absolute refractive index resolution is $\leq 7 \cdot 10^{-5}$ [42].

Fig. 8.6 shows the measured horizontal (fig. 8.6*A*) and vertical (fig. 8.6*B*) refractive index profile through the center of a waveguide written with a scan velocity of $v_{scan} = 85\,\mu\text{m}\,/\,\text{sec}$ and the extracted step-index profile from the model with a scaling factors of $x = 1.0$. The vertical cross section also contains the background profile obtained outside the waveguide, which is seen to be non-uniform. Fig. 8.6*A* shows that the horizontal profile resembles the extracted step-index profile, although it has a slightly higher step-index. The measured profile has a plateau with a value of $\Delta n = 0.0084$ and a full-width at half maximum ($FWHM$) of 7.6 $\mu$m. This can be compared with that the extracted model (for $x = 1.0$) has a step-index of $\Delta n = 0.0074$ and a width of $W = 7.2\,\mu$m.

Fig. 8.6*B* shows the vertical index profile through the center of the core, where the height increases from left to right. The profile also has a plateau, but with a peak close to the intersection between the core layer and the topcladding. The peak gives a increase of $3 \cdot 10^{-3}$ compared to the index of the plateau and a $FWHM$ of 1.1 $\mu$m. However, a measurement of the vertical profile of the background (obtained outside the core) shows a similar peak. This suggests that the peak is caused by a non-uniform concentration of germanium, boron and phosphor throughout the core, caused by diffusion during the anneal of the wafer. This was subsequently confirmed by a secondary ion mass spectroscopy measurement (performed by Peter Carøe Nielsen), which showed germanium diffusion from the core-layer to the topcladding and phosphor diffusion from

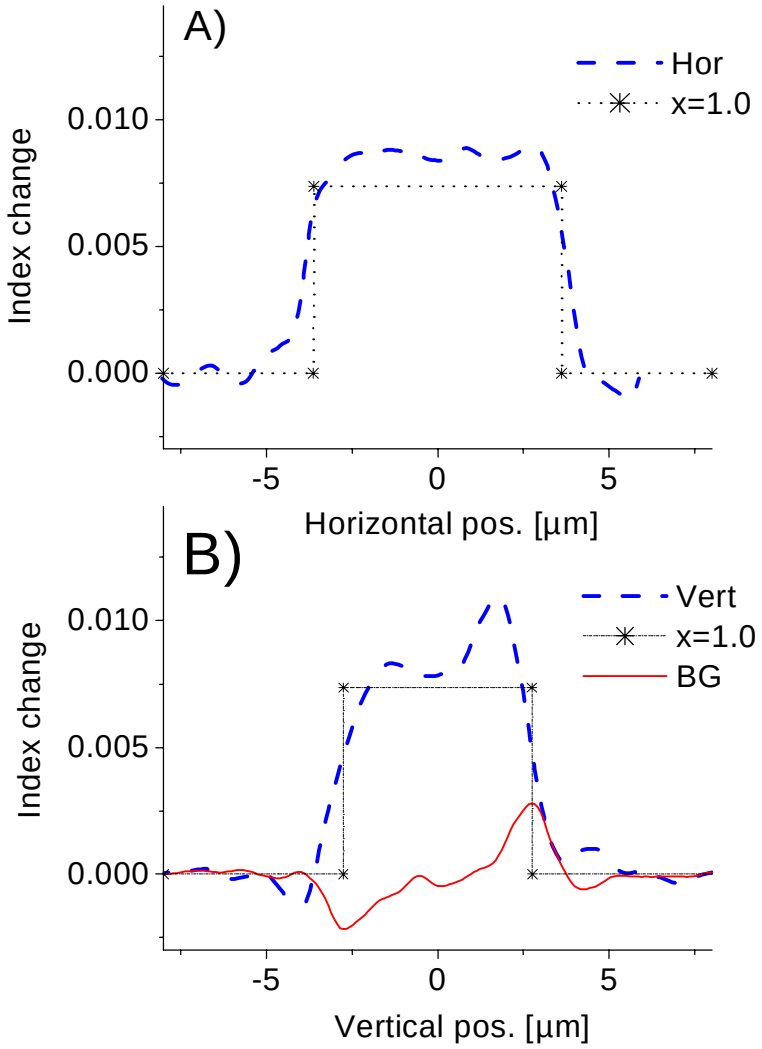


Figure 8.6: The measured horizontal ($A$) and vertical ($B$) index profile through the center of a $UV$-written waveguide, fabricated with a scan velocity of $v_{scan} = 85\,\mu\mathrm{m}\,/\,\mathrm{s}$ (as dashed lines). Also shown is the extracted step-index profiles from the developed model with a scaling factor of $x = 1.0$ (dotted line with sparse markers), and the vertical profile of the background (full line). The non-uniform background is caused by diffusion during the anneal of the wafer.

the topcladding to the core layer[2].

Despite the above described discrepancies, fig. 8.6 in general shows excellent agreement between the measured and extracted curves, which is clear corroboration of the model.

## 8.4 Summary

In this chapter an empirical method for deriving the waveguiding properties of directly *UV*-written waveguides was presented. Based on measurements of a waveguide width and the effective index using optical microscopy and weak Bragg gratings, respectively, a step-index value for an equivalent, rectangular core waveguide is obtained by comparison with mode field simulations. It was not expected that the real index profile has a rectangular shape. Thus the measured width might not be appropriate to describe the waveguide and hence a width scaling factor was introduced. It was found that the equivalent step-index of the *UV*-written waveguides decreases with the scan velocities, but is on the order of $\Delta n \simeq 0.007$ for a scan velocity of $200\,\mu\mathrm{m}\,/\,\mathrm{s}$. The success criterium for the model is whether it can achieve sufficient accuracy to be usable for layout of UV-written waveguide components. To quantify this requirement the predictions of the model for simple test structures should be within 10% from the measured values.

To validate this method the step-index of a set of standard cleanroom fabricated waveguides was reproduced. The derived value differed by 6% from the expected value, which was comparable to the experimental uncertainty. Furthermore, the model data for *UV*-written waveguides were used as input for *BPM* simulations to predict the layout parameters of directional couplers for a given set of design and performance requirements. Subsequent fabrication showed that within the measurement uncertainty the appropriate width scaling factor is unity. Using this model better than 5% agreement with the *BPM* simulations was obtained, both with respect to the center-to-center separation giving full cross coupling and with the wavelength dependency of the cross coupling. Finally the extracted model was compared with a direct measurement of the refractive index profile. The measurement showed that the sample has a non-uniform vertical refractive index profile, which could be explained by diffusion of germanium and phosphor during the anneal. Except for this deviation the

[2] A measurement for a supposedly similar wafer, shows significantly less diffusion. This indicates that by mistake the considered sample has been annealed with a too high temperature or that it does not have a barrier-layer between the core and the topcladding (see section 3.2).

measurements was in excellent agreement with the extracted profile form the model, which corroborates it. The model makes it possible to employ detailed numerical modeling to reduce the number of experimental iterations required for development of $UV$-written optical devices.

# Chapter 9

# Conclusion

During my Ph.D. project I have worked on a number of projects concerning silica-on-silicon components for optical communications, where special emphasis has been on optical couplers and how they can be used as building blocks for devices with a larger complexity. I have mainly been engaged in design, modelling and layout of the components, but have also characterized the components and participated in post processing experiments.

In the following some of the main conclusions of the work are summarized.

**Directional couplers**: In general there was good agreement between the measurements and simulations for directional couplers, and the measured transfer functions have the same functional form as their simulated counterparts. It was possible to reach the desired goals of a wavelength-flattened 3 $dB$ coupler with an imbalance of less than 0.2 $dB$ from $\lambda = 1500\,\mathrm{nm}$ to $1600\,\mathrm{nm}$, although this particular coupler is very process sensitive. However, a qualitative analysis showed that there is not complete agreement between $3D$ $BPM$ simulations and the measurements, and that it is not possible to reach agreement by varying the waveguide height, width or step-index. It was therefore concluded that the rectangular step-index model is not an adequate description of the waveguides.

**Multi mode interference couplers** were investigated in parallel with the directional couplers. Simulations showed that multi mode interference couplers have better process tolerance than directional couplers, but our measurements for 3 $dB$ couplers showed an unexpected imbalance of 0.6 $dB$ and a large polarization sensitivity of more than 1 $dB$. By inscribing a Bragg grating into very wide straight waveguides it was found that they have a very large birefringence, which is not induced by the geometrical shape. Furthermore simulations

showed that the imbalance of multi mode interference couplers is very sensitive towards an error in the rectangular step-index profile, where the measured deviation can be explained by a index step that is 0.6% lower at the edge than in the center of the multi mode slab. This effect was corroborated experimentally by ultraviolet-trimming of the multi mode interference couplers to remove the imbalance. In contrast hereto similar multi mode couplers (obtained from the original design by scaling) fabricated at Lucent Technologies Bell Labs did not show these effects, and it must be inferred that the processing technology at *COM* leaves room for improvement. In any case these observations showed that the process tolerance of multi mode interference couplers is not as good as what has previously been assumed.

**Pump-signal** 980/1550 nm **multiplexer**: Several architectures have been considered for pump/signal multiplexers for erbium doped amplifying waveguides. It was shown that a directional coupler can be used as a multiplexer with a measured pump loss of less than 0.2 $dB$ and a passband with a $-0.2$ $dB$ bandwidth of more than 80 nm. A multi mode interference coupler is not well suited as a multiplexer as it has a minimum excess loss of approximately $0.2 - 0.3$ $dB$ and furthermore simulations show that it has inferior wavelength-flatness compared to the directional coupler. Finally a new architecture consisting of a point-symmetric Mach-Zehnder interferometer of two uniform asymmetric couplers was presented. Simulations showed that it has a pump loss of less than 0.2 $dB$ and an extremely flat signal spectrum with a $-0.2$ $dB$ bandwidth of approximately 200 nm. Taking realistic waveguide parameter deviations into account it maintained a signal loss of less than 0.1 $dB$ from 1500 nm to 1600 nm. Accordingly it has better process tolerance than the directional coupler. However, this architecture has not been fabricated yet, so these conclusions still remain to be confirmed experimentally.

**Interferometer based demultiplexer using all-pass filters**: During a period as visiting scientist at Lucent Technologies Bell Labs I mainly worked on refining an architecture for multiplexing/demultiplexing a small number of channels. The architecture consists of a $1xN$ generalized interferometer with single-stage all-pass filters in the interferometer arms, where the splitter and combiner can be realized as multi mode interference couplers and the all-pass filters as a ring resonator coupled to a waveguide. This limits the architecture to small $N$ as 2, 4 or 8. The all-pass filters introduce a non-linear phase dependency that can be optimized to give the router a flat passband with a loss of less than 0.1 $dB$ over 60% of the channel spacing and a crosstalk suppression ratio in excess of 30 $dB$. However, my analysis showed that the all-pass filter also introduce a cubic dispersion, which is significant close to the edge of the

passband. Accordingly the dispersion limits the number of routers that can be cascaded before incurring a power penalty. It was shown that the dispersion is inherent to the considered architecture and can only be removed by using additional non-linear phase filters. The best solution is to add an all-pass filter to the single input arm as this removes the dispersion of all the outputs. A single-stage all-pass filter reduced the dispersion over the passband by a factor of 2 while a three-stage filter reduced it by a factor of 16. By a loop transmission simulation it was shown that the compensating filter significantly increased the tolerance for cascading several multiplexers, as it gave a lower power penalty at zero detuning of the central frequency and increased the tolerable detuning. Finally a numerical analysis based on experimental data (for ring and multi mode interference couplers and straight waveguides) showed that the fabrication tolerances for the router are reasonable.

**Ultraviolet-written components:** An equivalent step-index model for ultraviolet-written waveguides was constructed by comparing measurements of the waveguide width and the refractive index of the waveguides with simulation data for a rectangular step-index core. It was shown that the used technique can correctly reproduce the waveguide width and step-index for standard cleanroom fabricated waveguides. Furthermore the model was used to predict an appropriate design for realizing a uniform symmetrical coupler with 100% cross coupling, and subsequent measurements reproduced the simulation result to within 5% for both the center-to-center spacing resulting in 100% cross coupling and the wavelength of maximum cross coupling. Finally a comparison between the extracted model and the refractive index profile showed good agreement. Accordingly it was concluded that the model can be used for designing ultraviolet-written waveguides with a more complicated functionality. This will reduce the number of experimental iterations needed to develop such components. However, it is also possible to fabricate more complicated components using standard cleanroom waveguides, and it still remains to be seen whether the ultraviolet writing technique can surpass the standard technique in either price or performance of the components.

## 9.1 Recommendations for future work

As shown in the above summary we, at *COM,* face a number of challenges in fabricating complex integrated optical components. In the following section I shall try to give some recommendations for possible future work.

The measurements presented in this work show that the fabricated waveg-

uides can not be described by a step-index model. It is therefore relevant to further investigate the refractive index profile to see whether it depends on height, mask width or step-index, e.g. by directs measurements of the refractive index profile or by secondary ion mass spectroscopy. It must be emphasized that it is not necessarily critical to have a uniform index profile for the waveguides. However, it is critical that the profile is constant over the wafer and from wafer to wafer. Accordingly it is necessary to further examine the effect of process variations on component performance. This can be done numerically, but a numerical analysis can not stand alone and must be accompanied by experiments on the actual structure which is investigated. To facilitate such an analysis it is advantageous to include optical test structures on the mask with a known functionality, as characterization of these components will reveal, whether the fabricated wafer deviates from the expected performance.

Another issue is the unexpected large birefringence for wide waveguides and the problems with fabricating multi mode interference couplers. A comparison with components fabricated at Lucent Technologies Bell Labs show that the fabrication process at *COM* needs further optimization. In particular the role of diffusion during the anneal and non uniform stress in the waveguides should be clarified. Furthermore, the polarization sensitivity of the components have only been briefly touched upon, although very low polarization dependent loss is a necessity for optical components to have any commercial value. Hence this topic should be treated in further detail.

With regards to the ultraviolet-written waveguides it could be investigated how to decrease the propagation loss, e.g. by encapsulating the sample in a vacuum chamber during the ultraviolet-writing process. To increase the design flexibility it would furthermore by useful to increase the maximum obtainable index change. A possible method would be to increase the deuterium concentration in the wafer through deuterium loading at a higher pressure.

# Appendix A

# Accuracy of the numerical methods

The purpose of this appendix is to compare different simulation methods used in this work. The effective index method *(EIM)* and the finite difference *(FD)* method are compared and hereafter the $2D$ and $3D$ *BPM,* that rely on each of these mode solvers, are compared.

All the following simulations are conducted for step-index waveguides with $\Delta n = 0.010$, *TE* polarization and a uniform buffer around the core with an index $n_{buf}$ given from the Sellmeier formula for silica. Unless something else is stated the wavelength is: $\lambda = 1.550\,\mu$m. The settings used are a compromise between accuracy and speed.

## A.1 *EIM-x* versus *FD* method

The following simulations are for a rectangular step-index waveguide with width $W$ and height $H$. The calculation window is rectangular and has a width $CWW$ and height $CWH$ that are both large compared to the field dimensions. A standard single mode waveguide has dimensions on the order of $5\,\mu$m for the chosen index step, whereby a calculation window size of $30\,\mu\text{m}\,x30\,\mu$m is appropriate. The calculation window is discretized using a step size of $0.2\,\mu$m and fixed boundary conditions are used.

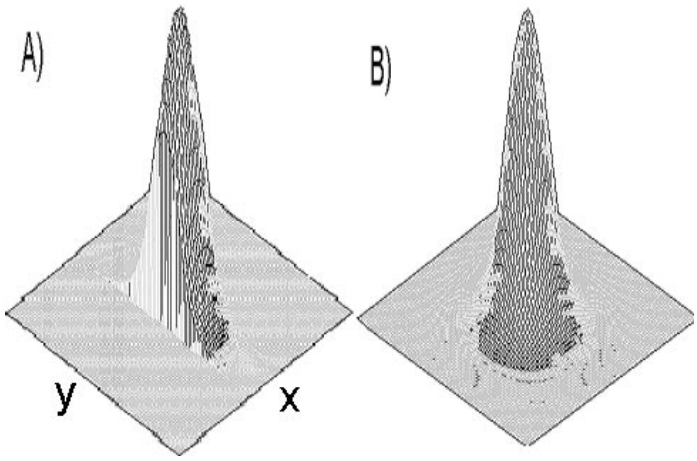


Figure A.1: The intensity of the modal field of a step-index waveguide from $A$) the effective index method ($EIM$-$x$) and $B$) the finite difference ($FD$) method.

### A.1.1 One isolated step-index waveguide

Fig. A.1 shows the intensity of the modal field of the zero order mode of a step-index waveguide with $W = H = 5.5\,\mu$m. Fig. A.1$A$ shows the result of a $EIM$-$x$ simulation, whereas fig. A.1$B$ shows the result of a finite difference simulation. In both cases the field reaches its maximum at the center of the core. It decays monotonically from this maximum and is close to zero at the edge of the calculation window. The simulated field is symmetrical in the $FD$ simulation, but not in the $EIM$-$x$ simulation. Here the field is cut-off at the edge of the core in the $x$-direction, which clearly is not an accurate description of the field.

To make a quantitative comparison the effective index of the core $n_{eff}$ can be used. Define the ratio $R$ of the effective indices by:

$$R \equiv \frac{n_{eff}(EIM) - n_{eff}(FD)}{n_{eff}(EIM)} \tag{A.1}$$

where $n_{eff}(EIM)$ and $n_{eff}(FD)$ are the values of the effective index obtained with from the $EIM$-$x$ and $FD$ simulation, respectively. For the performed simulations the ratio is less than $10^{-3}$, which indicates excellent agreement. However,

in either case the effective index is bounded by: $n_{buf} < n_{eff} < n_{buf} + \Delta n$. Accordingly it is a better test of the accuracy to take the ratio after subtraction of the index of the buffer, whence the deviation ratio $DR$ is defined as:

$$DR \equiv \frac{(n_{eff}(EIM) - n_{buf}) - (n_{eff}(FD) - n_{buf})}{n_{eff}(EIM) - n_{buf}} \quad (A.2)$$

$$= \frac{n_{eff}(EIM) - n_{eff}(FD)}{n_{eff}(EIM) - n_{buf}} \quad (A.3)$$

The simulated deviation ratio as a function of the ratio between the width and the height $W/H$ is shown on double logarithmic plot on fig. A.2. The figure shows that the deviation ratio in general is positive meaning that the value from the *EIM-x* is higher than from the *FD* method. The deviation ratio decreases with the value of $W/H$. For a ratio $W/H < 0.3$ the deviation ratio is larger than unity $DR > 1$, whereby the *EIM-x* is not suited for describing such a waveguide. A square core $W/H = 1$ gives a deviation ratio of $DR = 0.08$, which is also a substantial error. For the multi mode interference (*MMI*) couplers used in this work the ratio between the width and height is $W/H = 40/5.5 \simeq 7$ for which the deviation ratio is $DR \simeq 5 \cdot 10^{-4}$. Accordingly the *EIM-x* is very accurate for the effective index of the zero order mode in a *MMI* slab.

It should be mentioned that if the *FD* method were compared with the *EIM-y* method then the resulting deviation ratio would instead increase with the ratio of $H/W$ and be a good description for very high thin cores.

### A.1.2 Two coupled step-index waveguides

Hereafter the two methods are compared for a structure consisting of two rectangular step-index waveguides. The waveguides both have a height of $H = 5.5\,\mu$m. The widths of the cores are denoted $W_1$ and $W_2$, their center-to-center separation is *Sep* and their edge-to-edge gap is $G_{E2E}$, which is given from:

$$Sep = G_{E2E} + 0.5(W_1 + W_2) \quad (A.4)$$

The two coupled waveguides could e.g. constitute the coupling region in a directional coupler. The cross coupling is (see section 5.2.1):

$$P_c = (\frac{C}{\kappa})^2 \sin^2(\frac{\pi(L_{st} + \delta L_b)}{L_c}) = \frac{C}{\kappa})^2 \sin^2(\phi) \quad (A.5)$$

where $(C/\kappa)^2$ is the cross coupling amplitude, $L_{st}$ is the length of the coupling region, $\delta L_b$ is the equivalent length from the bends and $L_c$ is the coupling length

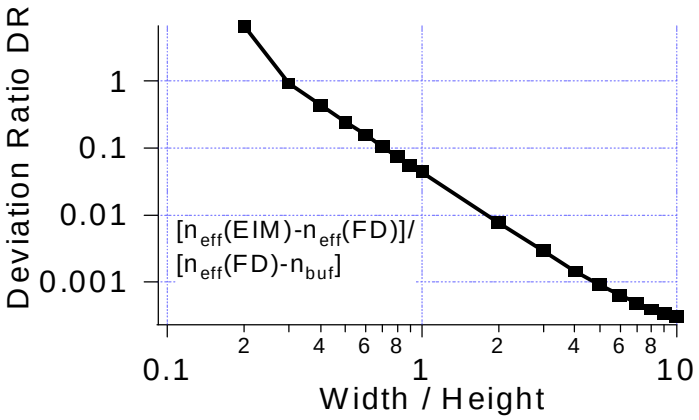


Figure A.2: The deviation ratio $DR$ between the effective index resulting from a *EIM-x* and a *FD* simulation as a function of the ratio between the core width $W$ and height $H$.

and $\phi$ is denoted the coupling strength. The coupling length is given as:

$$L_c = \frac{\lambda}{2(n^S_{eff,0} - n^S_{eff,1})} \tag{A.6}$$

where $n^S_{eff,0}$ and $n^S_{eff,1}$ are the effective indices of the zero order and first order mode of the composite structure. The cross coupling amplitude is:

$$(\frac{C}{\kappa})^2 = \frac{(\beta^S_0 - \beta^S_1)^2}{\sqrt{0.25\Delta\beta^2 + (\beta^S_0 - \beta^S_1)^2}} \tag{A.7}$$

where $\Delta\beta$ is the difference between the propagation constant of the 2 cores when viewed in isolation.

To compare the accuracy of the *EIM-x* method with that of the *FD* method the coupling length and cross coupling amplitude is simulated as a function of the asymmetry between the two cores. Define the width asymmetry as:

$$WA = \frac{(W_1 - W_2)}{W_1} \tag{A.8}$$

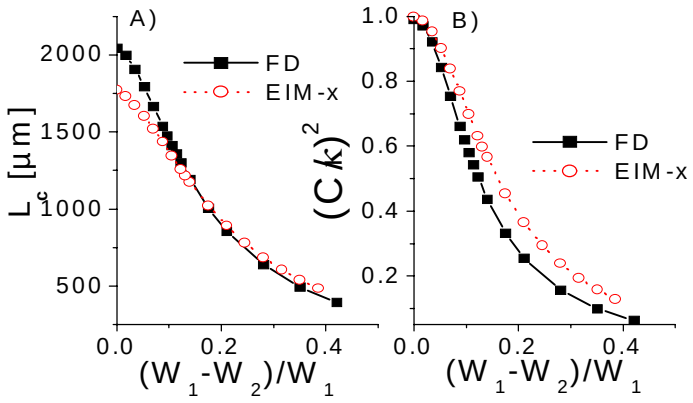


Figure A.3: *A*) The coupling length $L_c$ and *B*) the cross coupling amplitude $(C/\kappa)^2$ as a function of the width asymmetry $WA$ in a two core structure.

Fig. A.3*A* shows the simulated coupling length as a function of the width asymmetry for a two core structure with $W_1 = 5.7\,\mu$m and $G_{E2E} = 3.8\,\mu$m and varying $W_2$. The figure shows that the coupling length decreases when the width asymmetry increases. For a symmetric structure the coupling length is approximately 15% longer in the *FD* method than in the *EIM-x*, but the coupling length decreases faster with the asymmetry in the *FD* than in the *EIM-x* simulation. For a width asymmetry of $WA \simeq 0.15$ the coupling lengths are approximately equal and for larger width asymmetries the coupling length from the *FD* method is actually shorter than from the *EIM-x*. Fig. A.3*B* shows the cross coupling amplitude as a function of the width asymmetry. For zero asymmetry both methods give unity cross coupling amplitude and they both converge to zero cross coupling amplitude as the width asymmetry goes to infinity. In the intermediate region the cross coupling amplitude is smaller in the *FD* than in the *EIM-x* simulation reaching a maximum difference of approximately 0.14 at a width asymmetry of $W/H \simeq 0.15$. If the two methods are used to predict the cross coupled power in a uniform asymmetric coupler the results therefore in general are quite different.

A similar investigation shows that the deviation between the simulation results from the two methods increases with the separation between the waveg-

uides.

## A.2 Comparison of $2D$ and $3D$ *BPM*

Both the $2D$ and the $3D$ *BPM* are used extensively in this work. The $2D$ *BPM* uses the *EIM-x* as a mode solver, and hereby is not an exact solution of the wave equation. The $3D$ *BPM* on the other hand uses the *FD* method and accordingly is an asymptotically correct solution of the wave equation. The reason for using $2D$ *BPM* is, that it is much faster than the $3D$ *BPM* as the calculation window here is not discretized in the $y$-direction. Hereby it is possible to perform a lot of simulations in a limited time, whereas the $3D$ *BPM* is quite time consuming as a typical simulation for a single coupler takes on the order of 15 mn.

The settings for the *BPM* simulations are as follows, the calculation window is $50\,\mu$m wider than the considered components and has a height of $20\,\mu$m, the grid spacing is $0.2\,\mu$m and transparent boundary conditions are used. The beam propagation step is $2\,\mu$m.

### A.2.1 Comparison for directional couplers

The first test is to validate that the $2D$ and $3D$ *BPM* give the same result for the coupling length and cross coupling amplitude as the *EIM-x* and *FD* method, respectively. Hereafter the *BPM* simulations are compared directly for uniform directional couplers, see fig. 5.2. The nomenclature for the coupling region is identical to the previous description of two coupled waveguides. Instead of describing the coupler by the bar $P_b$ and cross coupling $P_c$ the imbalance is used, which is defined as:

$$IMB = 10\log(\frac{P_b}{P_c}) \tag{A.9}$$

Fig. A.4*A* shows the imbalance as a function of the wavelength for a uniform symmetric (*US*) coupler with $W_1 = W_2 = 4.0\,\mu$m, $Sep = 9.0\,\mu$m and $L_{st} = 418\,\mu$m. The length is chosen to give the shortest possible 3 $dB$ coupler for a $2D$ *BPM* at $\lambda = 1550$ nm (i.e. it has a coupling strength of $\phi = \pi/4$). The figure shows that in both cases the imbalance is decaying approximately linearly with the wavelength, as the coupling length is decaying with the wavelength. The curve from the $3D$ *BPM* is between 0.5 $dB$ and 1.0 $dB$ above the curve from the $2D$ *BPM*. Recall that fig. A.3 shows that the coupling length is longer in the *FD* than in the *EIM-x* simulation. This results in a smaller coupling

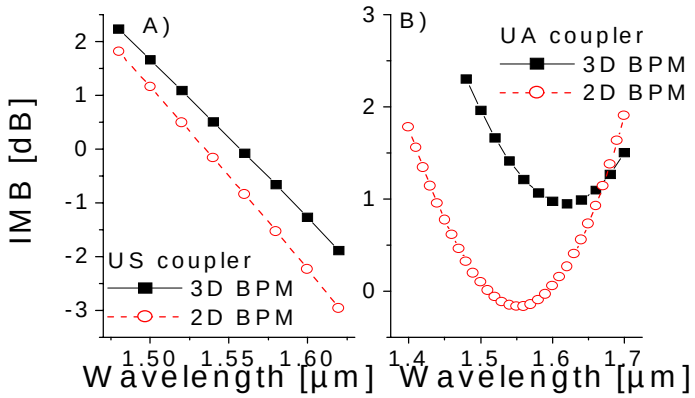


Figure A.4: The simulated wavelength response of *A*) a *US* coupler and *B*) a *UA* coupler. The plots show the results of both $2D$ and $3D$ *BPM* simulations.

strength in the $3D$ than in the $2D$ *BPM* and hereby a more positive imbalance, compare eq. A.9 and eq. A.9. In conclusion fig. A.4*A* shows that the $2D$ and $3D$ *BPM* predictions are quite different, whence the $2D$ *BPM* cannot be used solely to investigate a directional coupler. However, the functional form of the two curves is the same and thus the $2D$ *BPM* can be used to qualitatively investigate the effect of changes in wavelength.

Fig. A.4*B* shows the imbalance as a function of the wavelength for a uniform asymmetric (*UA*) coupler with $W_1 = 5.70\,\mu$m, $W_2 = 5.15\,\mu$m, $Sep = 9.23\,\mu$m and $L_{st} = 1500\,\mu$m. The design is chosen from a $2D$ *BPM* to give a wavelength flattened 3 *dB* coupler centered at $\lambda = 1550\,$nm. The figure shows that both the wavelength of minimum imbalance and the value of the minimum imbalance is different in the two methods. However, the two curves again have the same functional shape, which indicates that the $2D$ *BPM* can also here be used to qualitatively predict the effect of a change of wavelength.

By a similar comparison it was found that the $2D$ *BPM* can also be used to qualitatively give the effect of changing other parameters of the uniform directional couplers. Thus the $2D$ *BPM* can be used in the initial part of an investigation of a given architecture to estimate its wavelength dependence and process tolerance, and determine whether it should be investigated further using

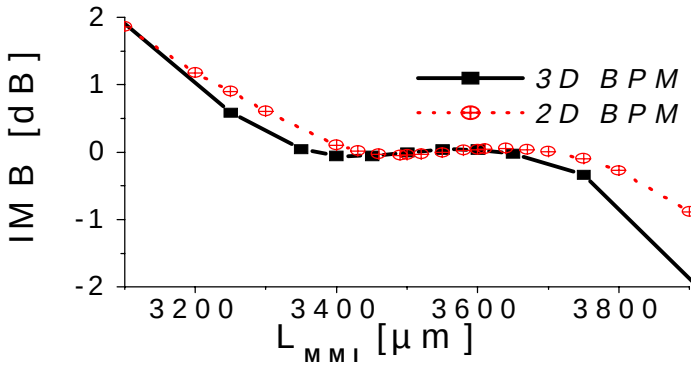


Figure A.5: The simulated imbalance from a $2D$ and a $3D$ *BPM* as a function of the *MMI* length of a $2x2$ *MMI* coupler.

the asymptotically correct $3D$ *BPM*.

### A.2.2 Comparison for *MMI* couplers

In the comparison between the *EIM-x* and the *FD* method it was shown that the accuracy of the *EIM-x* increases with the ratio of the width to the height. Consequently it is expected that the agreement between the $2D$ and $3D$ *BPM* is better for a *MMI* coupler than it was for the directional coupler. Fig. A.5 shows the imbalance as a function of the *MMI* length as simulated with the $2D$ and $3D$ *BPM*. The *MMI* coupler has $W = 40\,\mu$m, $H = 5.50\,\mu$m and is excited with an access waveguide having a width of $W_A = 13.8\,\mu$m that is placed $13.4\,\mu$m from the transversal symmetry axis of the *MMI* coupler, see fig. 5.10. The figure shows that the predictions from the $2D$ and $3D$ *BPM* are very similar, but that the curve from the $2D$ *BPM* is displaced towards slightly larger *MMI* length. However, the discrepancy is very small, which confirms that the $2D$ *BPM* is an excellent description of the *MMI* coupler.

# Appendix B

# Transfer matrix for the $1x4$ *MUX/DEMUX*

This purpose of this appendix is to calculate the transfer matrix of the passive $1x4$ optical *MUX/DEMUX* described in chapter 7. To increase the generality the *MUX* is generalized to a $4x4$ *MUX*, from which the response of the $1x4$ *MUX* can be found by considering a single input arm.

## B.1 The individual transfer matrices

The *MUX* architecture can be seen on fig. 7.3. It consists of an input *MMI* $1x4$ coupler, 4 interferometer arms with delays differing by units of $\Delta T$ and a output *MMI* $4x4$ coupler. On each interferometer arm there is a phase controlling element $(\alpha_q)$ and a single-stage all-pass filter having a delay of $\Delta T^{AP}$, a pole magnitude $\rho_q$ and a frequency of $\phi_q$. As previously mentioned the discussion is generalized to a $4x4$ *MUX,* which is obtained by replacing the input $1x4$ *MMI* coupler with a $4x4$ *MMI* coupler.

The transfer matrix of the non-ideal $4x4$ *MMI* is [93]:

$$\underline{T}_{4x4} = \begin{bmatrix} -c_{11} & c_{12}\exp(\frac{i7\pi}{4}) & c_{13}\exp(\frac{i3\pi}{4}) & -c_{14} \\ c_{12}\exp(\frac{i7\pi}{4}) & -c_{22} & -c_{23} & c_{13}\exp(\frac{i3\pi}{4}) \\ c_{13}\exp(\frac{i3\pi}{4}) & -c_{23} & -c_{22} & c_{12}\exp(\frac{i7\pi}{4}) \\ -c_{14} & c_{13}\exp(\frac{i3\pi}{4}) & c_{12}\exp(\frac{i7\pi}{4}) & -c_{11} \end{bmatrix} \quad \text{(B.1)}$$

where $c_{ij} \in C$ are the non-ideality coefficients, which in the ideal case all are equal to 1. Notice that the number of independent coefficients in the $4x4$ matrix is reduced from 16 to 6, which is casued by that the *MMI* coupler has transversal as well as longitudinal symmetry.

The transfer function of the interferometer arms is diagonal, since the arms are independent (i.e. there is no coupling between the arms). The size of the non-zero elements is obtained by multiplying the delay of the particular arm with the transfer matrix of the all-pass filter in that arm:

$$\begin{bmatrix} (\underline{T}_{Arms})_{1,1} \\ (\underline{T}_{Arms})_{2,2} \\ (\underline{T}_{Arms})_{3,3} \\ (\underline{T}_{Arms})_{4,4} \end{bmatrix} = \begin{bmatrix} z^{-1} \cdot \frac{+\rho_1 + Gz^{-4}}{1+G\rho_1 z^{-4}} \\ z^{-2} \cdot \frac{+\rho_2 + Gz^{-4}}{1+G\rho_2 z^{-4}} \\ \frac{+\rho_3 + Gz^{-4}}{1+G\rho_3 z^{-4}} \\ z^{-3} \cdot \frac{+\rho_4 + Gz^{-4}}{1+G\rho_4 z^{-4}} \end{bmatrix} \tag{B.2}$$

where it has been utilized that the all-pass filters have $\phi = \pi$ and $G$ denotes the amplitude transmission of a single round trip through the filter, whence the loss per round trip is: $L = -10\log_{10}(G^2)$.

Assume that the phase shifts $\alpha_q$ are chosen so that all the light from input arm 1 goes to output arm 1 at $f_N = 0$. This implies that the transfer matrix for the phase shifts is:

$$\underline{T}_{PhS} = \begin{bmatrix} 1 & 0 & 0 & 0 \\ 0 & i & 0 & 0 \\ 0 & 0 & -i & 0 \\ 0 & 0 & 0 & 1 \end{bmatrix}$$

## B.2 The total transfer matrix

The total transfer matrix of the *MUX* is found by matrix multiplication:

$$\underline{T_{n,m}} = \underline{T}_{4x4} \cdot \underline{T}_{Arms} \cdot \underline{T}_{PhS} \cdot \underline{T}_{4x4} \tag{B.3}$$

where $n$ and $m$ are the number of the input and output arms, respectively. The matrix multiplication is straightforward although lengthy. It gives a transfer matrix of the form:

$$\underline{T_{n,m}}(z) = \frac{\sum_{r=0}^{19} b_{n,m}(r) z^{-r}}{1 + \sum_{s=1}^{4} a_{4s} z^{-4s}} \tag{B.4}$$

where the coefficients $b_m$ and $a_s$ depend on the parameters of the *MUX*. Notice that the denominator is independent of the choice of input and output arm, and that it furthermore only has five non-zero terms. The delay in the non-zero terms correspond to what would be obtained by either $1, 2, 3$ or $4$ round trips in one of the all-pass filters.

## B.3 The transfer matrix for ideal *MMI* couplers

To evaluate the transfer matrix elements consider input arm 1, and assume that the *MMI* couplers are ideal.

The denominator for all elements is:

$$\begin{aligned}\mathbf{a} \;=\; & \{1 + G(\rho_1 + \rho_2 + \rho_3 + \rho_4)z^{-4} + \\ & G^2(\rho_1\rho_2 + \rho_1\rho_3 + \rho_1\rho_4 + \rho_2\rho_3 + \rho_2\rho_4 + \rho_3\rho_4)z^{-8} + \\ & G^3(\rho_1\rho_2\rho_3 + \rho_1\rho_2\rho_4 + \rho_1\rho_3\rho_4 + \rho_2\rho_3\rho_4)z^{-12} + \\ & G^4\rho_1\rho_2\rho_3\rho_4 z^{-16}\}\end{aligned} \tag{B.5}$$

which as previously mentioned only has five non-zero elements. The numerator for input arm 1 and output arm 1 is:

$$\begin{aligned}\mathbf{b}_{1,1} \;=\; & 0.25\{\rho_3 + \rho_1 z^{-1} + \rho_2 z^{-2} + \rho_4 z^{-3} + \\ & G[(1 + \rho_3(\rho_1 + \rho_2 + \rho_4))z^{-4} + (1 + \rho_1(\rho_2 + \rho_3 + \rho_4))z^{-5} + \\ & (1 + \rho_2(\rho_1 + \rho_3 + \rho_4))z^{-6} + (1 + \rho_4(\rho_1 + \rho_2 + \rho_3))z^{-7}] + \\ & G^2[(\rho_1 + \rho_2 + \rho_4 + \rho_3(\rho_1\rho_2 + \rho_1\rho_4 + \rho_2\rho_4))z^{-8} + \\ & (\rho_2 + \rho_3 + \rho_4 + \rho_1(\rho_2\rho_3 + \rho_2\rho_4 + \rho_3\rho_4))z^{-9} + \\ & (\rho_1 + \rho_3 + \rho_4 + \rho_2(\rho_1\rho_3 + \rho_1\rho_4 + \rho_3\rho_4))z^{-10} + \\ & (\rho_1 + \rho_2 + \rho_3 + \rho_4(\rho_1\rho_2 + \rho_1\rho_3 + \rho_2\rho_3))z^{-11}] + \\ & G^3[(\rho_2\rho_4 + \rho_1\rho_2 + \rho_1\rho_4 + \rho_1\rho_2\rho_3\rho_4)z^{-12} + \\ & (\rho_3\rho_4 + \rho_2\rho_3 + \rho_2\rho_4 + \rho_1\rho_2\rho_3\rho_4)z^{-13} \\ & (\rho_3\rho_4 + \rho_1\rho_3 + \rho_1\rho_4 + \rho_1\rho_2\rho_3\rho_4)z^{-14} + \\ & (\rho_2\rho_3 + \rho_1\rho_2 + \rho_1\rho_3 + \rho_1\rho_2\rho_3\rho_4)z^{-15}] + \\ & G^4[\rho_1\rho_2\rho_4 z^{-16} + \rho_2\rho_3\rho_4 z^{-17} + \rho_1\rho_3\rho_4 z^{-18} + \rho_1\rho_2\rho_3 z^{-19}]\}\end{aligned} \tag{B.6}$$

where the effect of ring loss is given through the parameter $G$. The numerator

of the other output arms are found as:

$$b_{1,2}(r) = i^m b_{1,1}(r) \quad \text{(B.7)}$$
$$b_{1,3}(r) = i^{(3m+2)} b_{1,1}(r) \quad \text{(B.8)}$$
$$b_{1,4}(r) = i^{2m} b_{1,1}(r) \quad \text{(B.9)}$$

where $r$ is the number of the term. Thus the numerator has the same functional form for all four output arms. Since the denominator is identical for all output arms this implies that their response is identical although centered at different wavelengths.

Furthermore a calculation shows that the same spectra are obtained by using any of the other input arms, although centered at a different wavelength.

## B.4 Including the effect of non-ideal *MMI* couplers

By lifting the assumption of an ideal *MMI* couplers the complexity of the numerator increases, but the denominator remains unchanged. The effects is that the weight of the individual terms in the numerator changes due to the non-ideality terms. Accordingly the total numerator $b_{1,1}$ is:

$$\begin{aligned}
\mathbf{b}_{1,1} = \; & 0.25\{\rho_3 + \rho_1 z^{-1} + \rho_2 z^{-2} + \rho_4 z^{-3} + \\
& G[c_{13}^2(1+\rho_3(\rho_1+\rho_2+\rho_4))z^{-4} + c_{11}^2(1+\rho_1(\rho_2+\rho_3+\rho_4))z^{-5} + \\
& c_{12}^2(1+\rho_2(\rho_1+\rho_3+\rho_4))z^{-6} + c_{14}^2(1+\rho_4(\rho_1+\rho_2+\rho_3))z^{-7}] + \\
& G^2[c_{13}^2(\rho_1+\rho_2+\rho_4+\rho_3(\rho_1\rho_2+\rho_1\rho_4+\rho_2\rho_4))z^{-8} + \\
& c_{11}^2(\rho_2+\rho_3+\rho_4+\rho_1(\rho_2\rho_3+\rho_2\rho_4+\rho_3\rho_4))z^{-9} + \\
& c_{12}^2(\rho_1+\rho_3+\rho_4+\rho_2(\rho_1\rho_3+\rho_1\rho_4+\rho_3\rho_4))z^{-10} + \\
& c_{14}^2(\rho_1+\rho_2+\rho_3+\rho_4(\rho_1\rho_2+\rho_1\rho_3+\rho_2\rho_3))z^{-11}] + \\
& G^3[c_{13}^2(\rho_2\rho_4+\rho_1\rho_2+\rho_1\rho_4+\rho_1\rho_2\rho_3\rho_4)z^{-12} + \\
& c_{11}^2(\rho_3\rho_4+\rho_2\rho_3+\rho_2\rho_4+\rho_1\rho_2\rho_3\rho_4)z^{-13} + \\
& c_{12}^2(\rho_3\rho_4+\rho_1\rho_3+\rho_1\rho_4+\rho_1\rho_2\rho_3\rho_4)z^{-14} + \\
& c_{13}^2(\rho_2\rho_3+\rho_1\rho_2+\rho_1\rho_3+\rho_1\rho_2\rho_3\rho_4)z^{-15}] + \\
& G^4[c_{13}^2\rho_1\rho_2\rho_4 z^{-16} + c_{11}^2\rho_2\rho_3\rho_4 z^{-17} \\
& + c_{12}^2\rho_1\rho_3\rho_4 z^{-18} + c_{14}^2\rho_1\rho_2\rho_3 z^{-19}]\}
\end{aligned} \quad \text{(B.10)}$$

whence the weight of each individual terms changes with the product of two non-ideality terms. In the shown example the number of input and output arm are identical thus it is the same non-ideality term which is squared. If the input and output arm have different number the product will be between two different terms.

# Appendix C

# Functional analysis

Assume that the transfer function of a component is given as a function of one argument $x$:

$$T(x) = g[f(x)] \tag{C.1}$$

where $g$ and $f$ are invertible functions. Using eq. C.1 it is possible to find the argument $x_1$ giving a desired output $y$

$$\begin{aligned} T(x_1) &= y \Leftrightarrow & \text{(C.2)} \\ f(x_1) &= g^{-1}(y) \Leftrightarrow & \text{(C.3)} \\ x_1(y) &= f^{-1}[g^{-1}(y)] & \text{(C.4)} \end{aligned}$$

where $g^{-1}$and $f^{-1}$ are the inverse functions of $g$ and $f$, respectively.

Assume furthermore that process deviations leads to changes that can be described within the functional form of $g$, but with another argument:

$$T_2 = g[f_2(x)] \tag{C.5}$$

accordingly there will be a different argument $x_2$ giving the output $y$:

$$x_2(y) = f_2^{-1}[g^{-1}(y)] \tag{C.6}$$

where $f_2^{-1}$ is the inverse of $f_2$. The ratio of the arguments $x_1$ and $x_2$ giving the output $y$ is:

$$\frac{x_1(y)}{x_2(y)} = \frac{f^{-1}[g^{-1}(y)]}{f_2^{-1}[g^{-1}(y)]} \tag{C.7}$$

Consider the special case where $f$ and $f_2$ are directly proportional to $x$, i.e.:

$$f(x) = ax \Leftrightarrow f^{-1}(x) = a^{-1}x \tag{C.8}$$
$$f_2(x) = a_2x \Leftrightarrow f_2^{-1}(x) = a_2^{-1}x \tag{C.9}$$

by inserting this into eq. C.7 one obtains:

$$\frac{x_1(y)}{x_2(y)} = \frac{a_2g^{-1}(y)}{a_1g^{-1}(y)} = \frac{a_2}{a_1} \tag{C.10}$$

whereby the ratio is independent of the output value $y$. This means that under the assumption of direct proportionality between $f$, $f_2$ and $x$, the ratio of the predicted values for the argument $x$ resulting in a constant output $y$ are independent of the value of $y$.

## C.1 The uniform symmetrical coupler

As an example consider a uniform symmetrical directional coupler where the length of the coupling region $L_{st}$ is varied. The cross coupling $P_c$ is [8]:

$$P_c = \sin^2[\frac{\pi(L_{st} + \delta L_b)}{L_c}] = \sin^2\phi \tag{C.11}$$

where $\delta L_b$ is an equivalent length giving the amount of coupling in the bends, $L_c$ is the coupling length and $\phi$ is denoted the coupling strength. Set $x := L_{st} + \delta L_b$ and compare eq. C.1 and eq. C.11 to obtain:

$$f(x) = \frac{\pi x}{L_c} = \phi \tag{C.12}$$
$$g[f(x)] = \sin^2[f(x)] \tag{C.13}$$

whereby $f$ is directly proportional to $x$ and $g[f(x)]$ is invertible provided that the coupling strength is limited to $0 < f(x) < \pi/2$.

Changes in the coupler parameters of the uniform symmetrical directional coupler leads to changes in the coupling length, but assume that the equivalent length from the bends $\delta L_b$ remains unchanged. Thus the new functional form $f_2(x)$, which results from the change in coupler parameters is also directly proportional to $x$. Within the approximation the ratio between the predicted values of the argument $x$ giving a constant cross coupling $P_c$ from the original transfer function and the new transfer function is independent of value of the cross coupling $P_c$.

| $\lambda = 1550\,\mathrm{nm}$ | $L_c$ | $Dev(L_c)$ | $\delta L_b$ | $Dev(\delta L_b)$ | $Dev(Lc)/Dev(\delta L_b)$ |
|---|---|---|---|---|---|
| $W = 4.8\,\mu\mathrm{m}$ | 3008 | 1.89% | 332.2 | 0.73% | 2.60 |
| $W = 5.0\,\mu\mathrm{m}$ | 2952 | 0% | 329.8 | 0% | 0 |
| $W = 5.2\,\mu\mathrm{m}$ | 2888 | −2.17% | 327.7 | −0.64% | 3.42 |

Table C.1: The simulated (2D BPM) variation in the coupling length and equivalent length from the bends in a uniform directional coupler as a function of the waveguide width.

A number of $2D$ *BPM* simulation were performed for uniform symmetrical couplers to examine whether the assumption of unchanged equivalent length from the bends holds for process induced changes. The coupler parameters are: step-index: $\Delta n = 0.010$, waveguide height: $H = 5.50\,\mu\mathrm{m}$, center-to-center separation: $Sep = 9.0\,\mu\mathrm{m}$ and waveguide width: $W = 5.0\,\mu\mathrm{m} + \delta WWR$, where $\delta WWR$ is the deviation from the nominal waveguide width reduction. To compare the changes define the deviation from the nominal value (in %) as:

$$Dev(x) = 100\frac{x - x_0}{x_0} \tag{C.14}$$

where the $x_0$ is the nominal value of the design parameter.

Table shows C.1 the simulated values of the coupling length and equivalent length from the bends for widths of $W \in (4.8, 5.0, 5.2)\,\mu\mathrm{m}$ at a wavelength of $\lambda = 1550\,\mathrm{nm}$ and the deviation in these quantities as compared to the values for a width of $W = 5.0\,\mu\mathrm{m}$. The table shows that the deviation in coupling length is a factor of $2 - 4$ larger than the change in equivalent bend length. A numerical investigation shows this behavior is quite typical, accordingly the assumption of unchanged equivalent bend length is not accurate.

Thus it is investigated how the ratio of the length of the coupling region $L_{st}$ giving a fixed cross coupling $P_c$ obtained for two different widths of the waveguides in the coupler depends on the value of the cross coupling. By using the values from table C.1 and dividing by with the length for a width of $W = 5.0\,\mu\mathrm{m}$ the dependency shown in fig. C.1 is obtained. The curves are only valid for a coupler, where the coupling strength is less than $\pi/2$.

Fig. C.1 shows that the ratio between the lengths for $W = 4.8\,\mu\mathrm{m}$ and $W = 5.0\,\mu\mathrm{m}$ is larger than unity and decaying with the cross coupling, whereas the ratio between the lengths for $W = 5.2\,\mu\mathrm{m}$ and $W = 5.0\,\mu\mathrm{m}$ is smaller than unity and increasing with the cross coupling. The reason is that the importance of the equivalent length from the bends decreases with the coupling strength

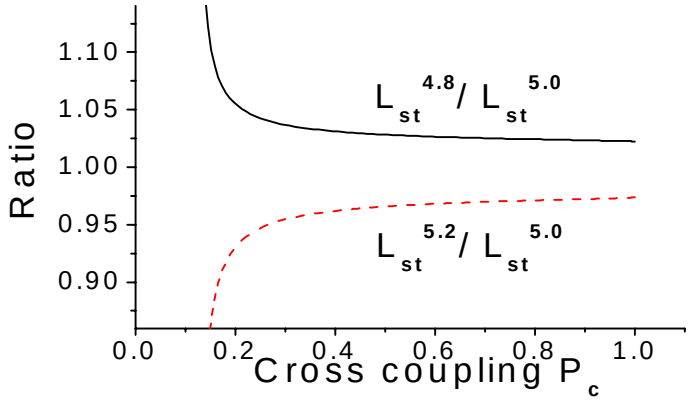


Figure C.1: The ratio of the length of the coupling region $L_{st}$ giving a fixed output power for different widths of the waveguides in the coupler as a function of the cross coupling.

(the ratio of $L_{st}/\delta L_b$ increases). If the coupling strength is increased beyond the considered limit the equivalent length from the bends eventually becomes negligible, which implies that the ratio between the lengths monotonically converges to the ratio between the coupling lengths, as predicted from eq. C.10. In the considered example the two ratios are 1.019 and 0.978.

Notice that due to the coupling in the bends it is not possible to construct a uniform symmetric coupler with arbitrarily small coupling strength, and therefore the curves on fig. C.1 can not be extended to a cross coupling smaller than $P_c < 0.1$. Close to the minimum obtainable cross coupling the ratios depend strongly on the value of the cross coupling, but apart from this region the dependency is rather small. For a cross coupling larger than $P_c > 0.3$ the ratio changes less than 2% by a further increase in coupling strength. Thus the numerical investigation shows that although the equivalent length from the bend changes with the process parameters, the ratio between the lengths giving a constant cross coupling is still fairly constant.

# Appendix D

# List of publications

- L. Leick, J. H. Povlsen and R. J. S. Pedersen, "Numerical and experimental investigation of 2x2 multi mode interference couplers in silica-on-silicon", *Optical and Quantum Electronics*, Vol. 33, pp. 387-398 (2001).

- L. Leick, A. Harpøth and M. Svalgaard, "Empirical model for the waveguiding properties of directly UV written waveguides", Accepted for publication in *Applied Optics*

- L. Leick, and C. K. Madsen, "Dispersion compensation of a 1 x N router with low loss, flat passband and low crosstalk", Accepted for publication in *Optics Letters* (February 2002)

- L. Leick, J. H. Povlsen and R. J. S. Pedersen, "Achieving small process tolerant wavelength-flattened 3 dB directional couplers in Silica-on-Silicon", *Integrated Photonics Research 2000*, Paper IThB6, Quebec City, Canada, July (2000)

- L. Leick, M. Svalgaard and J. H. Povlsen, "Impact of weak index perturbations on 3 dB multi mode interference couplers" *Integrated Photonics Research 2001*, Paper IMC3, Monterey, California, USA, June (2001)

- L. Leick, and C. Peucheret "Dispersion induced penalty for 1xN passive interferometric optical MUX/DEMUXs and its reduction using all-pass filters", Accepted for presentation at *European Conference on Optical Communication 2002*

- M. Svalgaard, A. Harpøth and L. Leick, "Empirical model for the waveguiding properties of directly UV written waveguides", *Bragg Gratings, Poling and Photosensitivity 2001*, Paper BThC32, Stresa, Italy, July (2001).

- R. K. Sandberg and L. Leick, "Novel design for integrated wavelength flat 980/1550 nm multiplexer", Accepted for presentation at *Integrated Photonics Research 2002*

- J. H. Povlsen and L. Leick, "Multi mode interference couplers in silica-on-silicon", *News of the Danish Optical Society (DOPS-NYT)*, No. 2, pp. 43-46 (2001).

# Bibliography


[1] V. Khosla, The Terabit Tsunami, OFC 2001 (2001).

[2] G. P. Agrawal, *Fiber-Optic Communication Systems*, Wiley, New York, 1997.

[3] S. Bigo, Y. Frignac, G. Charlet, W. Idler, S. Borne, H. Gross, R. Dischler, W. Poehlmann, P. Tran, C. Simonneau, D. Bayart, G. Veith, A. Jourdan, and J.-P. . Hamaide, 10.2 Tbit/s (256x42.7 Gbit/s PDM/WDM) transmission over 100 km TeraLight/sup TM/ fiber with 1.28 bit/s/Hz spectral efficiency, OFC 2001 **4**, PD25 (March 2001).

[4] G. Vareille, F. Pitel, and J. Marcerou, 3Tbit/s (300x11.6Gbit/s) transmission over 7380 km using C+L band with 25GHz channel spacing and NRZ format, OFC 2001 **4**, PD22 (March 2001).

[5] R. Ryf, J. Kim, J. P. Hickey, A. Gnauck, D. Carr, F. Pardo, C. Bolle, R. Frahm, N. Basavanhally, C. Yoh, D. Ramsey, R. Boie, R. George, J. Kraus, C. Lichtenwalner, R. Papzian, J. Gates, H. R. Shea, A. Gasparyan, V. Muratov, J. E. Grifftih, J. A. Prybyla, C. D. Goyal, S. and-White, M. T. Lin, R. Ruel, C. Nijander, S. Arney, D. T. Neilson, D. J. Bishop, P. Kolodner, S. Pau, C. Nuzman, A. Weis, B. Kumar, D. Liuwen, V. Aksyuk, D. S. Greywall, T. C. Lee, H. T. Soh, W. M. Mansfield, S. Jin, W. Y. Lai, H. A. Huggins, D. L. Barr, R. A. Cirelli, G. R. Bogart, R. Teffeau, R. Vella, H. Mavoori, A. Ramirez, N. A. Ciampa, F. P. Klemens, M. D. Moris, T. Boone, J. Q. Liu, J. M. Rosamilla, and C. R. Giles, 1296-port MEMS Transparent Optical Crossconnect with 2.07Petabit/s Switch Capacity, OFC 2001 (Paper PD28), PD28 1–3 (2001).

[6] E. Pennings, G.-D. Khoe, M. Smit, and T. Staring, Integrated-Optic Versus Microoptic Devices for Fiber Optic Telecommunications Systems:

A Comparison, IEEE Journal of Selected Topics in Quantum Electronics **2**(2), 151–164 (1996).

[7] I. P. Kaminov, T. L. Koch, Authors, Y. P. Li, and C. H. Henry, *Optical Fiber Telecommunications IIIB: Silicon Optical Bench Waveguide Technology*, Academic Press, San Diego, 1997.

[8] A. W. Snyder and J. D. Love, *Optical waveguide theory*, Chapman and Hall, London, UK, 1983.

[9] D. Marcuse, *Theory of dielectric optical waveguides*, Academic Press, New York, 1991.

[10] R. Marz, *Integrated optics: Design and modeling*, Artech House, Boston, 1994.

[11] F. Ladouceur and J. D. Love, *Silica-Based Buried Channel Waveguides and Devices*, Chapman and Hall, London, UK, 1996.

[12] R. Scarmozzino, A. Gopnath, R. Pregla, and S. Helfert, Numerical Techniques for Modeling Guided-Wave Photonic Devices, IEEE Journal of Selected Topics in Quantum Electronics **6**(1), 150–162 (2000).

[13] T. P. Rasmussen, *Integrates Optical Structures for Optical Communications*, PhD thesis, EMI, Technical University of Denmark, 1994.

[14] E. A. J. Marcatili, Bends in dielectric guides, Bell. Syst. Tech. J. **48**(7), 2103–2132 (1969).

[15] I. Ilic, R. Scarmozzino, and R. M. Osgood, Investigation of the Padé Approximant-Based Wide-Angle Beam Propagation Method for Accurate Modeling of Waveguiding Circuits, J. Lightwave Technol. **14**(12), 2813–2822 (1996).

[16] D. Huang, T. Chiu, and Y. Lai, Arrayed Waveguide DWDM Interleaver, OFC 2001 **3**, WDD1–3 (2001).

[17] H. Rao, R. Scarmozzino, and R. M. Osgood, A bidirectional beam propagation method for multiple dielectric interfaces, Photon. Technol. Lett. **11**, 830–832 (1999).

[18] D. Zauner, *Integrated Optical Devices for Wavelength Division Multiplexing Using PECVD and Direct UV-Writing Techniques*, PhD thesis, COM, Technical University of Denmark, 1999.

[19] K. Jinguji, N. Takato, Y. Hida, T. Kitoh, and M. Kawachi, Two-Port Optical Wavelength Circuits Composed of Cascaded Mach-Zehnder Interferometers with Point-Symmetrical Configurations, J. Lightwave Technol. **14**(10), 2301–2310 (1996).

[20] A. Takagi, K. Jinguji, and M. Kawachi, Design and Fabrication of Broad-Band Silica-Based Optical Waveguide Couplers with Asymmetric Structure, J. Quantum Electron. **28**(4), 848–855 (1992).

[21] A. Takagi, K. Jinguji, and M. Kawachi, Silica-Based Waveguide-Type Wavelength-Insensitive Couplers (WINC'S) with Series-Tapered Coupling Structure, J. Lightwave Technol. **10**(12), 1814–24 (1992).

[22] K. Jinguji, N. Takato, A. Sugita, and M. Kawachi, Mach-Zehnder Interferometer Type Optical Waveguide Coupler with Wavelength-Flattened Coupling Ratio, Electron. Lett. **26**(17), 1326–1327 (1990).

[23] M. Kuznetsov, N. M. Froberg, S. R. Henion, and K. A. Rauschenbach, Power penalty for Optical signals due to Dispersion Slope in WDM filter Cascades, IEEE Photon. Tecnol. Lett. **11**(11), 1411–1413 (1999).

[24] M. Kuznetsov and D. O. Caplan, Time-frequency analysis of optical communication signals and effects of second and third order dispersion, Conference on Lasers and Electro-Optics (CLEO 2000) **TOPS 39**, 281–282 (2000).

[25] C. K. Madsen and J. H. Zhao, *Optical filter design and analysis*, Wiley, New York, 1999.

[26] J. Leuthold, R. Ryf, D. Chandrasekhar, D. Neilson, C. Joyner, and C. Giles, All-Optical NOnblocking Terabit/s Crossconect Based on Low Power All-Optical Wavelength Converter and MEMS SWitch Fabric, OFC 2001 (Paper PD16), PD16 1–3 (2001).

[27] Y. Hibino, F. Hanawa, H. Nakagome, M. Ishii, and N. Takato, High reliability optical power splitters composed of silica-based planar lightwave circuits, J. Lightwave Technol. **13**, 1728–1735 (1995).

[28] R. Syms, *Advances in integrated optics*, Plenum Press, New York, 1994.

[29] J. Hübner, S. Guldberg-Kjær, M. Dyndgaard, Y. Shen, C. L. Thomsen, S. Balslev, C. Jensen, D. Zauner, and T. Feuchter, Planar Er- and Yb-doped amplifiers and lasers, Appl. Phys. B **73**, 435–438 (2001).

[30] M. W. Sckerl, S. A. Gulberg-Kjær, C. Lauernt-Lund, and M. Rysholt Poulsen, Loss-less Planar Waveguide 1:4 Power Spllitter at 1550 nm, Ecoc 1999 , 48–49 (Sept. 1999).

[31] J. Arentoft, *Optimisation of UV-induced processes in glass materials for photonic components*, PhD thesis, COM, Technical University of Denmark, 2000.

[32] K. Zenth, *Pigtailing of Integrated Optical Components*, PhD thesis, COM, Technical University of Denmark, 2001.

[33] C. A. Jones, K. Cooper, M. W. Nield, J. D. Rush, R. G. Waller, and P. J. Collins, J. V. adn Fiddyment, Hybrid integration of a laser diode with a planar silica waveguide, Electron. Lett. **30**(3), 215–216 (1991).

[34] K. Kato and Y. Tohmori, PLC Hybrid Integration TEchnology and Its Application to Photonic Components, IEEE Journal of Selected Topics in Quantum Electronics **6**(1), 4–13 (2000).

[35] H. Ou and J. Hübner, Silica-on-silicon waveguide fabrication, News from The Danish Optical Society (DOPS-nyt) (2), 39–42 (2001).

[36] M. Svalgaard, *Ultraviolet light induced refractive index structures in germanosilica*, PhD thesis, MIC, Technical University of Denmark, 1997.

[37] M. Svalgaard, C. Poulsen, A. Bjarklev, and O. Poulsen, Direct UV-writing of buried singlemode channel waveguides in Ge-doped silica films, Electron. Lett. **30**, 1401–1402 (1994).

[38] M. Svalgaard and M. Kristensen, Directly written silica-on-silicon planar waveguides with low loss, Electron. Lett. **33**, 861–863 (1997).

[39] M. Svalgaard, Zero-birefringence UV written waveguides, 1999 OSA Topical meeting on Bragg Gratings, Photosensitivity and Poling **Tech. Digest Series**, postdeadline paper PD–7 (1999).

[40] M. Svalgaard, Effect of D2 outdiffusion on direct UV writing of optical waveguides, Electron. Lett. **35**, 1840–1842 (1999).

[41] K. I. White, Practical application of the refracted near-field technique for the measurement of optical fibre refractive index profiles, Opt. Quant. Electr. **11**, 185–186 (1979).

[42] EXFO, Optical Waveguide Analyzer OWA-9500, www.exfo.com.

[43] M. Suzuki, S. Yanagisawa, Y. Hibino, , and K. Oda, High-density integrated planar lightwave circuits using SiO2:GeO2 waveguides with a high refractive index, J. Lightwave Technol. **12**(5), 790–796 (1994).

[44] F. Ladouceur, J. Love, and T. Senden, Effect of side wall roughness in buried channel waveguides, IEE Proc. Optoelectron. **141**(4), 242–248 (1994).

[45] F. Ladouceur, Roughness, Inhomogenity and Integrated Optics, J. Lightwave Technol. **15**(6), 1021–1025 (1997).

[46] E. Laskowski, Y. P. Li, C. Henry, and H. H. Yaffe, Optimized Waveguide Structure, Technical Report United States Patent 5 719 976, Feb. 17, 1998.

[47] K. Shiraishi, H. Ohnuki, N. Hiraguri, K. Matsumura, K. Matsumura, I. Ohisi, H. Morichi, and H. Kazami, A Lensed-Fbier Coupling Scheme Utilizing a Grade-Index Fiber and a Hemisperically Ended Coreless Fiber Tip, J. Lightwave Technol. **15**(2), 356–363 (1997).

[48] Z. Weissman and I. Hendel, Analysis of Peridically Segmented Waveguide Mode Expanders, J. Lightwave Technol. **13**(10), 2053–2058 (1995).

[49] R. Adar, W.-K. Wang, and E. J. Laskowski, Two dimensional segmentation of an integrated optics waveguide to match the waveguide's mode to that of a fibre, Technical Report European Patent EP0731366, A3, Sept. 11, 1996.

[50] B. Jacbos, R. Zengerle, K. Faltin, and W. Weiserhausen, Vertically tapered spot size transformers fabricated by a simple masking technique, Electron. Lett. **31**(10), 794–796 (1995).

[51] J. Stulemeijer, *Integrated Opyics for Microwave Phase-Array Antennas*, PhD thesis, TU Delft, 2002.

[52] H. Renner, Modes of UV-writtten planar waveguides, Optics Lett **23**, 111–113 (1998).

[53] L. Leick, J. H. Povlsen, and R. Pedersen, Numerical and Experimental Investigation of 2x2 Multimode Interference Couplers in Silica-on-Silicon, Optical Quantum. Electron. **33**, 387–398 (2001).

[54] J. H. Povlsen and L. Leick, Multi-mode interference couplers in silica-on-silicon, News of the Danish Optical Society (2), 43–46 (2001).

[55] L. Leick, J. H. Povlsen, and R. Pedersen, Achieving Small Process Tolerant Wavelength-Flattened 3 dB Directional Couplers in Silica-on-Silicon, Integrated Photonics Research (IThB6) (2000).

[56] L. Leick, M. Svalgaard, and J. H. Povlsen, Impact of weak index perturbations on 3 db multi mode interference couplers, Integrated Photonics Research (IMB3) (2001).

[57] W.-P. Huang, Coupled-Mode Theory for Optical Waveguides: An Overview, Journal of the Optical Society of America A: Optics and Image Science **11**(3), 963–983 (1994).

[58] Y. Shani, C. H. Henry, R. Kistler, and R. Kazarinov, Integrated Optic Adiabatic Device on Silicon, IEEE J. Quantum. Electron. **27**(3), 556–566 (1991).

[59] R. Adar, C. Henry, R. Kazarinov, R. Kistler, and G. Weber, Adiabatic 3-DB Couplers, Filters, and Multiplexers Made with Silica Waveguides on Silicon, J. Lightwave Technol. **10**(1), 46–50 (1992).

[60] A. Syahruar, V. M. Schneider, and S. Al-Bader, The Design of Mode Evolution Couplers, J. Lightwave Technol. **16**(10), 1907–1914 (1998).

[61] P. O'Sullivan and C. Hussey, Truly wavelength-flattened monolithic couplers, Electron. Lett. **33**(4), 321–322 (1997).

[62] V. J. Kuck, E. Laskowski, J. Shmulovich, A. Hale, E. A. Chandross, C. Madsen, and R. E. Scotti, Tunable directional optical waveguide couplers, Technical Report United States Patent 6 002 823, Dec. 14, 1999.

[63] D. Johlen, P. Klose, and E. Brinkmeier, UV-written directional couplers in silica-on-silicon, Proc. OFC 1997 (paper THI5), 279–280 (1997).

[64] H. Renner, Up and Down UV-Trimming of Planar Directional WAveguide Couplers: Modeling, IEE Photon Technol. Lett. **12**(7), 825–827 (2000).

[65] S. Hewlett, F. Ladouceur, and J. Love, Second-mode cutoff in rectangular-core couplers using the Fourier decomposition method, Optical and Quantum Electronics **27**(10), 987–94 (1995).

[66] S. Hewlett, J. Love, and V. Steblina, Analysis and design of highly broad-band, planar evanescent couplers, Optical and Quantum Electronics **28**(1), 71–81 (1996).

[67] A. Ankiewicz, A. Snyder, and X.-H. Zheng, Coupling Between Parallel Optical Fiber Cores-Critical Examination, J. Lightwave Technol. **LT-4**(9), 1317–23 (1986).

[68] R. Hereth and G. Schiffner, Broad-Band Optical Directional Couplers and Polarization Splitters, J. Lightwave Technol. **7**(6), 925–930 (1989).

[69] J. D. Love and V. V. Steblina, Highly broadband buried channel couplers, Electron. Lett. **30**(22), 1853–1854 (1994).

[70] C. H. Henry, E. J. Laskowski, Y. P. Li, and H. H. Yaffe, Optimized Waveguide Structure, Technical Report United States Patent 5 719 976, Feb. 17, 1998.

[71] A. Takagi, K. Jinguji, and M. Kawachi, Wavelength Characteristics of (2*2) Optical Channel-Type Directional Couplers with Symmetric Or Nonsymmetric Coupling Structures, J. Lightwave Technol. **10**(6), 735–46 (1992).

[72] A. Takagi, K. Jinguji, and M. Kawachi, Broadband silica-based optical waveguide coupler with asymmetric structure, Electron. Lett. **26**(2) (1990).

[73] F. Gonthier, D. Ricard, S. Lacroix, and J. Bures, Wavelength-flattened 2x2 splitters made of identical singe-mode fibers, Opt. Lett. **16**(15), 1201–1203 (1991).

[74] B. Little and T. Murphy, Design Rules for Maximally Flat Wavelength-Insensitive Optical Power Dividers Using Mach-Zehnder Structures, Photon. Technol. Lett. **9**(12), 1607–9 (1997).

[75] T. Murphy, B. Little, and H. Smith, Wavelength- and Polarization-Insensitive Integrated Directional Couplers Using Mach-Zehnder Structures, IPR proceedings 1999 , 138–140 (1999).

[76] L. Soldano, F. Veerman, M. Smit, B. Verbeek, A. Dubost, and E. Pennings, Planar Monomode Optical Couplers Based on Multimode Interference Effects, J. Lightwave Technol. **10**(12), 1843–50 (1992).

[77] L. C. Soldano, *Multimode Interference Couplers: Design and Applications*, PhD thesis, Technical University of Delft, The Netherlands, 1994.

[78] R. M. Jenkins, J. M. Heaton, D. Wight, J. Parker, G. Smith, and K. Hilton, Novel 1xN and NxN integrated optical switches using self-imaging multimode GaAS/AlGaAS waveguides, Appl. Phys. Lett. **64**(6), 684–686 (1994).

[79] J. Leuthold, R. Hess, J. Eckner, P. Besse, and H. Melchior, Spatial mode filters realized with multimode interference couplers, Opt. Lett. **21**(11), 836–8 (1996).

[80] D. S. Levy, Y. Li, R. Scarmozzino, and R. M. J. Osgood, Multimode Interference-Based Variable Power Splitter in GaAs-AlGaAs, Photon. Technol. Lett. **9**(10), 1373–1375 (1997).

[81] N. Lagali, M. Paiam, and R. MacDonald, Theory of Variable-Ratio Power Splitters Using Multimode Interference Couplers, Photon. Technol. Lett. **11**(6), 665–7 (1999).

[82] J. Heaton and R. Jenkins, General Matrix Theory of Self-Imaging in Multimode Interference (MMI) Couplers, Photon. Technol. Lett. **11**(2), 212–14 (1999).

[83] Y. Ma, S. Park, and T. H. Seng, Ultracompact Multimode Interference 3-dB Coupler with Strong Lateral Confinement by Deep Dry Etching, Photon. Technol. Lett. **12**(5), 492–494 (2000).

[84] M. P. Earnshaw, J. B. D. Soole, M. Cappuzzo, L. Gomez, E. Laskowski, and A. Paunescu, Compact, low loss 4x4 optical switch matrix using multimode intereferometers, Electron. Lett. **37**(2), 115–116 (2001).

[85] Q. Lai, M. Bachmann, and H. Melchior, Low-loss 1xN multimode interference couplers with homogeneous output power distributions realised in silica on Si material, Electron. Lett. **33**(20), 1699–700 (1997).

[86] T. Saida, A. Himeno, M. Okuno, A. Sugita, and K. Okamoto, Silica-based 2x2 multimode interference coupler with arbitrary power splitting ratio, Elctron. Lett. **35**(23), 2031–3 (1999).

[87] Q. Lai, M. Bachmann, W. Hunziker, P. Besse, and H. Melchior, Arbitrary ratio power splitters using angled silica on silicon multi-mode interference

couplers, European Conference on Optical Communication, ECOC **2**, 127–130 (1996).

[88] M. P. Earnshaw, J. B. D. Soole, M. Cappuzzo, L. Gomez, E. Laskowski, and A. Paunescu, 8x8 optical switch matrix in silica-on-silicon, Integrated Photonics Research (IMB2) (2001).

[89] L. B. Soldano and E. C. Pennings, Optical Multi-Mode Interference Devices Based on Self-Imaging: Principles and Applications, J. Lightwave Technol. **13**(4), 615–627 (1995).

[90] D. S. Levy, R. Scarmozzino, Y. M. Li, and R. M. J. Osgood, New Design for Ultracompact Multimode Interference-Based 2 by 2 Couplers, Photon. Technol. Lett. **10**(1), 96–98 (1998).

[91] D. Levy, R. Scarmozzino, and J. Osgood, R.M., Length Reduction of Tapered N*N MMI Devices, Photon. Technol. Lett. **10**(6), 830–2 (1998).

[92] J. Huang, R. Scarmozzino, and J. Osgood, R.M., A New Design Approach To Large Input/Output Number Multimode Interference Couplers and Its Application to Low-Crosstalk WDM Routers, Photon. Technol. Lett. **10**(9), 1292–4 (1998).

[93] M. Bachmann, P. Besse, and H. Melchior, General self-imaging properties in N by N multimode interference couplers including phase relations, Appl. Opt. **33**(18), 3905–3911 (1994).

[94] M. Rajarajan, B. Rahman, and K. Grattan, A Rigorous Comparison Of the Performance of Directional Couplers with Multimode Interference Devices, J. Lightwave Technol. **17**(2), 243–8 (1999).

[95] P. A. Besse, M. Bachmann, H. Melchior, L. Soldano, and M. Smit, Optical Bandwidth and Fabrication Tolerances of Multimode Interference Couplers, J. Lightwave Technol. **12**(6), 1004–1009 (1994).

[96] R. K. Sandberg and L. Leick, Novel design for integrated wavelength flat 980/1550 nm multiplexer, Integrated Photonics Research **IThI3** (2002).

[97] D. Barbier, Erbium-doped waveguide amplifiers promote optical-networking evolution, Lightwave (November) (2000).

[98] J. F. Massicott, R. Wyatt, and B. J. Ainslie, Low noise operation of Er3+ doped silica fiber amplifier around 1.6ţm, Elctron. Lett. **28**(20), 1924–1925 (1992).

[99] Y. Sun, J. W. Sulhoff, A. K. Srivastave, J. L. Zyskind, T. A. Strasser, J. R. Pedrazzani, C. Wolf, J. Zhou, J. B. Judkins, R. P. Espindola, and A. M. Vengsarkar, 80nm ultra-wideband erbium-doped silica fibre amplifier, Elctron. Lett. **33**(23), 1965–1967 (1997).

[100] A. G. Mustafa and B. McNeil, Building optical metro-access networks, Lightwave (March) (2001).

[101] S. A. Guldberg-Kjær, *Optically amplifying planar glass waveguides: Laser on a chip*, PhD thesis, COM, Technical University of Denmark, 2000.

[102] D. Barbier, M. Rattay, F. Saint Andre, G. Clauss, M. Trouillon, A. Kevorkian, J. M. P. Delavaux, and E. Murphy, Amplifying Four-Wavelengths Combiner, Based on Erbium/Ytterbium-Doped Waveguides Amplifiers and Integrated Splitters, IEEE Photon. Technol. Lett. **9**(3), 315–317 (1997).

[103] D. Barbier, P. Bruno, C. Cassagnettes, M. Troullon, R. L. Hyde, A. Kevorkian, and J. M. P. Delavaux, Net gain of 27 dB with a 8.6-cm-long Er/Yb-doped glass-planar-amplifier, Techn. Dig. OFC 1998 **Paper TuH5**, 45 (1998).

[104] J. Shmulovich, A. J. Bruce, G. Lenz, T. N. Nielsen, D. J. Muelhner, G. A. Bogert, I. Brener, E. J. Laskowski, A. Paunescu, I. Ryazansky, D. C. Jacobson, and A. E. White, Integrated Planar Waveguide Amplifier with 15dB net gain at 1550 nm, Techn. Digest. OFC 1999 **Paper PD442-1** (Febr. 1999).

[105] C. Laurent-Lund, M. R. Poulsen, M. Beukema, and J. E. Pedersen, Propagation and Waveguiding - PECVD Grown Multiple Core Planar Waveguides with Extremely Low Interface Reflections and Losses, IEEE Photon. Technol. Lett. **10**(10), 1431–1433 (1998).

[106] T. Negami, H. Haga, and S. Yamamoto, Guided-wave optical wavelength demultiplexer using an asymmetric y-juntion, Appl. Phys. Lett. .

[107] G. Zhang, S. Honkanen, S. I. Najafi, and A. Tervonen, Integrated 1.3 um/1.55 um wavelength multiplexer and 1/8 splitter by ion exchange in glass, Elctron. Lett. **29**(12), 1064–1066 (1993).

[108] A. Tervonen, P. Pöyhönen, S. Honkanen, M. Tahkokorpi, S. I. Najafi, and A. Tervonen, A Guided-Wave Mach-Zehnder Interferometer Structure for Wavelength Multiplexing, IEEE Photon. Technol. Lett. **3**(6), 516–518 (1991).

[109] R. K. Sandberg, Integrated Pump-Signal Wavelength Division Multiplexers, Technical report, COM, Technical University of Denmark, 2001.

[110] K. Hattori, T. Kitagawa, M. Oguma, Y. Ohmori, and M. Horiguchi, Erbium-doped silica-based waveguide amplifier integrated with a 980/1530 nm WDM coupler, Electron. Lett. **30**(11), 856–857 (1994).

[111] M. Paiam, C. Janz, R. MacDonald, and J. Broughton, Compact Planar 980/1550-Nm Wavelength Multi/Demultiplexer Based on Multimode Interference, IEEE Photon. Technol. Lett. **7**(10), 1180–2 (1995).

[112] M. Paiam and R. MacDonald, Polarisation-insensitive 980/1550 nm wavelength (de)multiplexer using MMI couplers, Elctron. Lett. **33**(14), 1219–20 (1997).

[113] A. Bakhtazad, J. N. McMullin, C. J. Haugen, and R. G. DeCorby, MMI Multiplexer for Dual-channel Erbium Doped Waveguide Amplifier, Optics Express **9**(4), 178–183 (2001).

[114] J.-L. Archambault and P. Russell, The grating-frustrated coupler, IEE Colloquium 'Planar Silicon Hybrid Optoelectronics' (Digest No.1994/198) , 9/1 (1994).

[115] J.-L. Archambault, P. Russell, S. Barcelos, P. Hua, and L. Reekie, Grating-frustrated coupler: a novel channel-dropping filter in single-mode optical fiber, Opt. Lett. **19**(3), 180–2 (1994).

[116] A.-C. Jacob-Poulin, R. Vallée, S. LaRochelle, D. Faucher, and G. R. Atkins, Channel-Dropping Filter Based on a Grating-Frustrated Two-Core Fiber, J. Lightwave Technol. **18**(5), 715–720 (2001).

[117] L. Leick and C. K. Madsen, Dispersion compensation of a 1 x N router with low loss, flat passband and low crosstalk, Optics Lett. **To appear**.

[118] L. Leick and C. Peucheret, Dispersion induced penalty for 1xN passive interferometric optical MUX/DEMUXs and its reduction using all-pass filters, European Conference on Optical Communication **Paper 01.2.4** (2002).

[119] G. Lenz, C. R. Eggleton, B. J. andGiles, C. K. Madsen, and R. E. Slusher, Dispersive Properties of Optical Filters for WDM Systems, IEEE J. Quantum Electron. **34**(8), 1390–1402 (1998).

[120] M. Amersfoot, C. de Boer, F. van Ham, M. Smith, P. Demeester, J. van der Tol, and A. Kuntze, Phase-array wavelength demultiplexer with flattened wavelength response, Electron. Lett. **30**(4), 300–302 (1994).

[121] K. Okamoto and H. Yamada, Arrayed-waveguide grating multiplexerwith flat spectral response, Opt. Lett. **20**(1), 1312–1314 (1995).

[122] C. Dragone, T. Strasser, G. Bogert, L. Schulz, and P. Chou, Waveguide grating router with maximally flat passband produced by spatial filtering, Electron. Lett. **33**, 1312 (1997).

[123] C. H. Henry, R. F. Kazarinov, Y. Shani, R. C. Kistler, V. Pol, and K. J. Orlowsky, Four-Channel Wavelength Division Multiplexers and Bandpass Filters based on Elliptical Bragg Reflectors, J. Lightwave Technol. **8**, 748 (1990).

[124] K. Miyazaki, A. Okamoto, and H. Nakjima, Optical Multiplexer/Demultiplexer Using Thin-film Optical Filters, Fujitsu Scientific and Technical Journal (1980).

[125] B. Verbeek, C. Henry, N. Olsson, K. Orlowsky, R. Kazarinov, and B. Johnson, Intergrated four-channel Mach-Zehnder multi/ demultiplexer fabricated with phosphorous doped SiO2 waveguides on Si, J. Lightwave Technol. **6**, 1011 (1995).

[126] C. Van Dam, M. Amersfoot, G. ten Kate, F. van Ham, M. Smith, P. Besse, M. Bachmann, and H. Melcior, Novel InP-based phased-array wavelength demultiplexer using a generalized MMI-MZI configuration, Proc. 7th Eur. Conf. Integrated Optics (ECIO), Delft, The Netherlands , 275 (1995).

[127] C. K. Madsen and G. Lenz, Optical All-Pass Filters for Phase Response Design with Applications for Dispersion Compensation, IEEE Photon. Tecnol. Lett. **10**(7), 994–996 (1998).

[128] G. Lenz and C. K. Madsen, General Optical All-Pass Filter Structures for Dispersion Control in WDM Systems, J. Lightwave Technol. **17**(7), 1248–1254 (1999).

[129] C. K. Madsen, A Multiport Frequency Band Selector with Inherently Low Loss, Flat Passbands and Low Crosstalk, IEEE Photon. Tecnol. Lett. **10**(12), 1766–1768 (1998).

[130] C. K. Madsen, Efficient architectures for Exactly Realizing Optical Filters with Optimum Bandpass Designs, IEEE Photon. Tecnol. Lett. **10**(8), 1136–1138 (1998).

[131] K. Enser, R. I. Laming, M. Zervas, M. N.and Ibsen, and M. Durkin, Effects of non-ideal group delay and reflection characteristics of chirped fibre grating dispersion compensators, ECOC 1997 **2**, 45–48 (1997).

[132] C. J. Anderson and J. A. Lyle, Technique for evaluating system performance using Q in numerical simulations exhibiting intersymbo interference, Electron. Lett. **30**(1), 71–72 (1994).

[133] C. K. Madsen, G. Lenz, A. J. Bruce, M. A. Capuzzo, L. T. Gomez, and R. Scotti, Integrated All-Pass Filters for Tunable Dispersion and Dispersion Slope Compensation, IEEE Photon. Technol. Lett. **11**(12), 1623–1625 (1999).

[134] K. Takada, H. Yamada, and Y. Inoue, Optical Low Coherence Method for Characterizing Silica-Based Array-Waveguide Grating Multiplexers, J. Lightwave Technol. **31**, 360 (1995).

[135] L. Leick, A. Harpøth, and M. Svalgaard, Empirical model for the waveguiding properties of directly UV written waveguides, Appl. Optics **To appear** (2001).

[136] M. Svalgaard, A. Harpøth, and L. Leick, Empirical model for the waveguiding properties of directly UV written waveguides, 2001 OSA Topical meeting on Bragg Gratings, Photosensitivity and Poling **Tech. Digest Series**, BThC32 (2001).

[137] G. D. Maxwell and B. J. Ainslie, Demonstration of a directly written directional coupler using UV induced photosensitivity in a planar silica waveguide, Electron. Lett. **31**, 95–96 (1995).

[138] J. Hübner, C. Poulsen, J. Pedersen, M. Poulsen, T. Feuchter, and M. Kristensen, UV-written Y-splitter in Ge-doped silica, Lasers and Integrated Optoelectronics, SPIE **2695**, 98–104 (1996).

[139] M. Svalgaard, Direct writing of planar waveguide power splitter and directional couplers using a focused ultraviolet laser beam, Electron. Lett. **33**, 1694–1695 (1997).